AN EXPERIMENTAL STUDY OF
THE TIME-DEPENDENT BEHAVIOR
OF THE APPENDAGE-BODY JUNCTION VORTEX

by

Joseph M. Fallone

B.S.M.E., United States Naval Academy
(1979)

SUBMITTED TO THE DEPARTMENT OF OCEAN ENGINEERING
IN PARTIAL FULFILLMENT OF THE REQUIREMENTS
FOR THE DEGREES OF

NAVAL ENGINEER

and

MASTER OF SCIENCE IN NAVAL ARCHITECTURE AND MARINE
ENGINEERING

at the

MASSACHUSETTS INSTITUTE OF TECHNOLOGY
June 1989

© Massachusetts Institute of Technology, 1989

The author hereby grants to the United States Government and its' agencies permission to reproduce and tc distribute copies of this thesis document in whole or in part.

Signature of Author _____
Department of Ocean Engineering
May, 1989
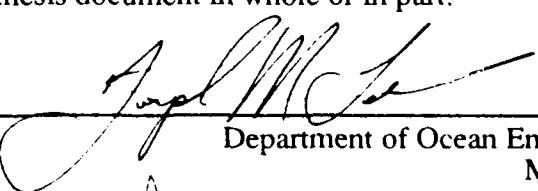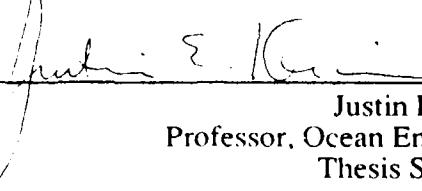
Certified by _____
Justin E. Kerwin
Professor, Ocean Engineering
Thesis Supervisor
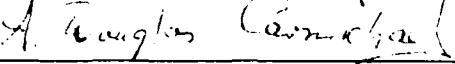
Accepted by _____
A. Douglas Carmichael
Chairman, Departmental Graduate Committee
Department of Ocean Engineering

89   10   10   135

AN EXPERIMENTAL STUDY OF
THE TIME-DEPENDENT BEHAVIOR
OF THE APPENDAGE-BODY JUNCTION VORTEX

by

Joseph M. Fallone

ABSTRACT

The three-dimensional flow in the region where a turbulent boundary layer encounters an appendage is characterized by the formation of a junction root vortex. The formation of this vortex can be attributed to the adverse pressure gradient upstream of the appendage. One major area of concern is the temporal behavior of the vortex. Fluctuations in the size and/or location of the vortex can cause degradation of downstream components or excitation of local structures. Recent studies in wind tunnels have identified a bi-modal characteristic in the structure of the vortex.

An experimental investigation of the time-dependent behavior of the junction root vortex was conducted using MIT's variable pressure water tunnel and laser doppler anemometry system. Data was collected at various points forward of a modified NACA 0020 section appendage mounted on a splitter plate and analyzed using off-line DFT analysis. The data was gathered at tunnel speeds of 10 and 20 ft/sec using an analog-to-digital acquisition system. Velocity probability distributions using a fully digital acquisition system were also plotted to identify the bi-modal structure.

The spectra generated from the DFT analysis were inconclusive. No distinct frequencies or pattern of frequencies attributable to the flow could be identified. Fluctuations within the spectra made their accuracy questionable. The existence of the bi-modal structure was confirmed by the velocity probability distributions.

Thesis Supervisor: *Dr. Justin E. Kerwin*

Title: Professor of Ocean Engineering

ACKNOWLEDGEMENTS

I owe a great deal of thanks to a number of people for helping me complete this thesis and the rest of my graduate study. First and foremost, I owe my undying gratitude to my loving wife Nancy for her patience during the many lonely hours, and her understanding at my inattentiveness. Without her constant love and support, I never would have made it through the many times when it felt like the world was falling in around me.

I also owe a great deal to my wonderful son Jonathan and my beautiful daughter Nicole. For the past three years, there have been many times when I was not much of a daddy. I can only hope that in the future they will understand and that I can make it up to them.

Table of Contents

Table of Figures

Table of Tables

1 INTRODUCTION

1.1 BACKGROUND

The two-dimensional turbulent boundary layer along a body has been studied extensively and is well understood. When this boundary layer encounters an appendage, however, the flow in the region of the junction becomes extremely complex. This three-dimensional flow is characterized primarily by the formation of a "horseshoe" or junction root vortex at the base of the appendage. There are many practical examples of this flow including the keel of a sailboat, a submarine's sail and control surfaces, an airplane's wings and stabilizers, and even a telephone pole in a windstorm.

The formation of this vortex secondary flow can be attributed to the adverse pressure gradient upstream of the appendage. The vorticity in the incoming turbulent boundary layer[1] is concentrated or coalesced by the gradient forming the vortex. The flow causes the vortex to wrap around the appendage turning the cross-flow vorticity of the incoming boundary layer into streamwise vorticity. The vortex produces a three-dimensional separation region in the vicinity of the appendage.

Dickinson [5] divided the flow around an appendage into three conceptual regions. The *inflow region* is the region upstream of the appendage where the presence of the appendage is not felt. The second region is the *appendage region*. This is the region which includes the adverse pressure gradients and the generation of the secondary flows associated with the appendage. This region is further divided into the *leading edge subregion*, the *alongside subregion*, and the *trailing edge subregion*. The final region is the *wake*.

---

1 A junction vortex can also form when the incoming boundary is laminar.

A number of experimental studies have been conducted or are currently in progress to characterize the junction vortex. Most of the early work concentrated on investigating the flow for various appendage geometries. Love [9] conducted some preliminary research which showed that the curvature of the leading edge affected the strength of the generated vortex. Since then, Belik [2] and Baker [1] have investigated the flow using cylindrical appendages; while Shabaka and Bradshaw [21], Oguz [13], Kubendran [8], and McMahon et al. [10],[11] conducted studies using infinite-chord appendages. To study the flow around more realistic hydrodynamic shapes, Dickinson [4],[5] of the David Taylor Research Center (DTRC) and Pierce et al. [14],[15],[16] of Virginia Polytechnic Institute (VPI) have used streamlined foils in their experimental work. A more complete literature review on the topic of the junction vortex can be found in Sung [22]. This document not only references experimental studies, but also publications on analytic and numerical work.

The majority of experimental work on the junction vortex flow has been for the purpose of obtaining data to support the development of analytic or numerical prediction schemes. The data has been collected using various experimental techniques including flow visualization, hot-wire/film anemometry, laser doppler anemometry, and pressure taps with most of the investigations having been conducted in low-turbulence wind tunnels. Recently, a great deal of attention has been focused on reducing the strength of the generated root vortex. In marine applications, the presence of this vortex can degrade the performance of downstream control surfaces and propellers. The use of fillets and other leading edge modifications is currently under study by various institutions. Pierce, Frangistas, and Nelson [17] have published some preliminary results from the studies being conducted at VPI.

Another area of concern is the temporal behavior of the junction vortex. Fluctuations in the size and/or location of the vortex can cause additional degradation of downstream components, or excitation of local structures resulting in vibrational and acoustical problems. Rood et al. [18],[19] conducted some of the first studies on the time-dependent nature of the junction vortex flow. He reported relatively low frequency and narrow bandwidth turbulent fluctuations in the three-dimensional boundary layer downstream of a streamlined protuberance with a 1.5:1 elliptical nose, similar to the one used in this study. In a meeting on appendage design at DTRC in 1988, Dr. R.L. Simpson [3] of VPI reported detecting a bi-modal characteristic in the structure of the vortex. Histograms of streamwise velocity fluctuations measured close to the line of shear[2] exhibit two distinct peaks. Pierce et al. [17] have shown that the spectra within the vortex flow is similar to that in the upstream boundary layer, suggesting that the fluctuations in the large scale vortex structure originate in the boundary layer.

1.2 RESEARCH GOALS

This experimental investigation had two purposes. The primary goal was to gather raw data on the junction vortex flow and process it to obtain information on the time dependent nature of the flow through spectral analysis. Unlike previous studies which were conducted using wind tunnels, this investigation was conducted in a circulating water tunnel. An attempt to verify the bi-modal structure identified by Simpson and quantify its frequency of fluctuation was a principal element of this objective.

---

2 The line of shear delineates a region of high shear near the foil from an area of lower shear outside. The line of shear falls inside the separation line forward of the appendage.

The other purpose of the investigation was to determine the feasibility of using velocity data from the laser doppler system in MIT's variable pressure water tunnel facility to conduct spectral analysis. A key element of this goal was to incorporate a new all-digital acquisition and flow analysis system into the laboratory facility.

2 EXPERIMENTAL APPARATUS

2.1 VARIABLE PRESSURE WATER TUNNEL

All testing and data acquisition was conducted using MIT's variable pressure water tunnel [7]. This facility is designed to test and evaluate the dynamic performance of propellers and two and three dimensional hydrofoils. The test section is a 54 inch long, 20 inch square closed-jet section. The maximum test section speed is 33 ft/sec.

The area directly upstream of the test section contains the upstream turning vanes, a circular to square transition section, a settling section, and a contraction. The transition section has a contraction ratio of 1.46:1, while the ratio for the contraction section is 4.92:1. The overall contraction ratio for the facility is 7.17:1. The settling section contains a honeycomb consisting of one inch diameter acrylic tubes, each one being one foot long, and three wire screens. The settling section is designed to reduce the turbulence in the test section. Measurements of the free stream turbulence using the laser doppler velocimeter show a turbulence intensity of less than 0.5 percent, accounting for phase noise[3] in the velocity measurements.

The test section is immediately followed by a diffuser, downstream turning vanes, and a square to circular transition section. The closed circuit flow in the water tunnel is driven by a 30.25 inch diameter four-bladed impeller.

2.2 BODY/APPENDAGE JUNCTION MODEL

The model used in the study of the junction vortex consisted of a modified NACA 0020 foil section mounted on a flat splitter plate. The foil and plate were both

---

3 Phase noise is related to the bandwidth of the doppler signal spectrum and can be related to an equivalent turbulence intensity.

constructed using anodized aluminum. The foil section was produced on a numerically controlled milling machine.

Figures 1 and 2[4] show the model layout, test section mounting arrangement, and experimental coordinate system.
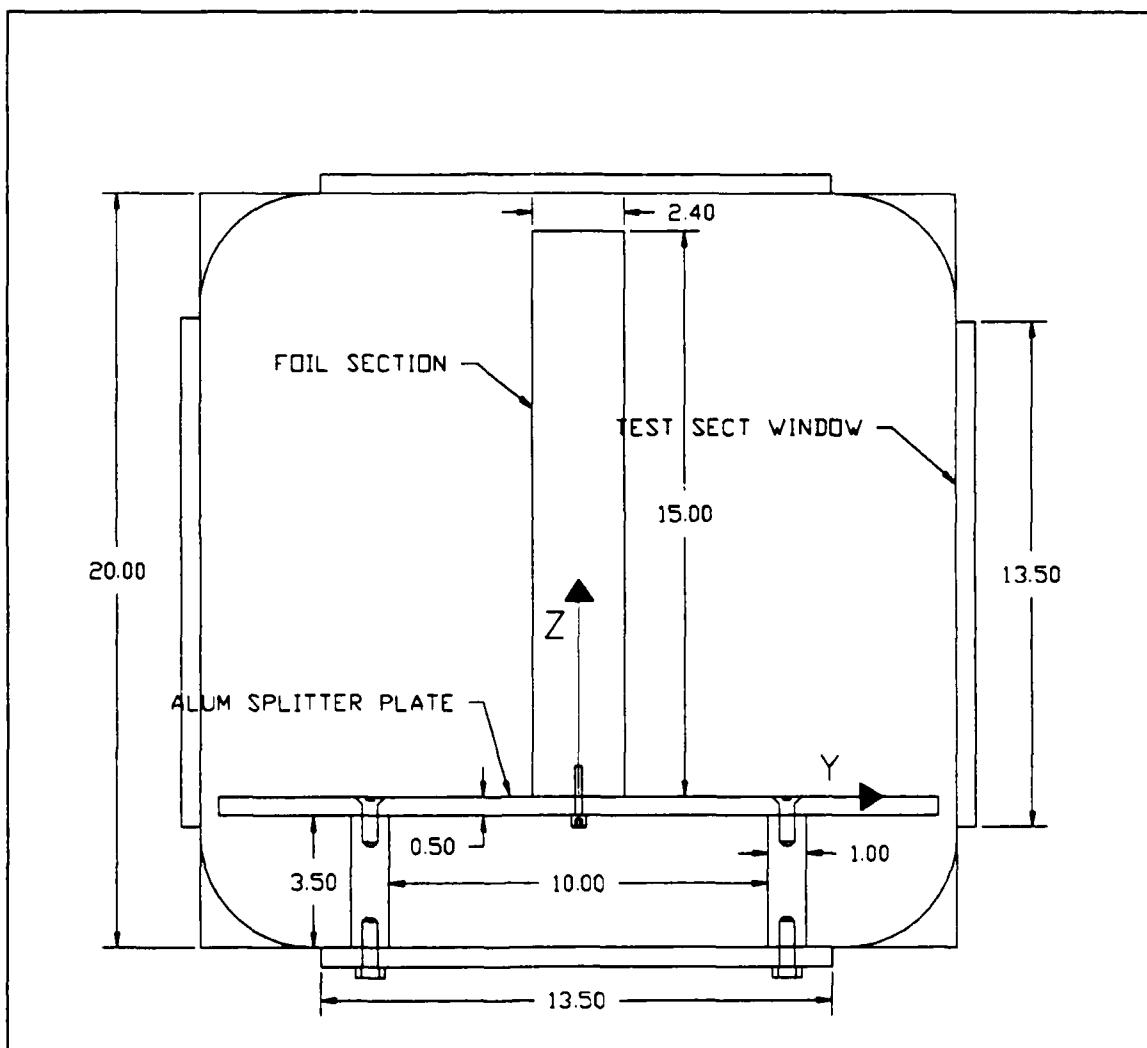
Figure 1.
Test Section Layout
(Front View)

---

4 All dimensions in Figures 1 and 2 are in inches.
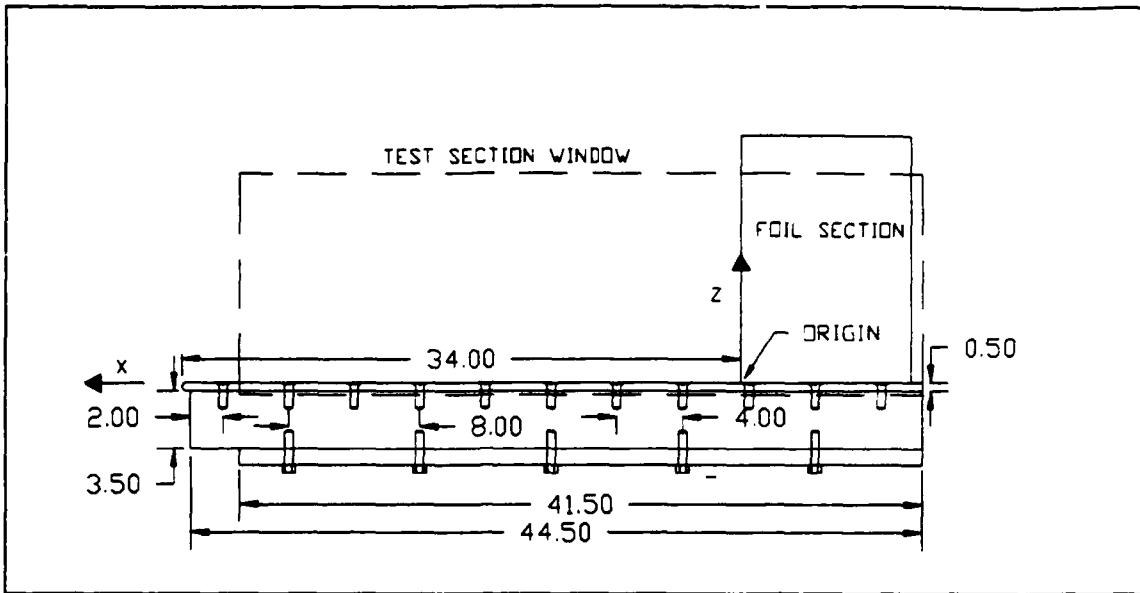
Figure 2.
Test Section Layout
(Side View)

The shape of the foil section was chosen to conform to several previous investigations (see Section 1.1). The standard NACA 0020 section was modified by replacing the nose with a 1.5:1 elliptical arc. This bluff leading edge produces a stronger adverse pressure gradient which promotes the formation of the junction vortex. Equations 2.1 and 2.2 were used to generate the foil section offsets.

Nose Section:

$$\frac{y^2}{1.2^2} + \frac{(x-1.8)^2}{1.8^2} = 1 \tag{2.1}$$

Tail Section:

$$y/c = 0.2969 \cdot \sqrt{x/c} - 0.126 \cdot x/c - 0.3516 \cdot (x/c)^2 \tag{2.2}$$
$$+0.2843 \cdot (x/c)^3 - 0.1015 \cdot (x/c)^4$$

Page 14

The two shapes were joined at their respective maximum widths (2.4 inches) resulting in a chord length of 10.3 inches. The span of the foil was set at 15 inches to allowing a 2.4 inch gap between the foil and top of the test section.
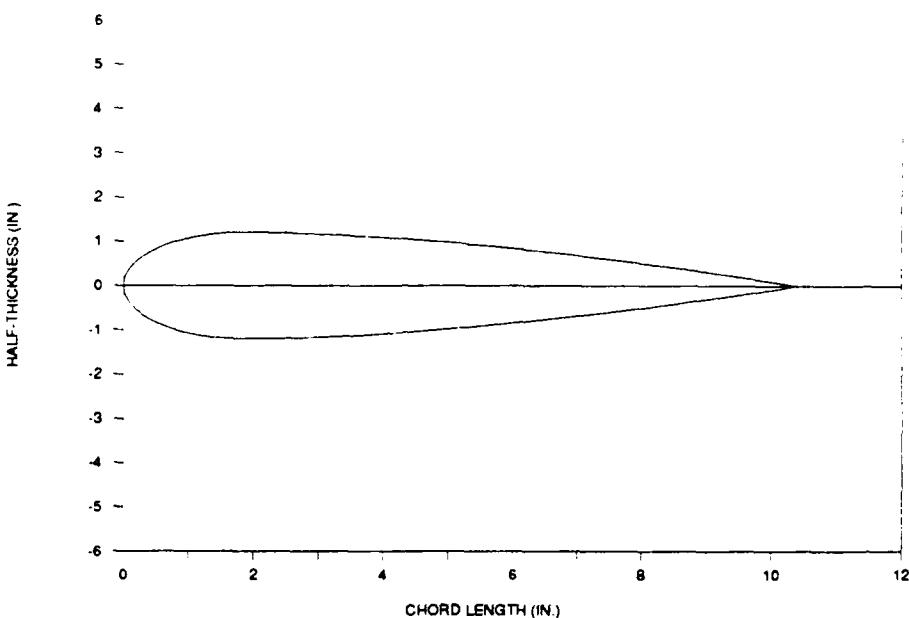
Figure 3.
Modified NACA 0020 Foil Section

Trip wires of circular cross-section were positioned just aft of the leading edge of the splitter plate and 0.4 inches upstream of the maximum thickness of the foil. The trip wire on the splitter plate invoked the development of a turbulent boundary layer along the plate forward of the foil. As recommended by Devenport and Simpson [3], the boundary layer on the foil was tripped to avoid any unsteadiness of the flow which might have resulted from natural transition. A trip wire diameter of 0.047 (3/64) inches was used in both cases making them fully effective down to a tunnel speed of 2.26 ft/sec as stated by Schlichting [20].

2.3 LASER DOPPLER VELOCIMETER SYSTEM

The velocity data used for this study was gathered using the horizontal component of a three-component laser doppler velocimeter. A three watt Argon-Ion laser serves as the coherent light source for the measurement system. The beam of light from the laser is split into three components, green (λ=5.14 nm), blue (λ=488.0 nm), and violet (λ=476.5 nm), by an optical color separator. The blue component is used for horizontal measurements.

Each component of the laser is further split into two beams in a dual beam system. By use of optical lenses and mirrors, the two beams intersect at a fixed angle inside the tunnel test section forming an ellipsoidal measurement volume. The two intersecting beams of light produce a fringe pattern within this measurement volume perpendicular to the plane formed by the two beams. A particle in the fluid moving through this fringe pattern will scatter light. The intensity of the scattered light will be modulated at a frequency determined by the fringe spacing and velocity of the particle perpendicular to the fringe pattern. This frequency is called the doppler frequency and is given by Equation 2.3.

$$f_D = \frac{2 \cdot u \cdot \sin k}{\lambda} \tag{2.3}$$

f_D = doppler frequency
u = component of velocity perpendicular to the fringe pattern
k = one-half of the intersection angle of the two beams
λ = wavelength of light

The scattered light from particles crossing the measurement volume is collected by a set of receiving optics and detected with a photomultiplier tube which converts the modulated light signal to a voltage signal with the same doppler frequency. The signal is

then processed by a data acquisition system to obtain the measured component of the particle velocity. The receiving optics can be placed at any location where the measuring volume can be effectively viewed. In this study, the same optics were used to focus the outgoing light and collect the scattered light; this is called an on-axis backscatter system.

A stationary fringe pattern cannot differentiate between equal positive and negative flow velocities, nor can it convey a zero flow condition. To overcome this shortcoming, a frequency shift is applied to one of the two crossing beams. This causes the fringe pattern to slowly move upstream or downstream depending on the magnitude and direction of the shift. The moving fringe pattern will produce a doppler frequency even in a zero flow condition and will provide different frequencies for equal positive and negative flow velocities.

The laser doppler velocimeter used in this study was mounted on a three-axes traverse table. The motion of the table was controlled remotely from a personal computer using feedback control. The positional accuracy of the traverse table, as stated in the operations manual, is 2.5 μm.

Additional information on laser doppler anemometry theory and techniques can be found in Durst, Melling, and Whitelaw [6].

Table I.
Laser System Characteristics

Wavelength	488.0 nm
Diameter of Measurement Volume	63 μm
Length of Measurement Volume	736 μm
Number of Fringes	22
Fringe Spacing	2.85 μm

3 DATA ACQUISITION

3.1 ANALOG-TO-DIGITAL ACQUISITION

The data for the spectra in Appendix B was collected using an analog-to-digital

acquisition system. Figure 4 depicts this acquisition system.
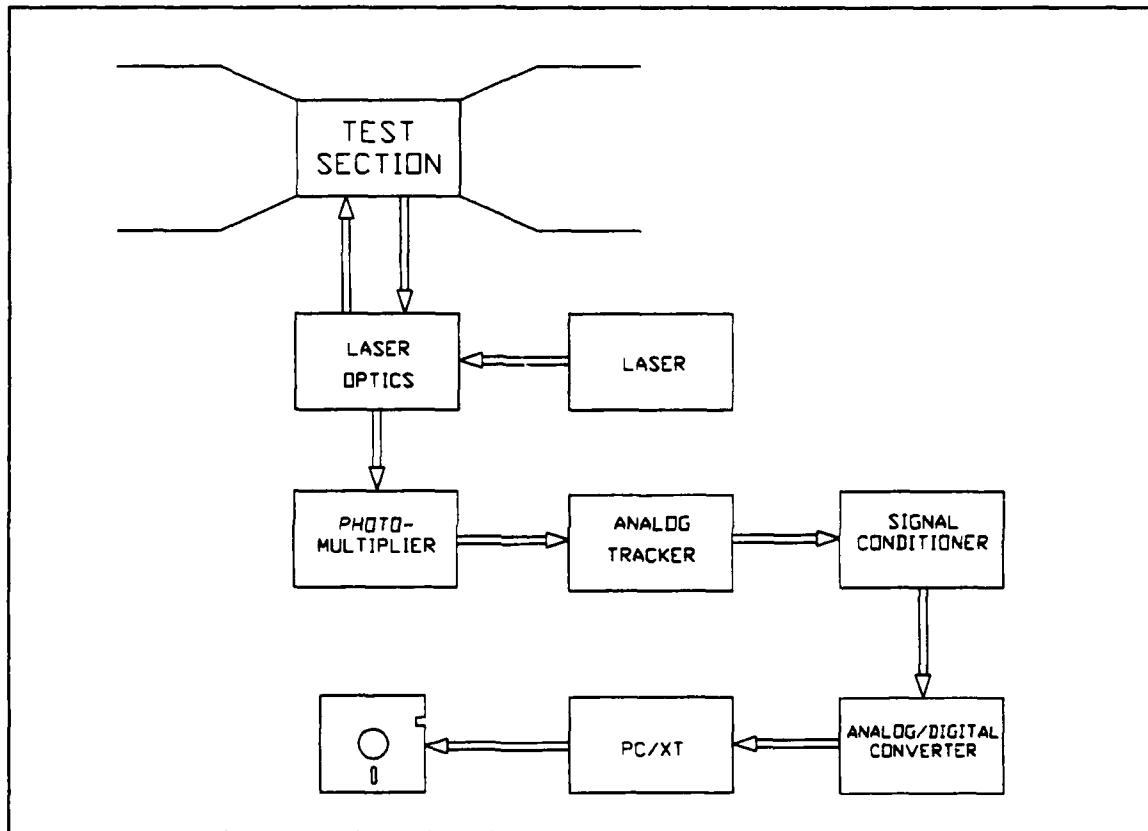
Figure 4.
Analog Data Acquisition System

As shown, the modulated voltage signal from the photomultiplier tube was fed to an

analog tracker. The tracker is a signal processor specifically designed to convert the

doppler frequency to an analog voltage, and extract the signal from the background noise.

Since the signal from the photomultiplier tube is discontinuous and varies in amplitude.

the tracker serves as a combination of tracking filter, frequency to voltage converter, and sample and hold circuit. The validity of the signal is confirmed before making it available for output as a voltage directly proportional to flow velocity.

The output voltage from the tracker was sent through a signal conditioner. The only purpose of this device was to apply a 1kHz low pass filter to the voltage signal, which was necessary to prevent aliasing during the off-line spectral analysis (see Section 4.1). The filtered voltage was then converted to digital information by using one channel of a 16-channel analog-to-digital converter board installed in the laboratory's personal computer.

The operation of the converter board was controlled via software directly from the computer keyboard, permitting selection of sampling frequency and number of data points. The digitized voltage versus time data was converted to an output file and placed on a floppy disk for later analysis. For each collection of samples, a graphic display of voltage versus time was available on the computer screen. Figure 5 is an example of a typical display. Note the large amount of scatter in the tracker output.
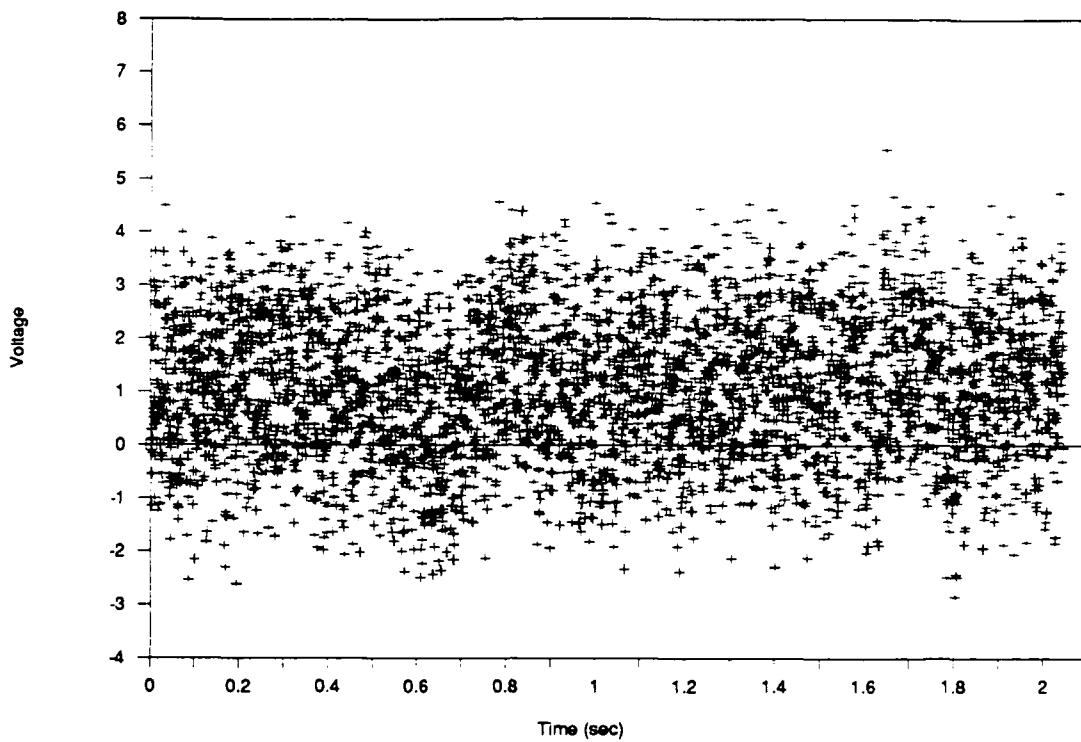
Figure 5.
Typical Digitized Data Display

The digital-to-analog converter and data analysis software used to generate the
spectra in Appendix B was designed for operation on continuous signals. The tracker's
output signal, however, appears as "points" or "lines" due to the data validation circuity.
This simply means that the last reading is held until a new reading is validated. The out-
put then is basically a series of point measurements rather than a continuous output. To
meet the continuity requirements for the analysis, it was necessary, therefore, to insure
that the data rate from the tracker sufficiently exceeded the data sampling frequency. In
all cases, the tracker data rate exceeded the 2000 Hz sampling frequency by a factor of
five.

3.2 FULL DIGITAL ACQUISITION

The data for the velocity probability distributions in Appendix C was collected using a fully digital acquisition system. Figure 6 depicts this acquisition system.
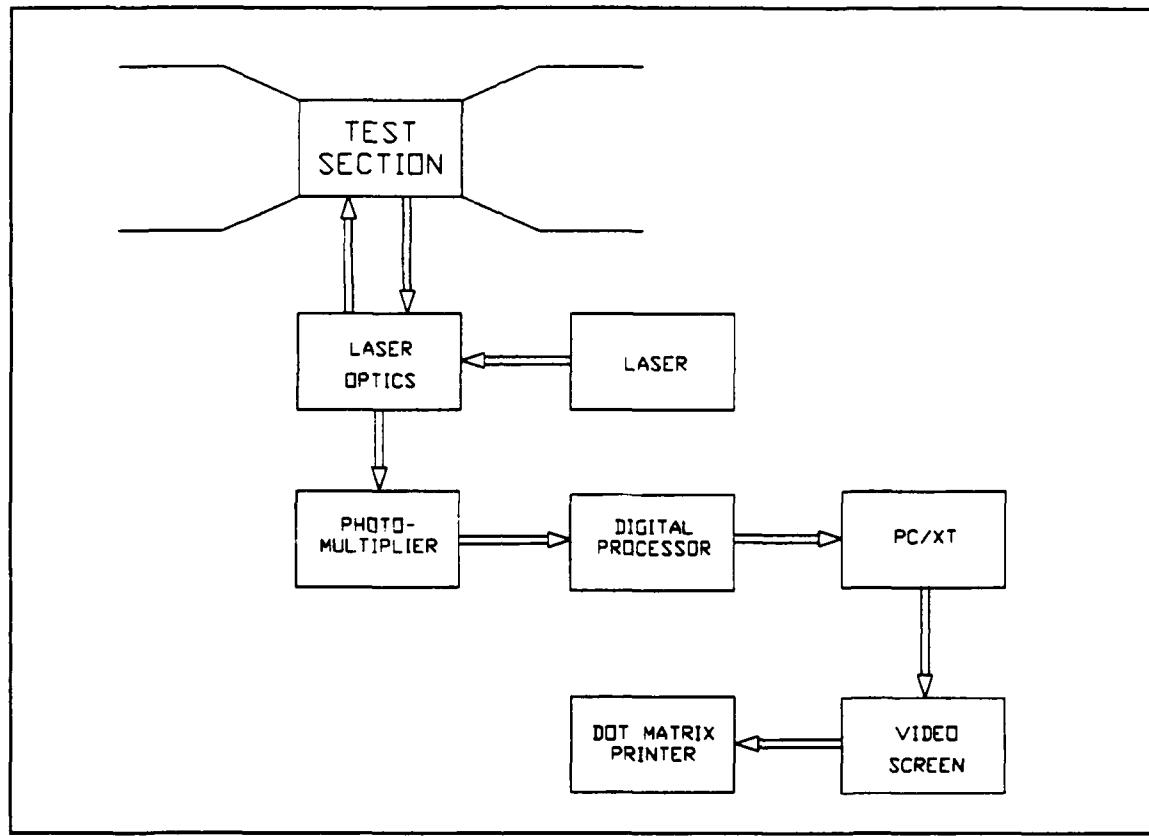

Figure 6.
Digital Data Acquisition System

The primary difference between the data acquisition system in Section 3.1 and that in Figure 6 is incorporation of a digital signal processor or Intelligent Flow Analyzer (IFA)[5]. One exceptional feature of the IFA is that it makes only "good" measurements or it makes no measurements at all. The IFA determines the doppler frequency by measuring the duration of eight contiguous cycles of the doppler signal. This elapsed time is

---

5 The Intelligent Flow Analyzer (IFA) is a product of Thermal Systems. Inc. (TSI).

then processed to obtain the frequency. To extract the true doppler signal from background noise, the IFA uses an autocorrelation of zero-crossings technique. The result is highly accurate data.

The IFA was not used to gather the data for the spectral analysis for two reasons: (1) It was not available during the initial measurements. (2) The processor data rate was insufficient to meet the 2000 Hz sampling requirement. In many cases, the maximum obtainable data rate was lower by a factor of ten than that required by the spectral analysis (see Section 4.1). Non-optimal tunnel seeding[6] and the processors stringent validation algorithm were the probable causes of this unfortunate limitation.

The IFA was directly controlled from the laboratory personal computer. The real-time display software installed on the computer not only controlled the IFA functions, but also produced the velocity probability distributions found in Appendix C.

---

6 Seeding is the process of adding particles to the flow to improve the fluids ability to scatter light.

4 DATA ANALYSIS

4.1 SPECTRAL ANALYSIS FUNDAMENTALS

The purpose of spectral analysis is to determine the frequency composition of a continuous random function of time $x(t)$. Since most experimental measurements of random functions are now conducted digitally, the spectral analysis is performed on a discrete series of numbers, $x_r(t)$, obtained by sampling the continuous function $x(t)$. The introduction of the fast Fourier transform (FFT) has made the calculation of spectral estimates directly from the discrete time series extremely quick and very accurate.

Any non-periodic function of time can be represented by a Fourier integral of the form

$$x(t) = \int_{-\infty}^{\infty} A(w)\cos(wt)dw + \int_{-\infty}^{\infty} B(w)\sin(wt)dw \tag{4.1}$$

w = angular frequency (rad/sec)

where

$$A(w) = \frac{1}{2\pi}\int_{-\infty}^{\infty} x(t)\cos(wt)dt$$

$$\tag{4.2}$$

$$B(w) = \frac{1}{2\pi}\int_{-\infty}^{\infty} x(t)\sin(wt)dt$$

For engineering purposes, Equation 4.1 is true in classical Fourier analysis if

$$\int_{-\infty}^{\infty} |x(t)|\, dt < \infty \tag{4.3}$$

Defining $X(w)$ as

$$X(w) = A(w) - iB(w) \tag{4.4}$$

Equations 4.2 can be combined to give

$$X(w) = \frac{1}{2\pi} \int_{-\infty}^{\infty} x(t)e^{-iwt} dt \qquad (4.5)$$

Equation 4.5 is the formal definition of $X(w)$ and is called the Fourier transform of $x(t)$.

The condition given by Equation 4.3 cannot be satisfied by an unending stationary[7] process. Therefore the classical Fourier theory cannot be applied to most experimental data. This difficulty is overcome by analyzing the autocorrelation function $R_x(\tau)$. The autocorrelation of a function $x(t)$ is defined as the average of the product $x(t)x(t+\tau)$, which for a stationary process is only a function of the time difference τ. The autocorrelation function can be adjusted to meet the condition of Equation 4.3 allowing it to be Fourier transformed. The transform of $R_x(\tau)$ is called the spectral density or the spectrum of $x(t)$.

Most experimental data, as stated above, is a discrete series of samples $x_r(t)$, $r = 0,1,2,...,(N-1)$, where $t = r\Delta$ and $\Delta = T/N$. T is defined as the total sampling time and N is the total number of samples. In this situation, the integral in Equation 4.5 can be replaced by the summation

$$X_k = \frac{1}{N} \sum_{r=0}^{N-1} x_r e^{-i2\pi kr/N} \quad k = 0, 1, 2, ..., (N-1) \qquad (4.6)$$

Equation 4.6 is the formal definition of the discrete Fourier transform (DFT), where k is the harmonic number that is related to a discrete angular frequency $w = 2\pi k/T$. The fast Fourier transform is a computer algorithm for calculating DFT's.

---

7 A process is said to be stationary if the probability distribution of a collection of samples is independent of absolute time.

The advantage of the DFT is that it can be used to generate the spectrum of $x(t)$ directly from the discrete time series $x_r(t)$ without first generating the autocorrelation function. The theory supporting this can be found in Newland [12]. The DFT produces spectral components at the frequencies defined by the harmonic numbers $k = 0,1,2,...,(N-1)$. Values of the spectrum for $k > (N-1)$ can be shown to simply repeat themselves. Additionally, it can be shown that the spectrum is symmetrical about the zero frequency position. The unique and valid portion of the spectrum exists only between $w = 0$ and $w = \pi/\Delta$. The upper limit on the frequency is called the Nyquist frequency[8] w_o and is the maximum frequency that can be detected from data sampled at a time spacing Δ. If frequencies greater than w_o exist in the original signal, distortion of the spectrum called aliasing can occur. The original signal must be filtered prior to processing to remove these frequencies to avoid this distortion.

The accuracy of a spectral measurement depends on the effective bandwidth of the measurement and the total sampling time T. The ratio of the standard deviation σ to the mean value m of the spectral density is given by Equation 4.7.

$$\frac{\sigma}{m} \cong \frac{1}{\sqrt{B_e T}} \qquad (4.7)$$

For most practical methods of calculating the spectrum using DFT's, the effective bandwidth B_e is approximately $1/T$ Hz. This means that $\sigma/m \cong 1$, or the magnitude of the standard deviation of the spectrum is equal to the mean. To improve this accuracy, several adjacent spectral estimates can be averaged increasing the effective bandwidth. Equation 4.7 becomes

---

8 The Nyquist frequency, when converted to Hz, is $f_o = 1/2\Delta$.

$$\frac{\sigma}{m} \cong \sqrt{\frac{1}{2n+1}} \qquad (4.8)$$

$(2n+1)$ = number of adjacent estimates

The larger the number of adjacent estimates that are averaged, the greater the accuracy, but not without a price. The increase in effective bandwidth also lowers the frequency resolution.

Another method of improving the accuracy of a spectral estimate is the application of a tapered data window. This function modifies the input data record by weighting the middle of the digital information more heavily than the two ends. The overall effect is a smoothing of the input data with a corresponding increase in the sharpness of the spectral window. The increase in sharpness comes at the expense of a slightly larger bandwidth and lower frequency resolution. Figure 7 shows one type of a tapered data window called a Hamming window.
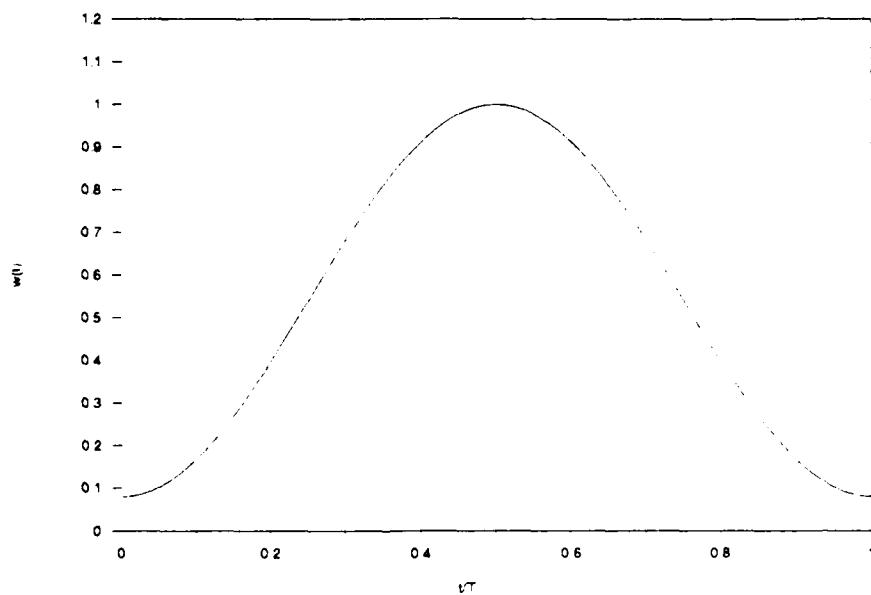
Figure 7.
Hamming Window

The following steps, as given by Newland [12], summarize the procedure for developing spectra from digital input data:

1. Estimate the frequency range of interest.

2. Choose an appropriate sampling interval Δ to insure that the Nyquist frequency exceeds the frequency of interest. Filter the input data to remove frequencies higher than the Nyquist frequency.

3. Decide on the required accuracy σ/m.

4. Estimate the required frequency resolution and specify the maximum effective bandwidth B_e.

5. Calculate the total sampling time T from Equation 4.7.

6. Determine the number of data points needed from $N = T/\Delta$. The total number of data points for each record must be equal to a power of two to apply FFT analysis.

7. Determine the number of adjacent spectral estimates that must be averaged from Equation 4.8.

8. Conduct the Fourier analysis using data taper windows if desired.

9. Average the required number of adjacent spectral estimates to obtain the smooth spectrum.

4.2 SPECTRUM DEVELOPMENT

The spectra in Appendix B were generated using the theory and procedure outlined in Section 4.1. Table II lists the particular parameters used in the Fourier analysis.

Table II.
Fourier Analysis Parameters

Frequency Range	0-500 Hz
Nyquist Frequency f_o	1000 Hz
Sampling Frequency	2000 Hz
Sampling Interval Δ	0.0005 sec
Number of Sample Points N	4096
Total Sample Time T	2.0475 sec
Number of Estimates Averaged	5
Effective Bandwidth B_e	2.442 Hz
Frequency Resolution	4.884 Hz
Accuracy σ/m	0.4472

The data for the spectra was gathered by surveying the area just forward of the foil, the incoming boundary layer, and the free stream. Measurements were made at tunnel speeds of 10 and 20 ft/sec. This equates to Reynolds numbers of 8.7×10^5 and 1.7×10^6 based on the chord length of the foil. If Reynolds numbers are calculated using the momentum thickness of the theoretical boundary layer, as in previous studies, the results are 5330 and 9280 respectively. Attempts were also made to collect data at a tunnel speed of 25 ft/sec, but tracker lock-on could not be maintained.

The coordinate system shown in Figures 1 and 2 was used as a reference for the data collection. The origin of the coordinate system was at the junction of the foil and the splitter plate as indicated in Figure 2. The location of each measurement point was given in millimeters to allow use of the traverse table software. The area forward of the sail was surveyed on the plane of symmetry using a two dimensional grid of six horizontal points and three vertical points. The size of the grid was set to incorporate the significant portion of the junction vortex. The boundary layer was sampled at a position 255 mm

upstream of the foil, the same location used to measure the boundary layer profiles given in Appendix A. The free stream data was collected in the test section with only the splitter plate installed.

The data collected by the analog-to-digital acquisition system was placed on floppy disks for off-line analysis. The first step of the analysis was to put each data file through a digital 4th-order Butterworth bandpass filter. For most of the spectra in Appendix B, the bandpass filter was set at 10-1000 Hz. The upper limit was set to match the setting of the analog low-pass filter of the signal conditioner in the acquisition system. Once again, the value of this cutoff was determined from the Nyquist frequency. The lower limit was chosen to remove low frequency fluctuations in the voltage signal caused by fluctuations in the tracker data rate. Figures 8 and 9 show the effect of the bandpass filtering.
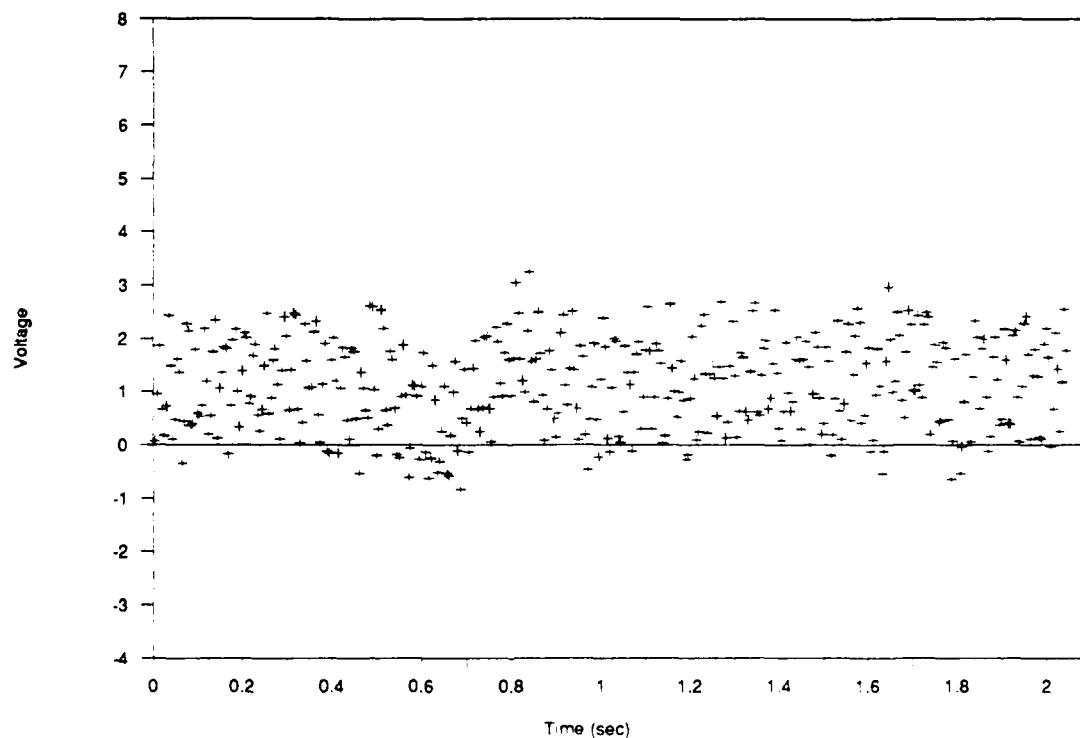
Figure 8.
Unfiltered Data
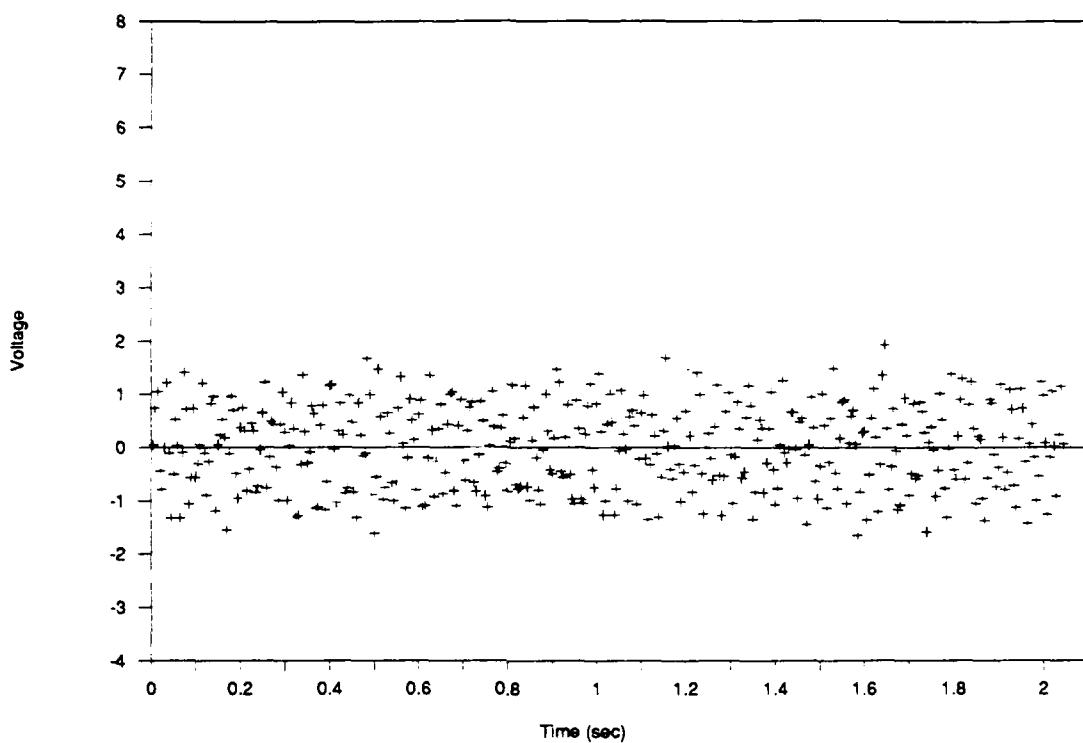
Figure 9.
Data after 10-1000 Hz Bandpass Filter

Figure 8 was produced using the same data as Figure 5, except the data has been time averaged to reduce the clutter of the display. Note the fluctuation in the voltage starting at approximately 0.5 seconds. This was caused by a drop in the tracker data rate. As can be seen in Figure 9, the bandpass filter removed the fluctuation providing smooth data for the spectral analysis. Also note that the mean value or 0 Hz component of the voltage was removed. This was of no consequence since the spectral analysis software would have removed this component prior to generating the spectrum.

The filtered data was then used to generate the power spectral density (PSD) for each measurement point. In all cases, the spectra were normalized to a maximum value of 1.0. Because of this normalization, some of the data files were filtered using a 50-250

Hz bandpass filter and then analyzed to enhance the spectral peaks in the 100 to 200 Hz range. These spectra can also be seen in Appendix B. A Hamming tapered data window was applied to all data files during the analysis to enhance and sharpen the spectral peaks. A typical output of the spectral analysis is shown in Figure 10.
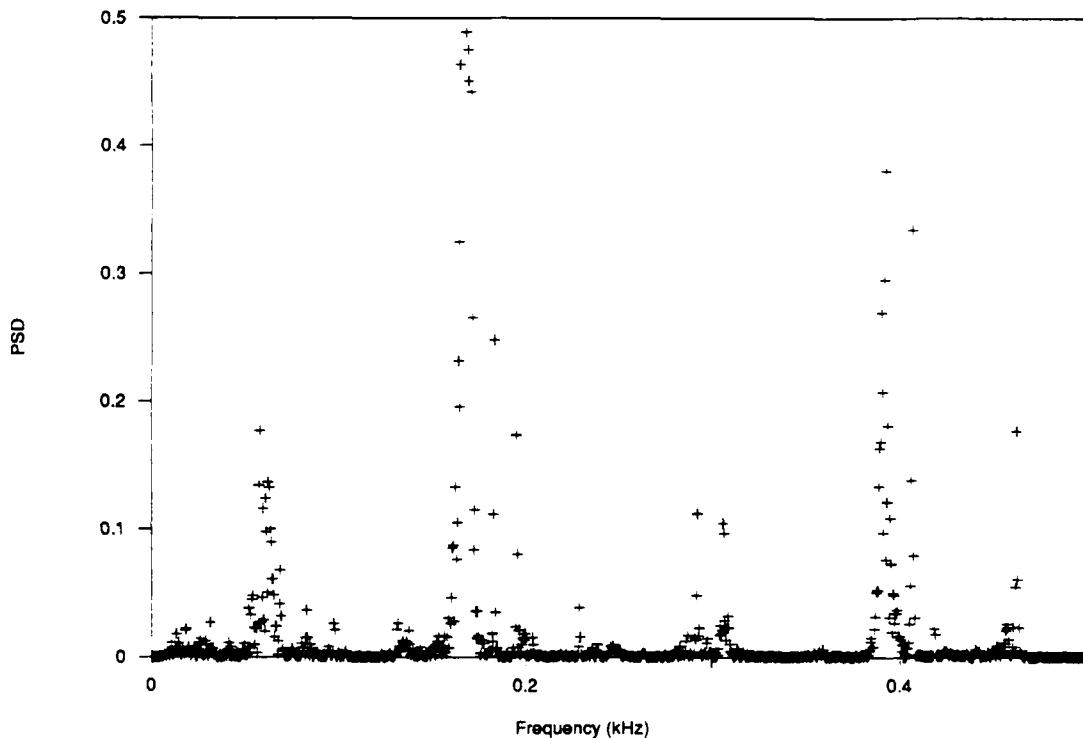
Figure 10.
Power Spectrum using Hamming Window

The final step necessary to produce the smooth spectra in Appendix B was to perform the averages of the adjacent spectral estimates. Five adjacent values were averaged producing the accuracy given in Table II. Figure 11 depicts a final smooth output spectrum.
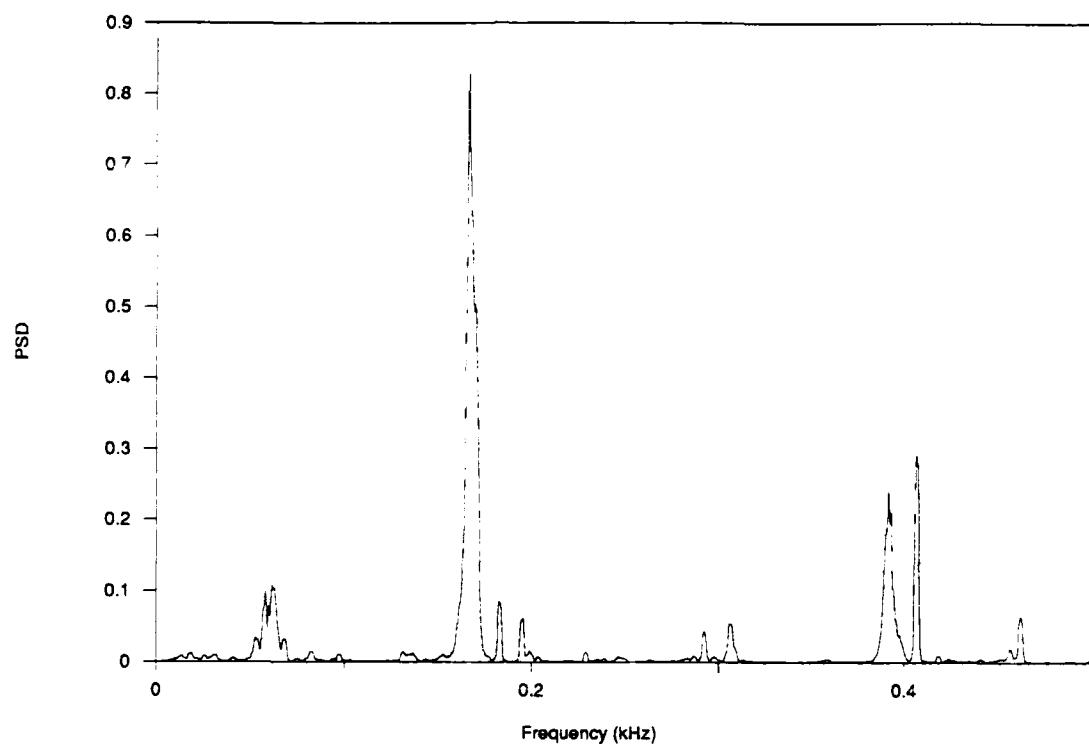
Figure 11.
Smooth Power Spectrum

5 RESULTS

Appendix A contains the measured profiles of the approach boundary layers for tunnel speeds of 10, 20, and 25 ft/sec. As stated before, these profiles were measured at a position 255 mm upstream of the leading edge of the foil on the plane of symmetry. The purpose of these measurements was to insure that a turbulent boundary layer was properly developing along the splitter plate. The flow was tripped just downstream of the leading edge of the plate to induce this development (see Section 2.2).

The curves shown in Figures 12, 13, and 14 are the profiles predicted theoretically assuming a 1/7th power law for the velocity distribution and the measured thickness of the boundary layer. Each experimental data point was determined by averaging the values of 1024 samples taken over a 200 sec time period. The data shows a great deal of scatter, especially at 10 ft/sec, much more than would be expected. The higher the flow rate, the closer the data approaches the predicted profile. In all cases, the measured data generally follows the predicted velocity profile; therefore, the boundary layers were accepted as satisfactory for the remainder of the study.

The first group of spectra in Appendix B are those for the free stream at 10, 20, and 25 ft/sec. At least two measurements were made and analyzed at each speed to determine the reproducibility of the spectra from the digitized analog data. These spectra also serve as a baseline to which the spectra in the boundary layer and junction region can be compared.

The consistency of the free stream spectra at 10 and 20 ft/sec is limited. In both cases, the approximate size and number of frequency peaks are similar between measurements, but the location or frequencies of the peaks appear shifted. The magnitude and direction of the shift varies depending on the frequency, possibly indicating that the source of these various frequencies is not common to all. The majority of the peaks do not shift by more than 50 Hz,

but there are some exceptions. If the first spectrum from 10 ft/sec is neglected, the remaining two are almost exactly alike with the exception of the frequency shifts, especially in the 500 Hz to 1000 Hz region.

The collection of spectra generated using the data from the boundary layer and junction region are extremely disappointing. They appear to contain very little, if any, quantitative information. In view of the inconsistency of the free stream spectra, no particular frequencies can be isolated with any degree of accuracy. All attempts to correlate a spectrum within the junction region with other spectra in the region, the boundary layer, or the free stream prove unsuccessful. No distinct frequencies or frequency pattern can be identified and directly attributed to the flow within the region.

A small amount of qualitative information may be extracted from the spectra despite their limitations. Near the plate ($Z = 1mm$), at a tunnel speed of 10 ft/sec, the spectrum for $X = 5mm$ indicates a very insignificant distribution of energy in the frequency range of interest (0-500 Hz). This spectral energy distribution changes significantly, however, as the position of measurement point moves away from the leading edge of the foil along the plane of symmetry. The spectrum from data taken at $X = 10mm$ shows a large increase in all spectral components producing numerous frequency spikes. Based on the predictions of previous studies and knowing the location of the flow's stagnation point from mean velocity measurements, this position is close to the core of the junction vortex. As the measurement point continues to move away from the leading edge, the trend appears to reverse resulting in lower average spectral levels as the spectra approach the levels found in the boundary layer.

It is difficult to confirm the above trend in spectral energy levels from the data gathered at 20 ft/sec. In general, the levels measured in the junction region at this tunnel speed are significantly lower than those recorded at 10 ft/sec.

The velocity probability distributions in Appendix C are much more conclusive in providing useful information on the nature of the junction flow. These distributions were created using the new digital flow analyzers in conjunction with the laser doppler system. The low data rate, which made these analyzers impractical for the spectra development, was not a factor in this portion of the study. The IFA's inherent accuracy, however, was crucial for this part of the investigation. The distributions in Appendix C clearly show the bi-modal characteristic in the structure of the junction root vortex.

The velocity probability distribution of the free stream at 10 ft/sec is exactly what would be expected. The shape is Gaussian with a very small standard deviation. The slight unsymmetrical nature of the curve about the mean is caused by the input filter settings of the IFA. The turbulence intensity calculated from this distribution is less than 0.5 percent when adjusted for the phase noise of the laser signal. The distribution in the boundary layer is also a Gaussian curve with a larger standard deviation caused by the increased turbulence in this region.

The velocity probability distributions within the junction region are unlike those of the free stream and boundary layer. In all cases, the distributions appear to be the sum of two Gaussian distributions displaying two distinct peaks. The relative strength of the two peaks, as expected, is dependent on the distance away from the leading edge of the foil. By following the progression of figures in Appendix C, it is obvious that the larger peak shifts from a negative velocity behind the stagnation point to a positive velocity as the stagnation point is crossed. The presence of two peaks is indicative of two distinct flow velocities existing over time at the measurement point confirming a bi-modal structure.

The velocity probability distribution results obtained at a tunnel speed of 20 ft/sec are the same as those acquired at 10 ft/sec. The bi-modal characteristic of the flow structure is even more pronounced at this tunnel speed. The two distinct peaks are clearly visible at X = 5mm and X = 10mm.

6 CONCLUSIONS AND RECOMMENDATIONS

The conclusions that can be drawn from this experimental study of the junction root vortex are not as extensive as originally expected. The results of the velocity probability distributions clearly confirm the presence of the bi-modal characteristic within the structure of the junction vortex as stated by Simpson. The spectral studies, however, provide no clear information about the flow except to indicate an increase in the spectral energy distribution in the vicinity of the vortex. The frequency of fluctuation of the bi-modal structure or any other distinctive frequency pattern caused by the flow cannot be identified from the spectra obtained in this investigation.

The ability to use data from MIT's laser doppler anemometry system to obtain spectral information is still questionable and requires further study. The accuracy of the data gathered using the IFA's could significantly improve the quality of the spectral output if sufficient data rates could be obtained.

The following is a list of recommended procedures for further investigation. Some of these procedures relate directly to the investigation of the junction vortex, while others broadly apply to the use of the laser doppler system for time-frequency studies:

1. Conduct on-line frequency analysis of the laser doppler signal using a spectrum analyzer and the analog output of a signal processor[9]. The sample-and-hold nature of both the tracker and IFA must be taken into account. A sufficient data rate, depending on frequencies of interest, must be achievable to assume a continuous input signal to the analyzer.

2. Improve the data rates obtainable with the IFA to allow the collection of

---

9 Although the primary output of an IFA is digital information, an analog output is available from a connection on the back panel of the processor.

accurate digital information for off-line spectral analysis within a useful frequency range.

3. If sufficient data rates can be obtained from the IFA's on both the horizontal channel and fiber optic (third component) channel, attempt to cross-correlate fluctuations in the junction region with fluctuations in the free stream or boundary layer.

4. Improve the accuracy of the spectra by averaging a larger number of adjacent spectral estimates. A σ/m of ten percent can be obtained by averaging 100 adjacent values.

5. Average a large number of spectra generated from sets of data taken at the same point over time. This may help to reduce the fluctuations in the spectra, as indicated in the free stream cases, allowing only significant frequency components to emerge.

REFERENCES

1. Baker, C.J. "The Turbulent Horseshoe Vortex." *Journal of Wind Engineering and Industrial Aerodynamics*. Vol. 6. Nos. 1-2, July 1980.

2. Belik, L. "The Secondary Flow about Circular Cylinders Mounted Normal to a Flat Plate." *Aeronautical Quarterly*. Vol. 26., February 1973.

3. Devenport, W.J. and R.L. Simpson. "Some Time-Dependent Features of Turbulent Appendage-Body Juncture Flows." Paper presented at 16th Symposium on Naval Hydrodynamics, July 1986.

4. Dickinson, S.C. "Flow Visualizations and Velocity Measurements in the Separated Region of an Appendage-Flat Plate Junction." DTNSRDC Report 86/020, March 1986.

5. Dickinson, S.C. "An Experimental Investigation of Appendage-Flat Plate Junction Flow." DTNSRDC Report 86/051, December 1986.

6. Durst, F., A. Melling, and J.H. Whitelaw. *Principles and Practice of Laser Doppler Anemometry*. 2nd ed. New York: Academic Press, 1981.

7. Kerwin, Justin E. "Variable Pressure Water Tunnel." Paper presented to the New England Section of the Society of Naval Architects and Marine Engineers, October 1967.

8. Kubendran, L.R. "Study of Turbulent Flow in a Wing-Fuselage Type Junction." Ph.D. Dissertation, Georgia Institute of Technology, April 1983.

9. Love, R.H. "An Investigation of the Effect of the Wall Boundary Layer on the Wake of an Obstacle Protruding from the Wall." University of Maryland Technical Note BM-370, August 1963.

10. McHahon, H., J. Hubbart, and L.R. Kubendran. "Mean Velocities and Reynolds Stresses in a Juncture Flow." NASA contractor Report 3605, 1982.

11. McHahon, H., J. Hubbart, and L.R. Kubendran. "Mean Velocities and Reynolds Stresses Upstream of a Simulated Wing-Fuselage Juncture." NASA contractor Report 3695, June 1983.

12. Newland, D.E. *An Introduction to Random Vibrations and Spectral Analysis*. 2nd ed. New York: Longman, Inc., 1984.

13. Oguz, E.A. "An Experimental Investigation of the Turbulent Flow in the Junction of a Flat Plate and a Body of Constant Thickness." Ph.D. Thesis, Georgia Institute of Technology, December 1980.

14. Pierce, F.J. and J.E. McAllister. "Near Wall Similarity in a Pressure-Driven Three-Dimensional Turbulent Boundary Layer." Virginia Polytechnic Institute and State University Report VPI-E-80.32, September 1980.

15. Pierce, F.J. and J.E. McAllister. "Measurements in a Pressure-Driven and a Shear-Driven Three-Dimensional Turbulent Boundary Layer." *Three-Dimensional Turbulent Boundary Layers*. Ed. H.H. Fernholz and E. Krause. Springer-Verlag, 1982.

16. Pierce, F.J., M.D. Marsh, and J.D. Menna. "The Mean Flow Structure Around and Within a Turbulent Junction or Horseshoe Vortex." Virginia Polytechnic Institute and State University Report VPI-E-85-19, September 1985.

17. Pierce, F.J., G.A. Frangistas, and D.J. Nelson. "Geometry Modification Effects on a Junction Vortex Flow." Proceedings of the Symposium on Hydrodynamic Performance Enhancement for Marine Applications, November 1988.

18. Rood, E.P. "Experimental Investigation of the Turbulent Large Scale Temporal Flow in the Wing-Body Junction." Ph.D. Dissertation, The Catholic University of America, 1984.

19. Rood, E.P. and J.E.C. Keller. "Evidence of Large Scale Time Dependent Flow in the Wing-Wall Interaction Wake." *Unsteady Turbulent Boundary Layers and Friction*. ASME Publication, FED Vol. 12, 1984.

20. Schlichting, H. *Boundary-Layer Theory*. 6th ed. New York: McGraw-Hill, 1968, 511-12.

21. Shabaka, I.M.M.A. and P. Bradshaw. "Turbulent Flow Measurements in an Idealized Wing/Body Junction." *AIAA Journal*. 81-4028, 1981.

22. Sung, C.H. "Numerical Wake Prediction Methods for Submerged Appended Bodies, A Literature Survey." DTNSRDC Report SPD-1057/01, February 1983.

APPENDIX A.

BOUNDARY LAYER PROFILES
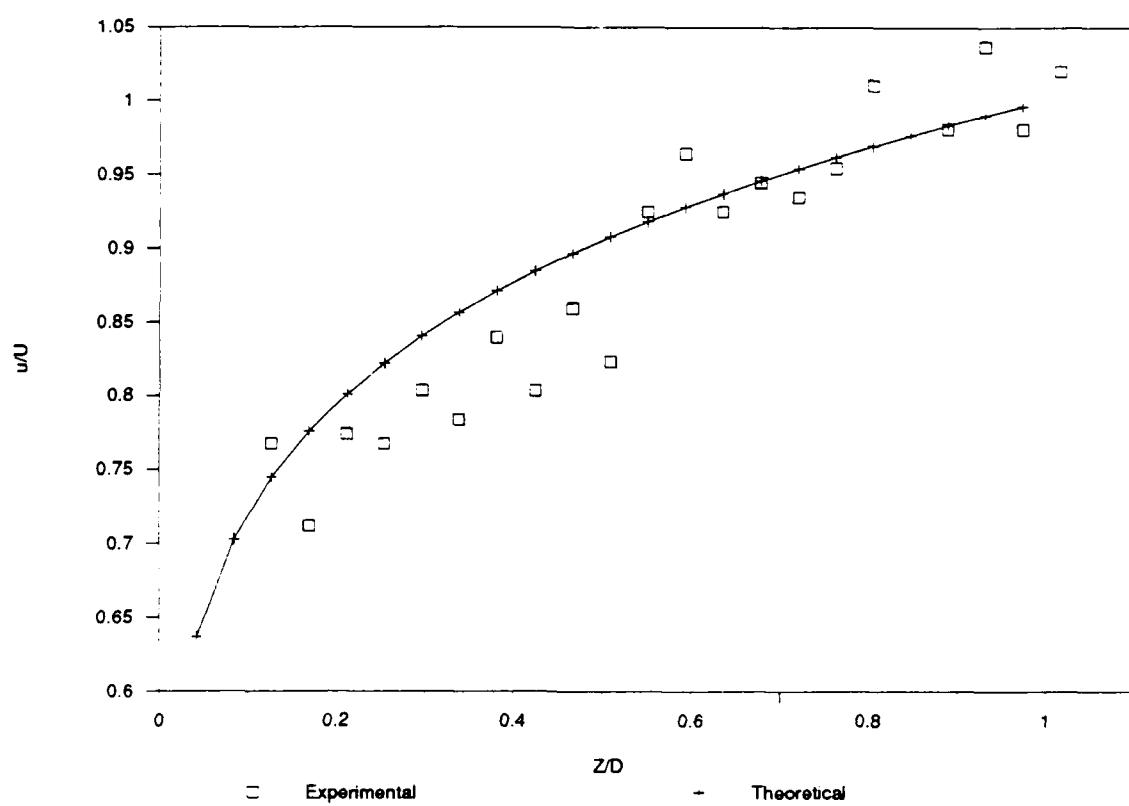
Figure 12.
Boundary Layer Profile (10 ft/sec)
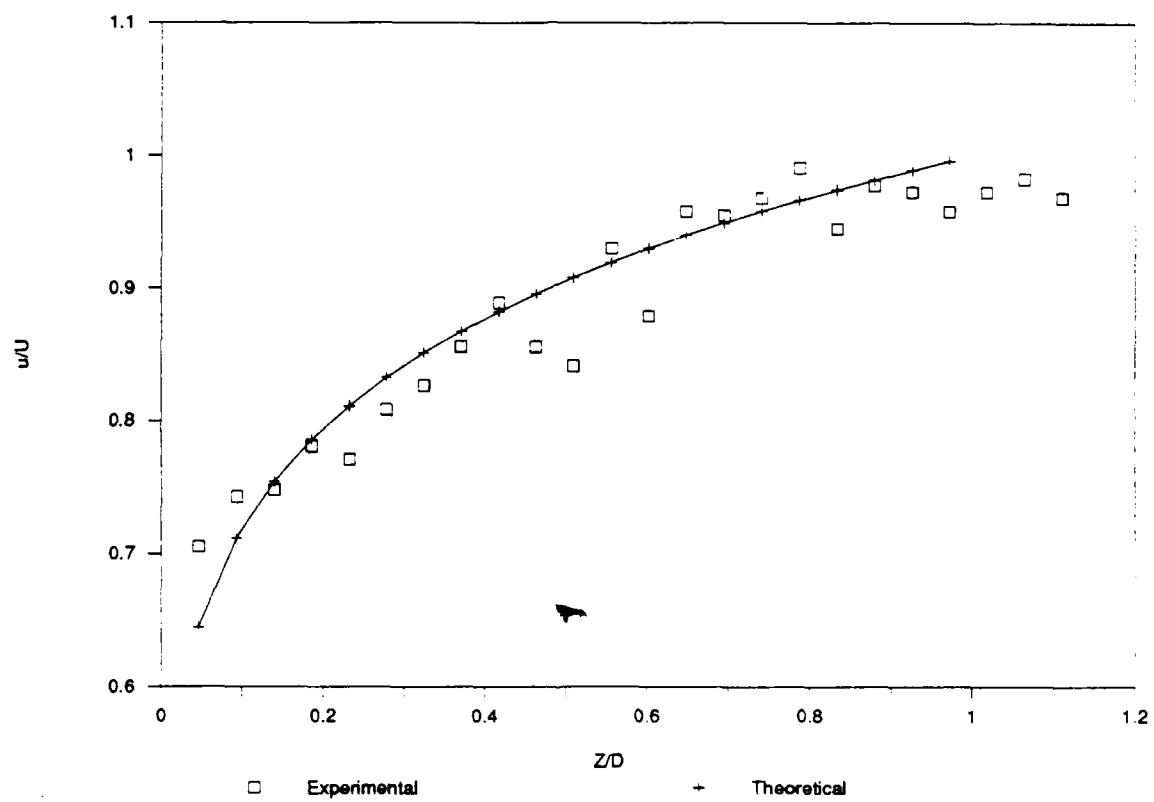
Figure 13.
Boundary Layer Profile (20 ft/sec)
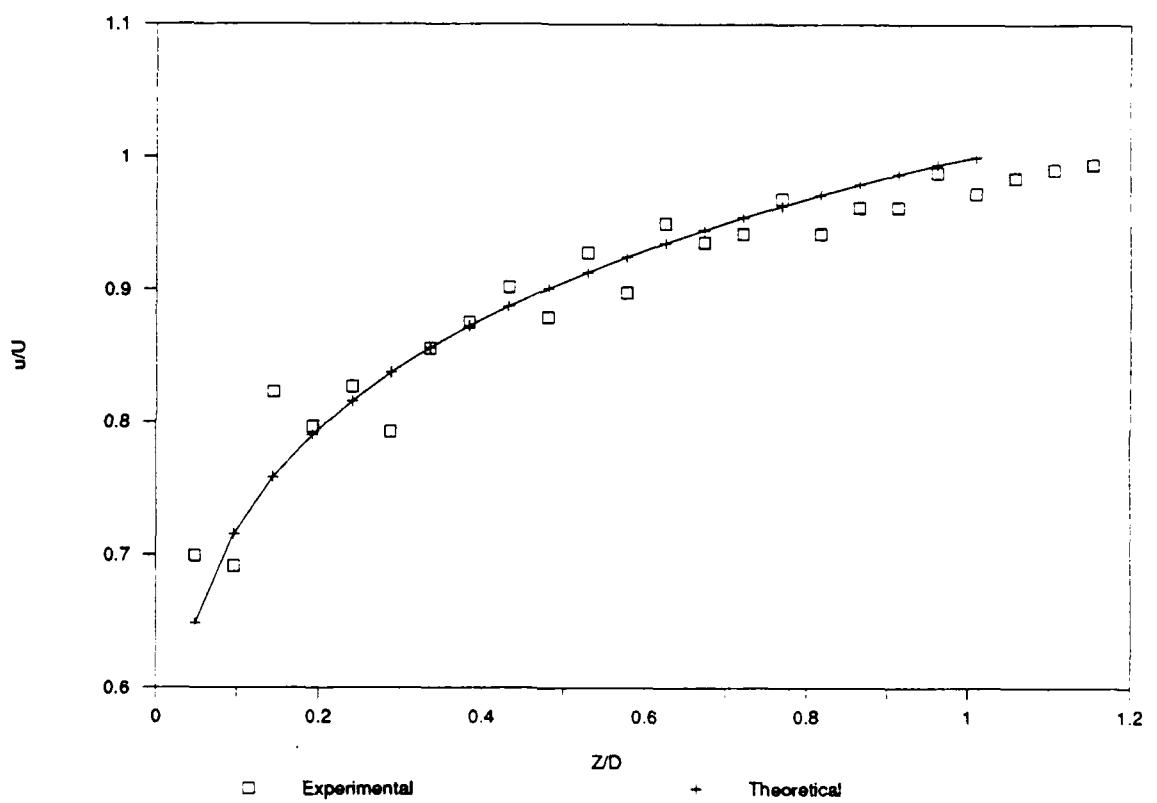
Figure 14.
Boundary Layer Profile (25 ft/sec)

APPENDIX B.

POWER SPECTRAL DENSITIES
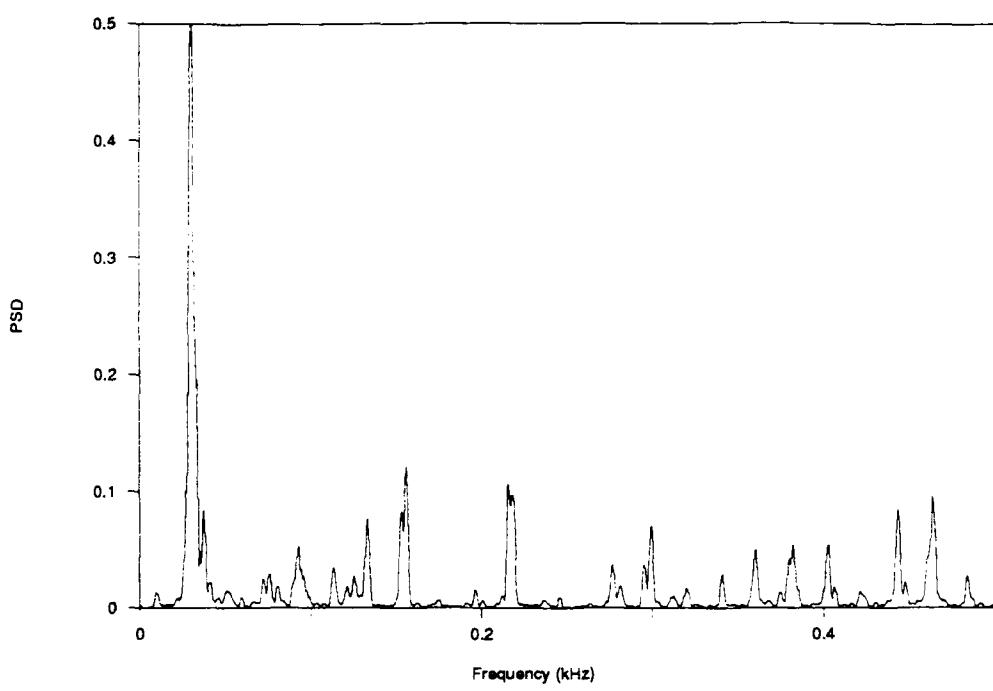
Figure 15.
Free Stream, 10 ft/sec
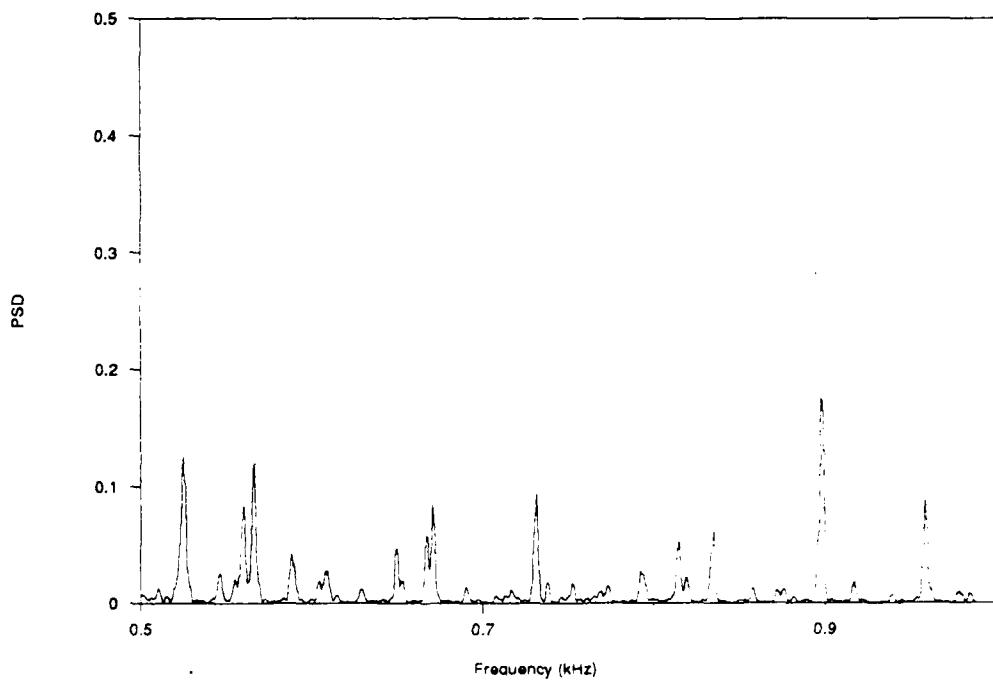
Figure 16.
Free Stream, 10 ft/sec

Page 45
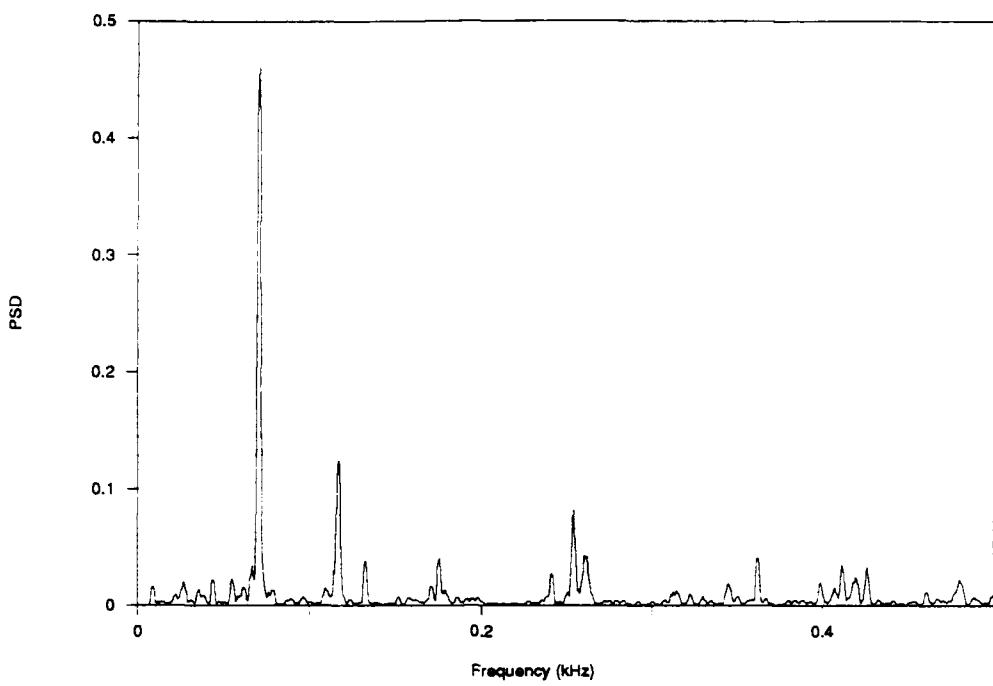
Figure 17.
Free Stream, 10 ft/sec
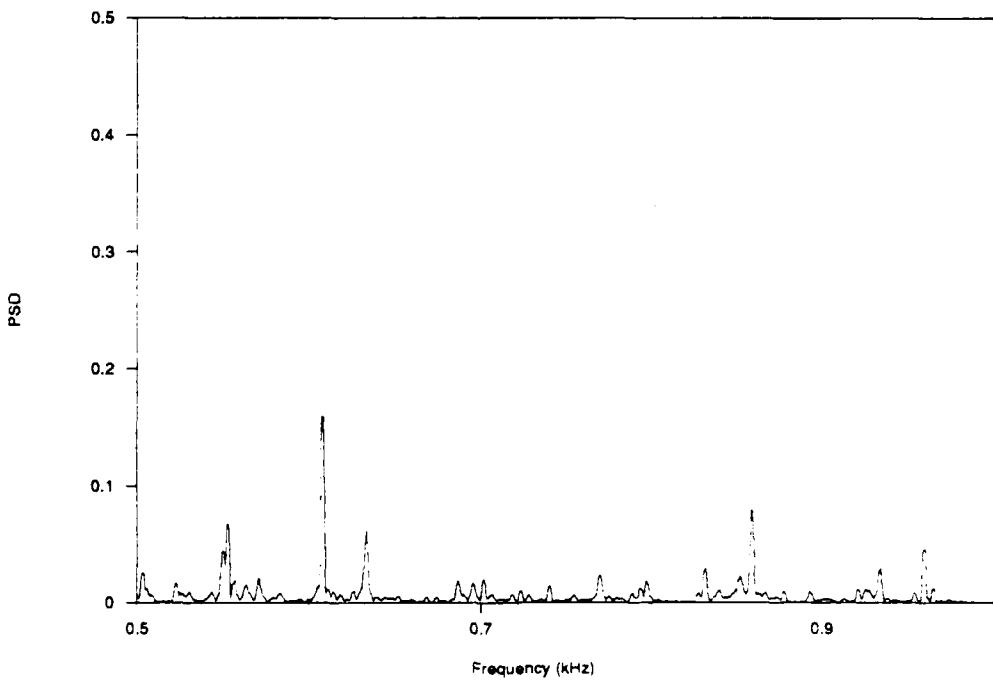
Figure 18.
Free Stream, 10 ft/sec

Page 46
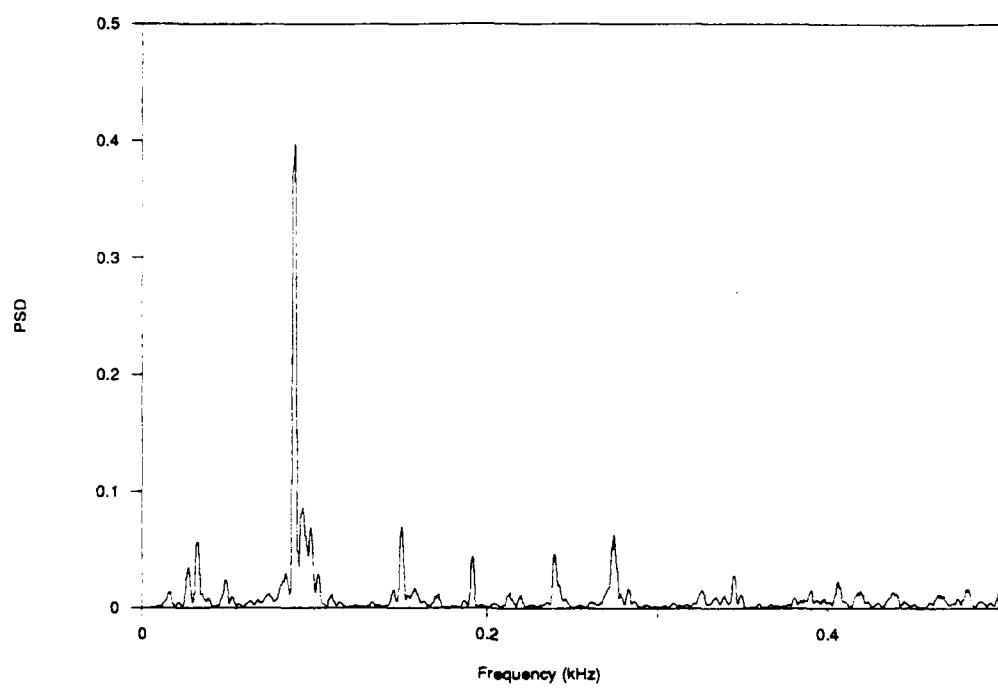
Figure 19.
Free Stream, 10 ft/sec
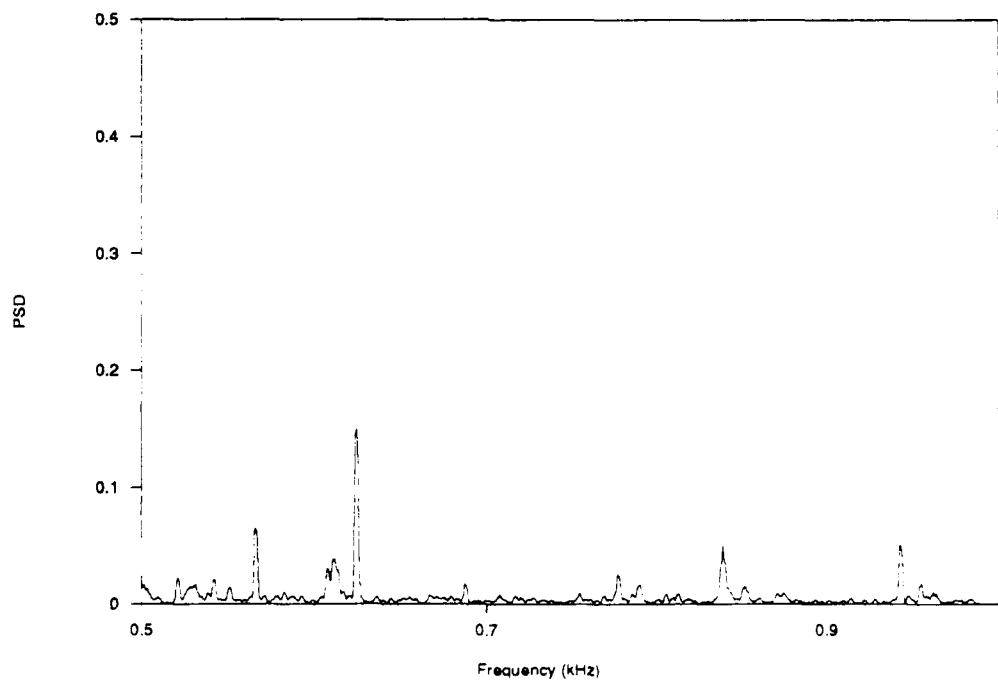
Figure 20.
Free Stream, 10 ft/sec

Page 47
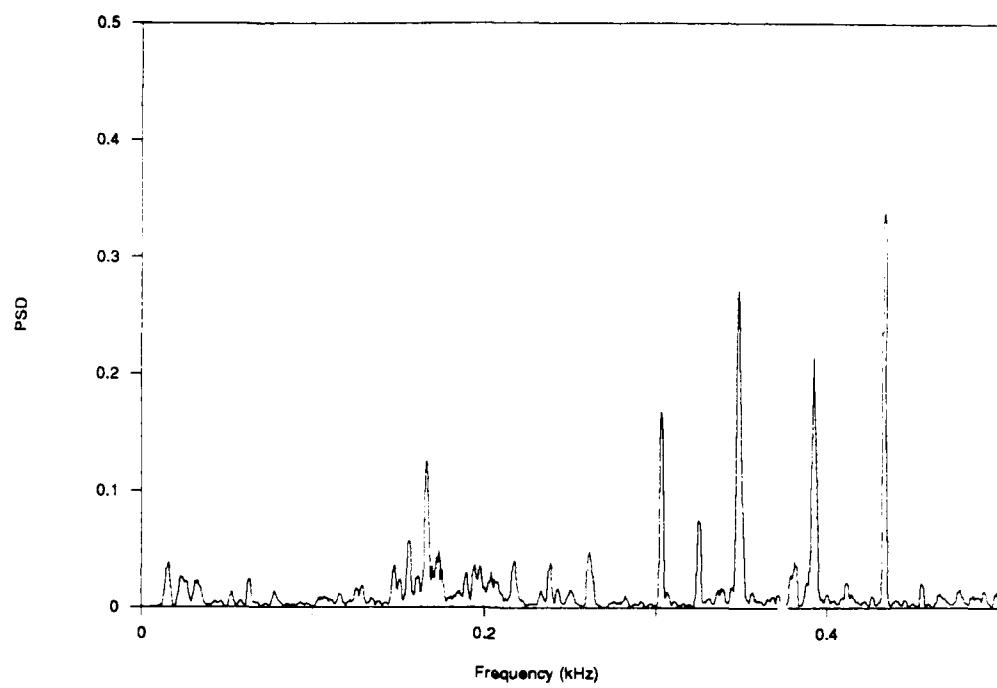
Figure 21.
Free Stream, 20 ft/sec
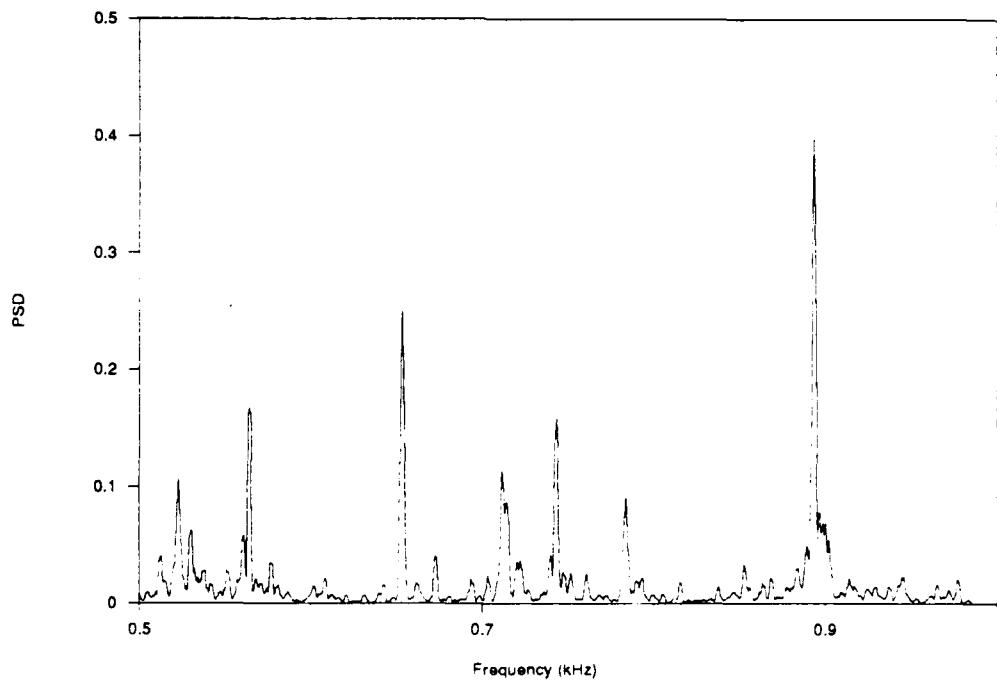
Figure 22.
Free Stream, 20 ft/sec

Page 48
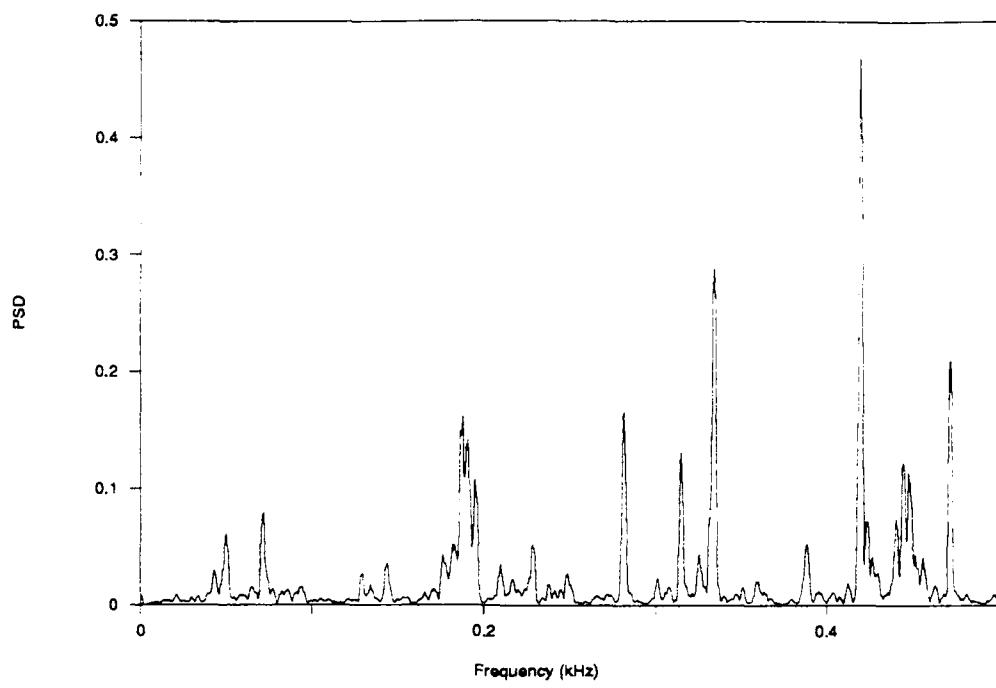
Figure 23.
Free Stream, 20 ft/sec
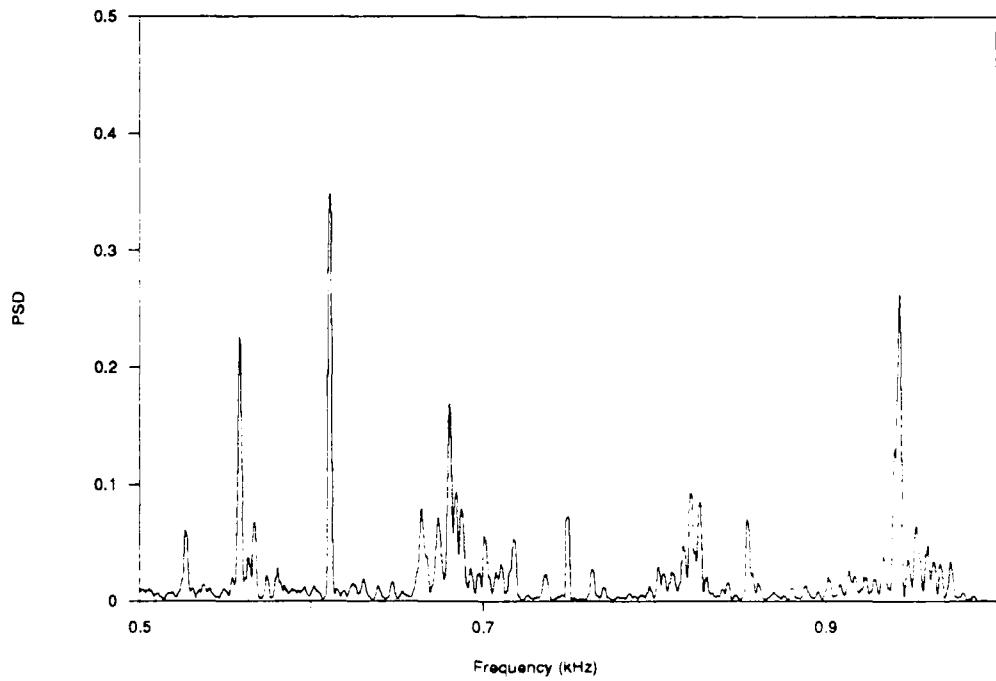
Figure 24.
Free Stream, 20 ft/sec

Page 49
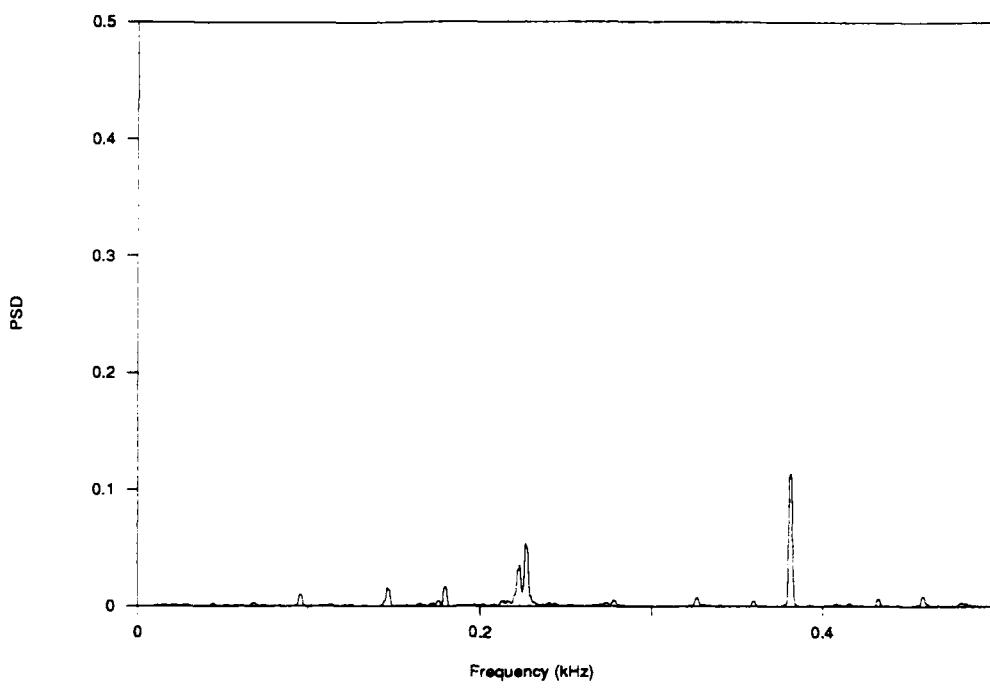
Figure 25.
X=5mm, Z=1mm, 10 ft/sec
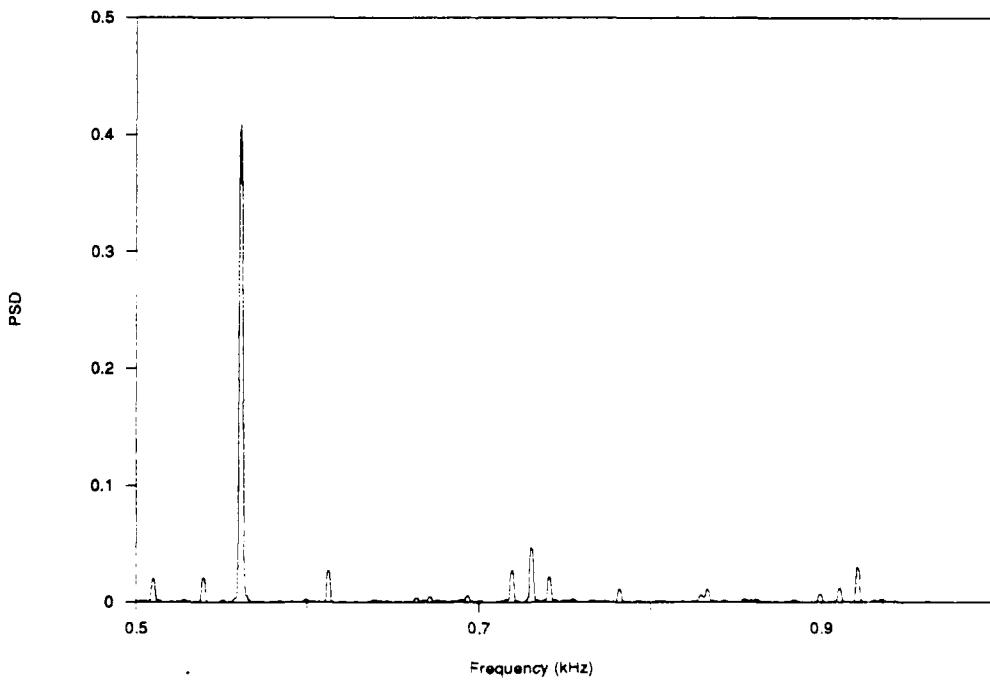
Figure 26.
X=5mm, Z=1mm, 10 ft/sec

Page 50
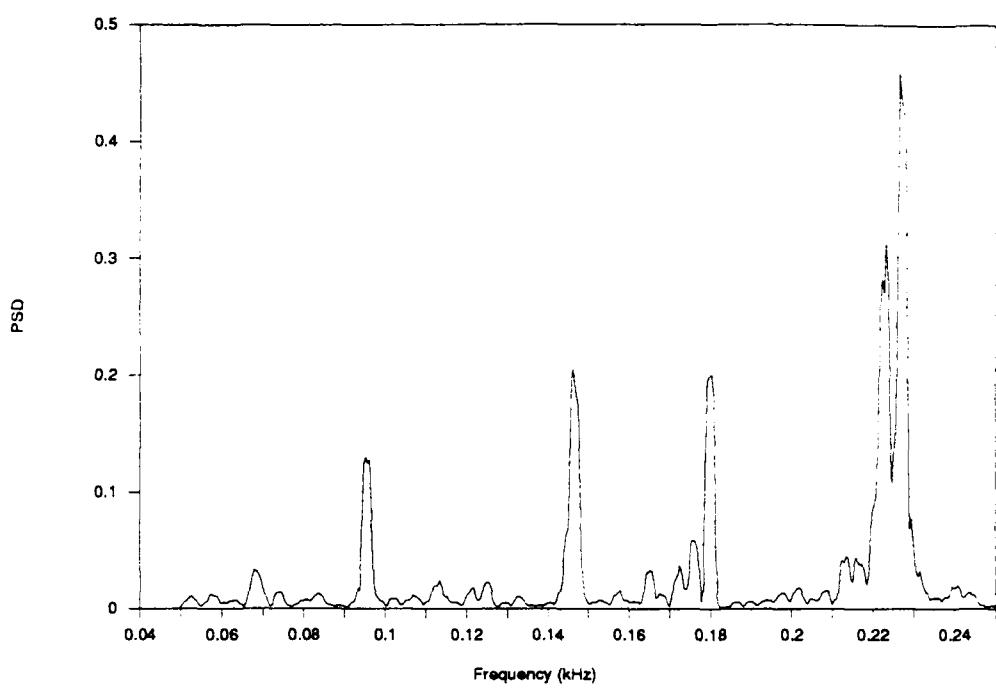
Figure 27.
X=5mm, Z=1mm, 10 ft/sec
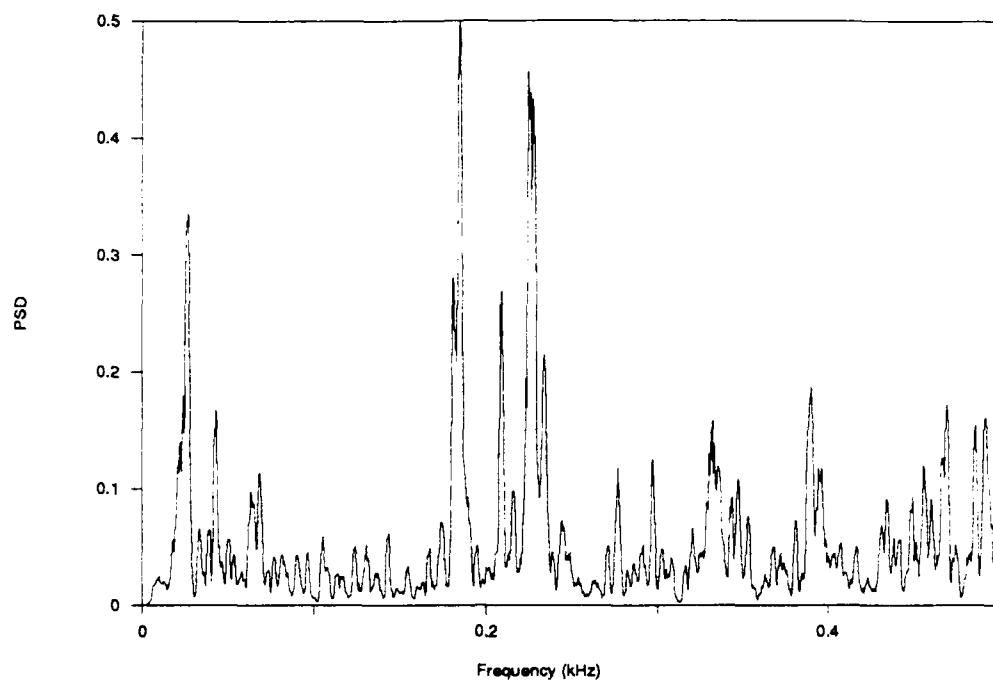
Figure 28.
X=10mm, Z=1mm, 10 ft/sec
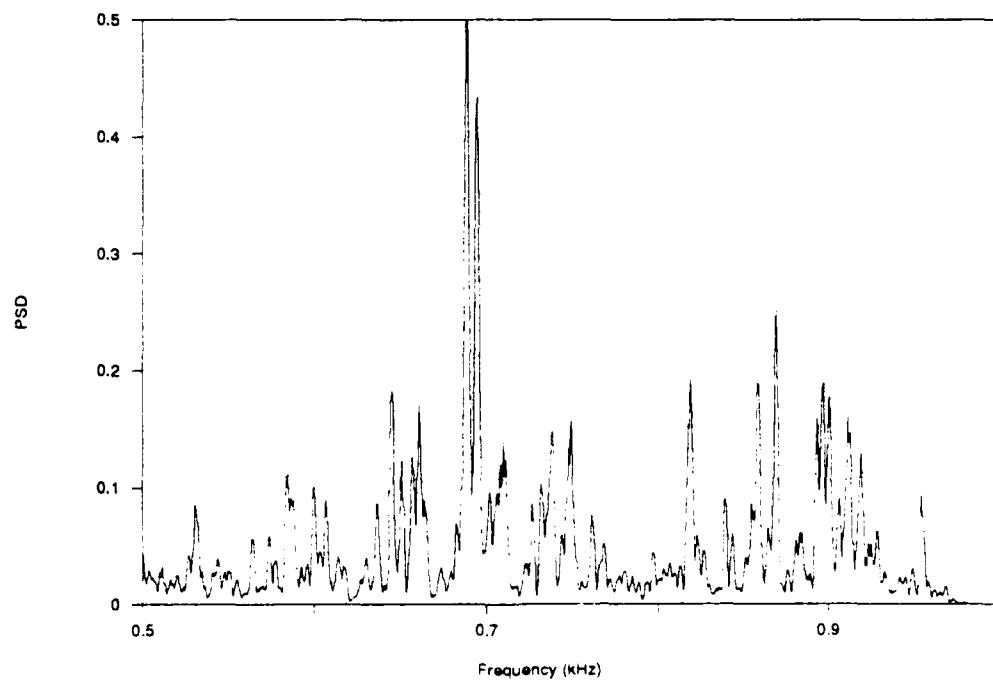
Figure 29.
X=10mm, Z=1mm, 10 ft/sec
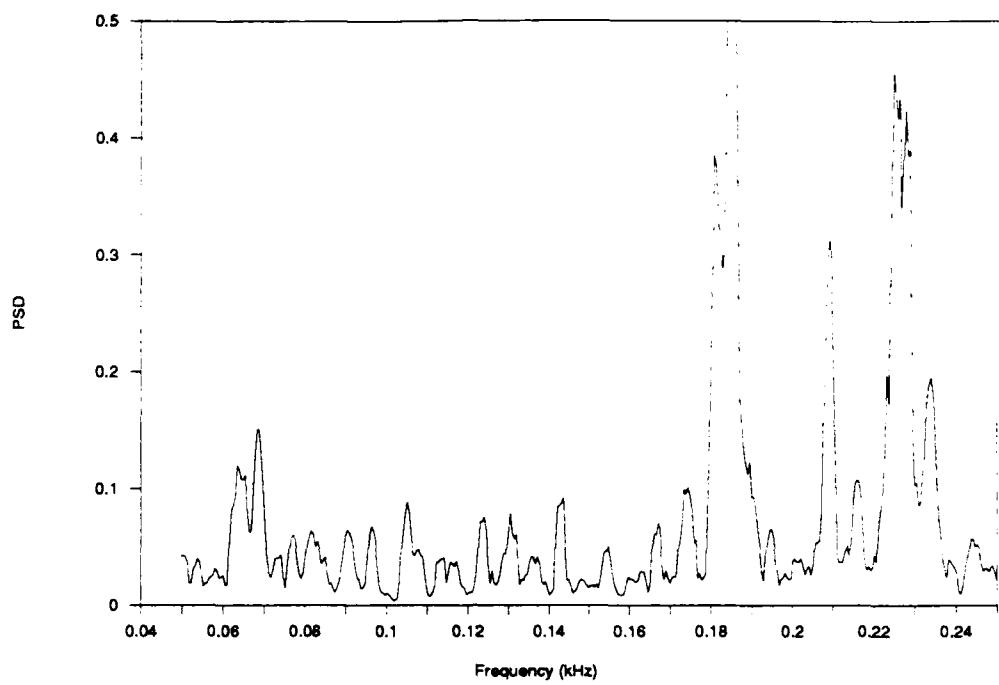
Figure 30.
X=10mm, Z=1mm, 10 ft/sec
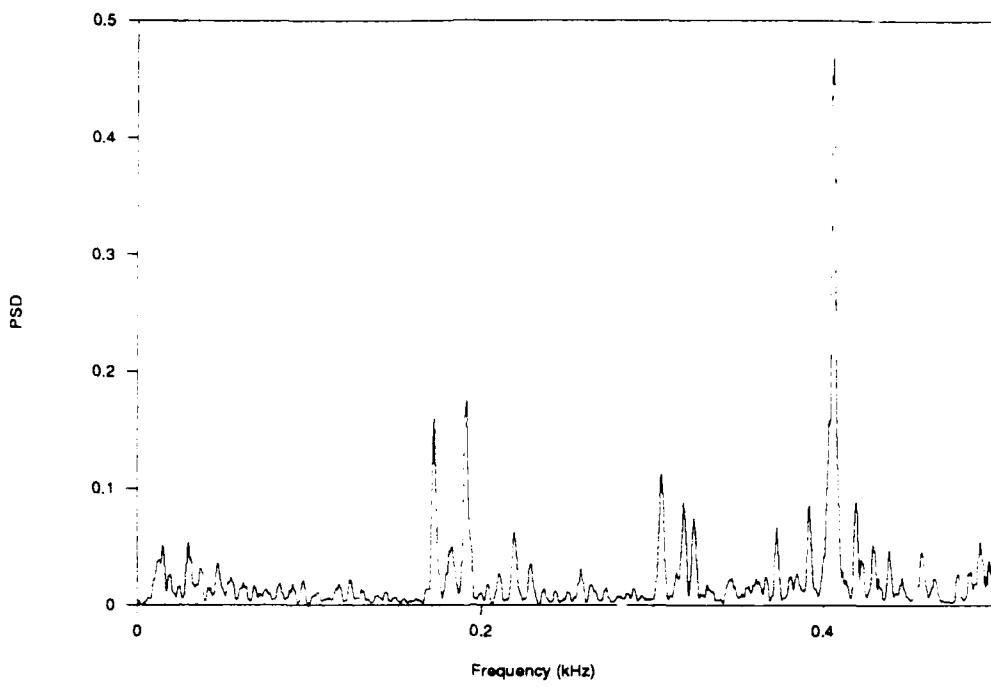
Figure 31.
X=15mm, Z=1mm, 10 ft/sec
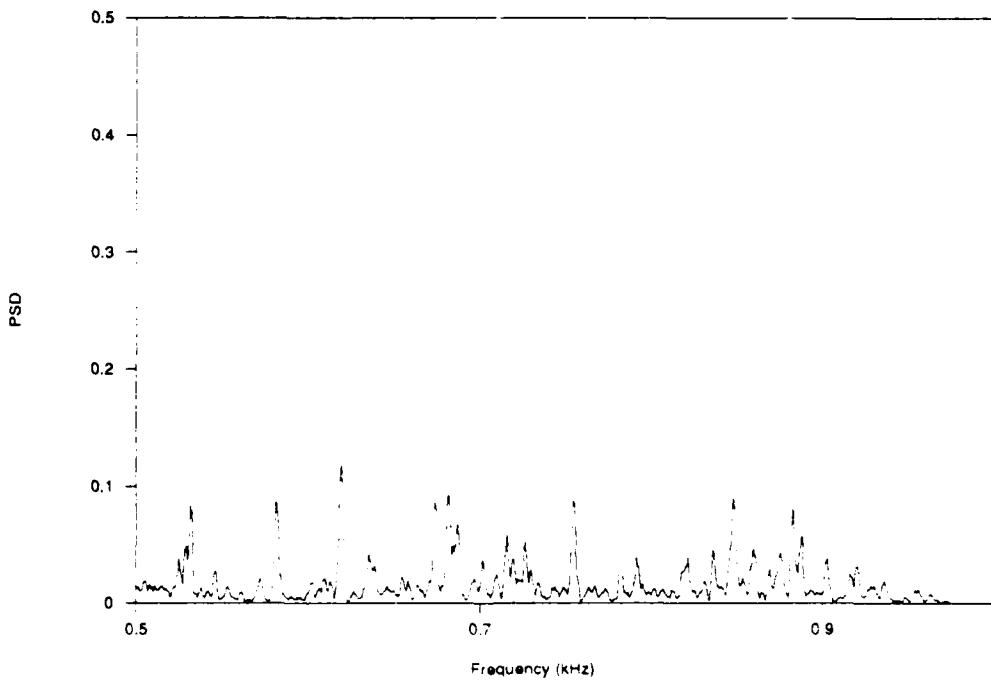
Figure 32.
X=15mm, Z=1mm, 10 ft/sec

Page 54
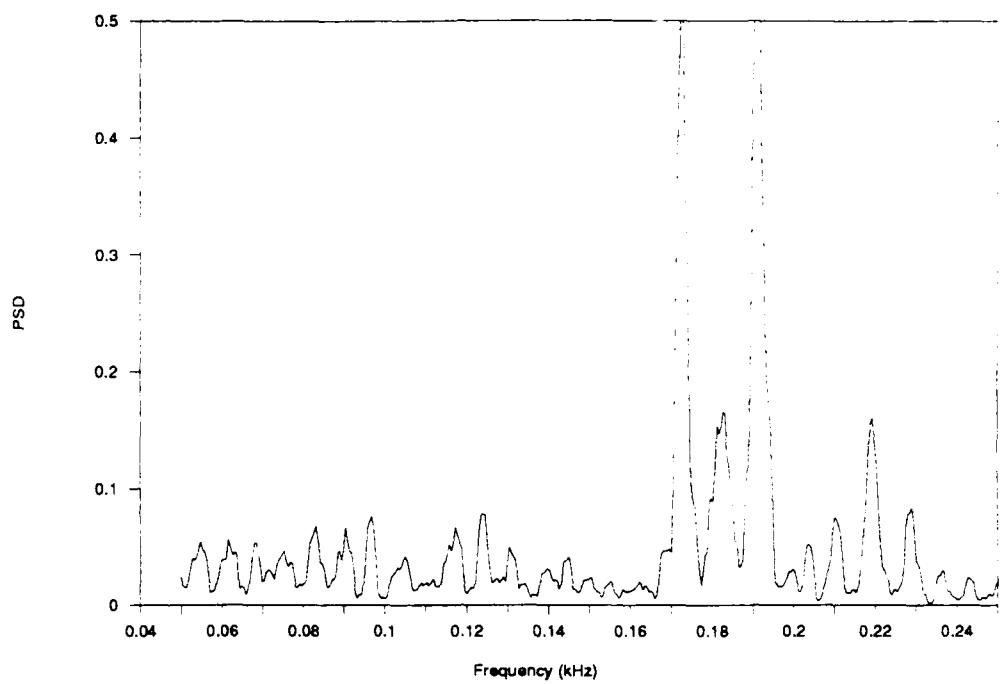
Figure 33.
X=15mm, Z=1mm, 10 ft/sec
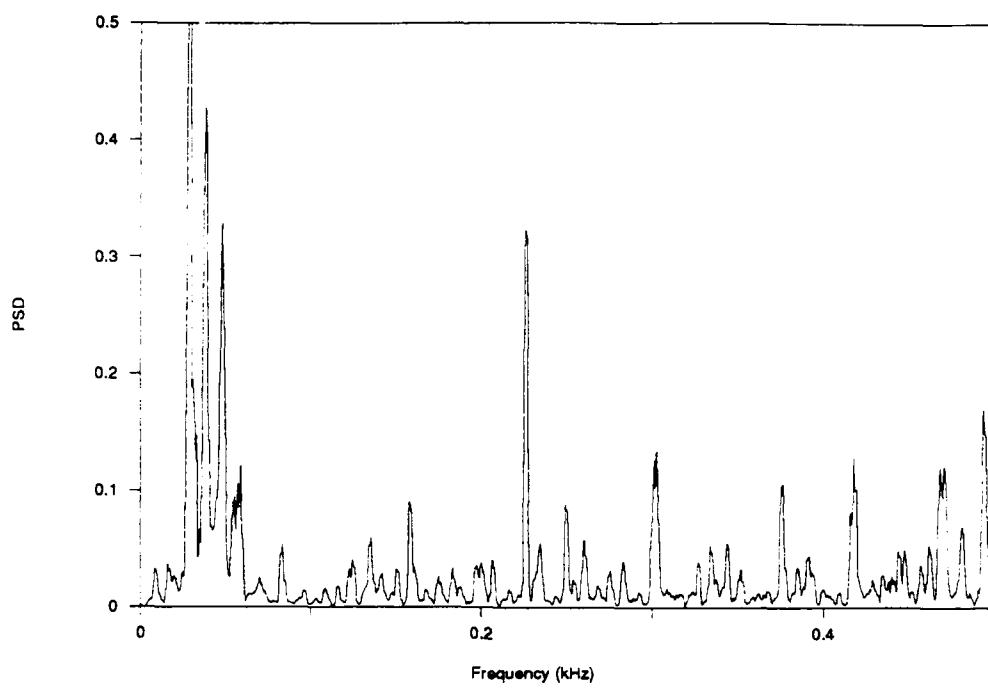
Figure 34.
X=25mm, Z=1mm, 10 ft/sec
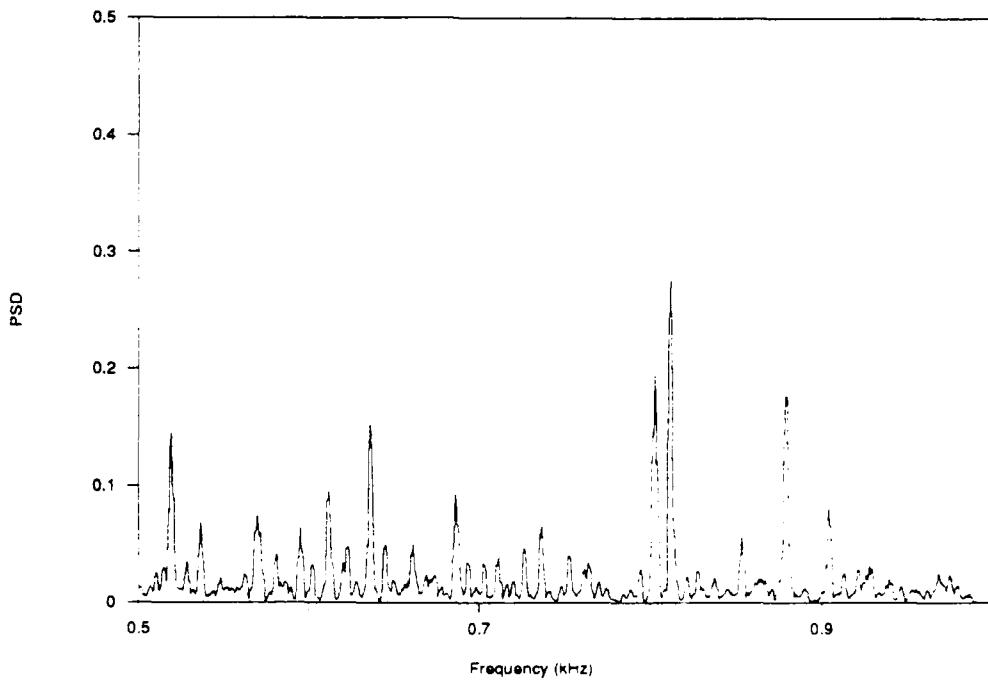
Figure 35.
X=25mm, Z=1mm, 10 ft/sec

Page 56
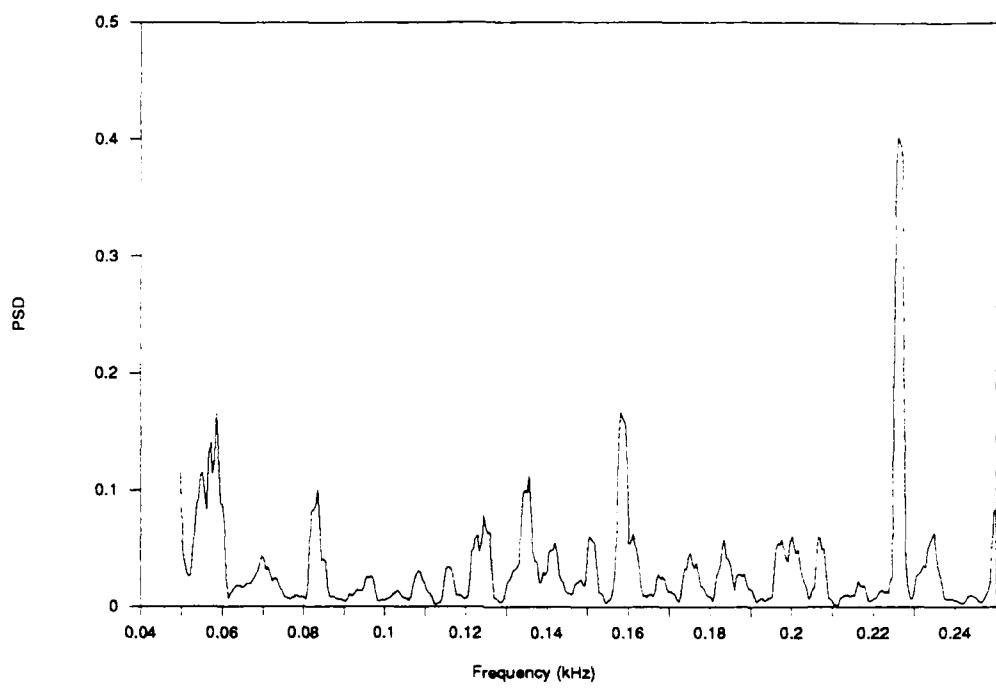
Figure 36.
X=25mm, Z=1mm, 10 ft/sec
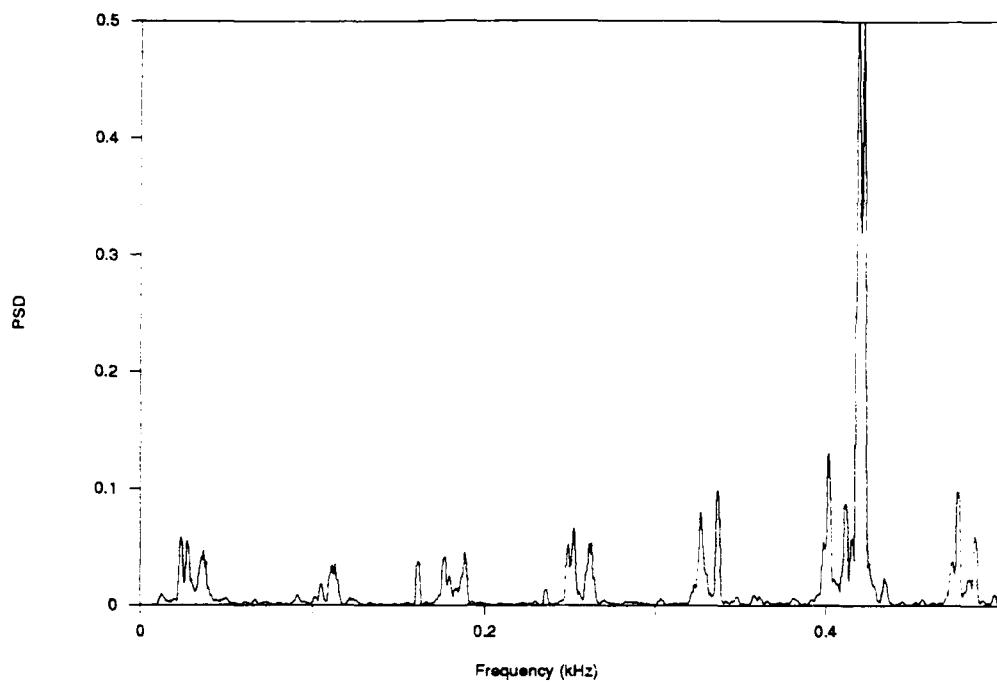
Figure 37.
X=5mm, Z=8mm, 10 ft/sec
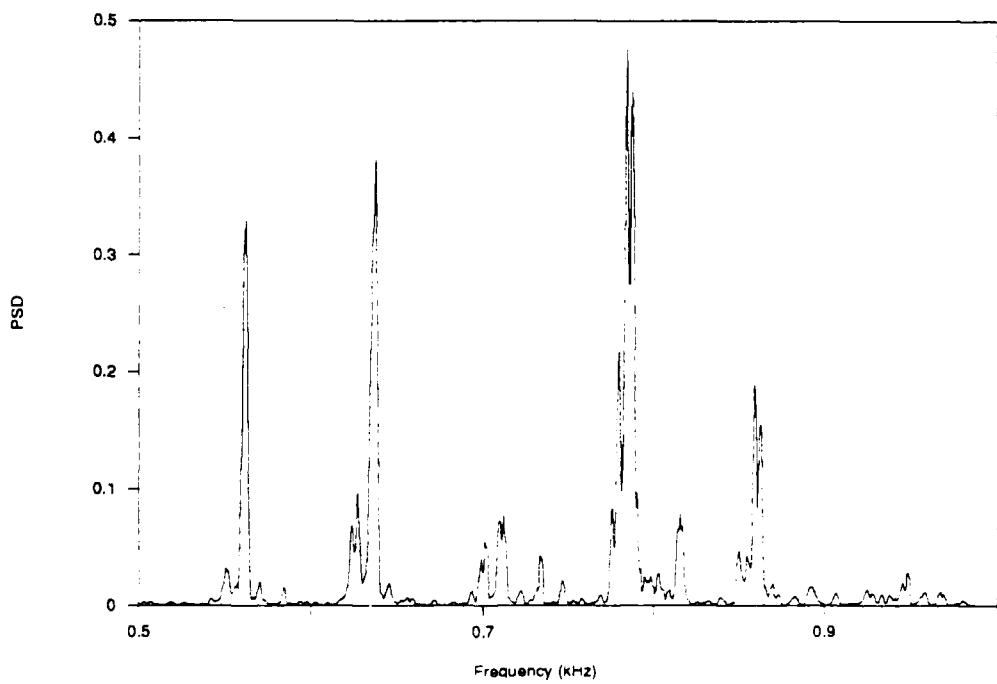
Figure 38.
X=5mm, Z=8mm, 10 ft/sec
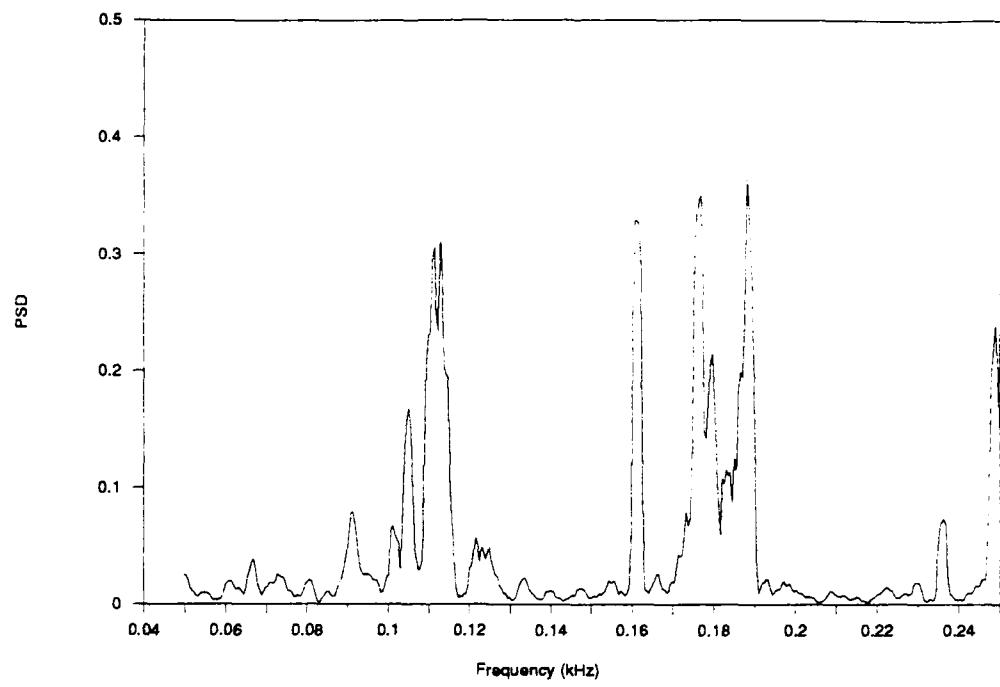
Figure 39.
X=5mm, Z=8mm, 10 ft/sec
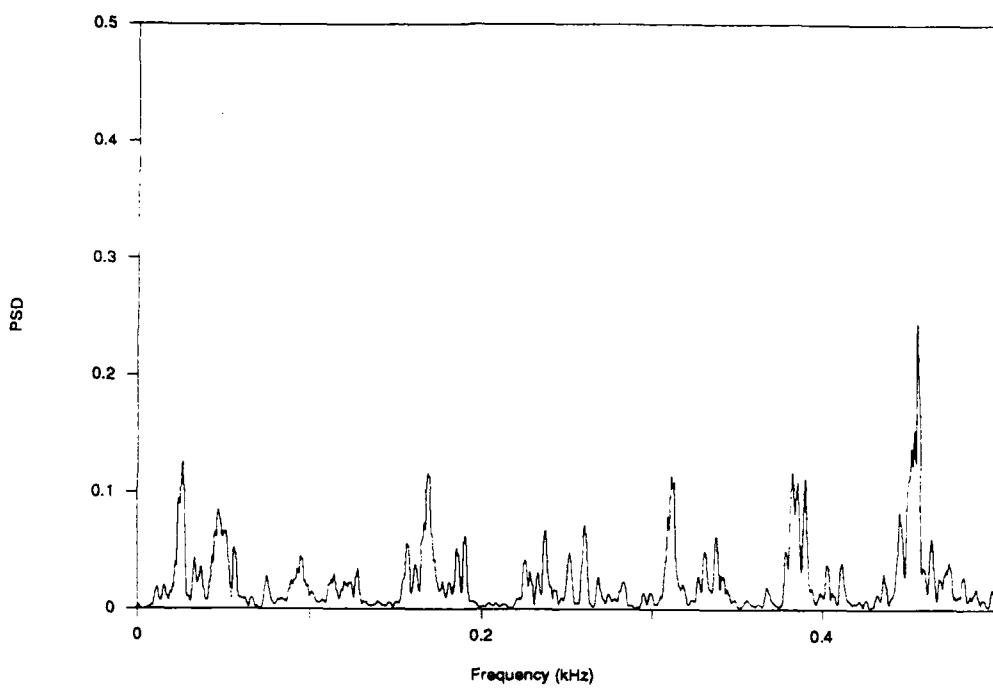
Figure 40.
X=15mm, Z=8mm, 10 ft/sec
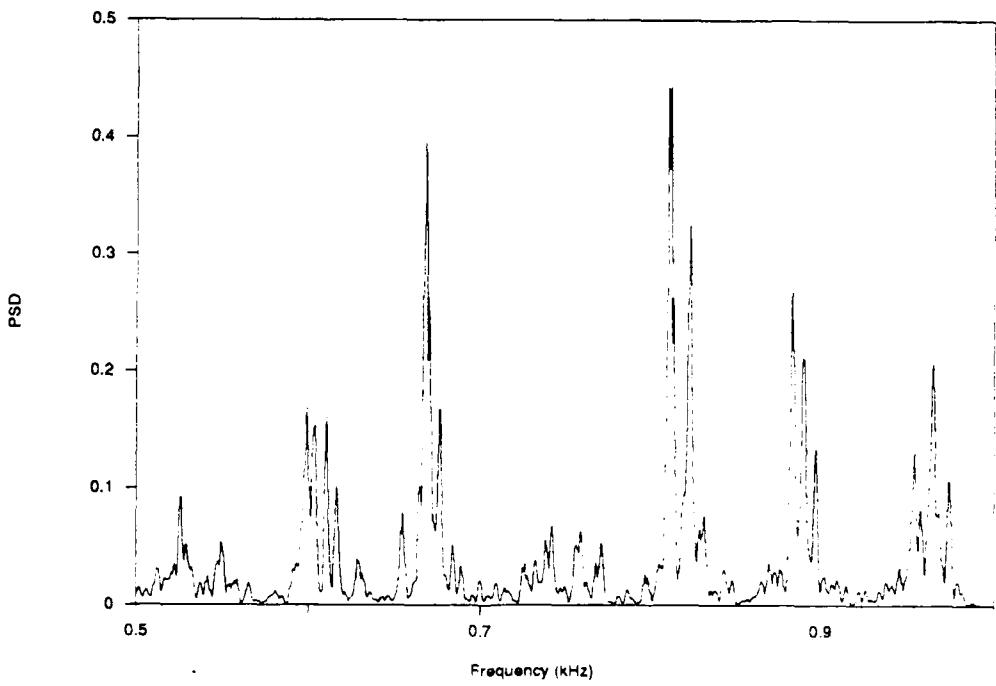
Figure 41.
X=15mm, Z=8mm, 10 ft/sec
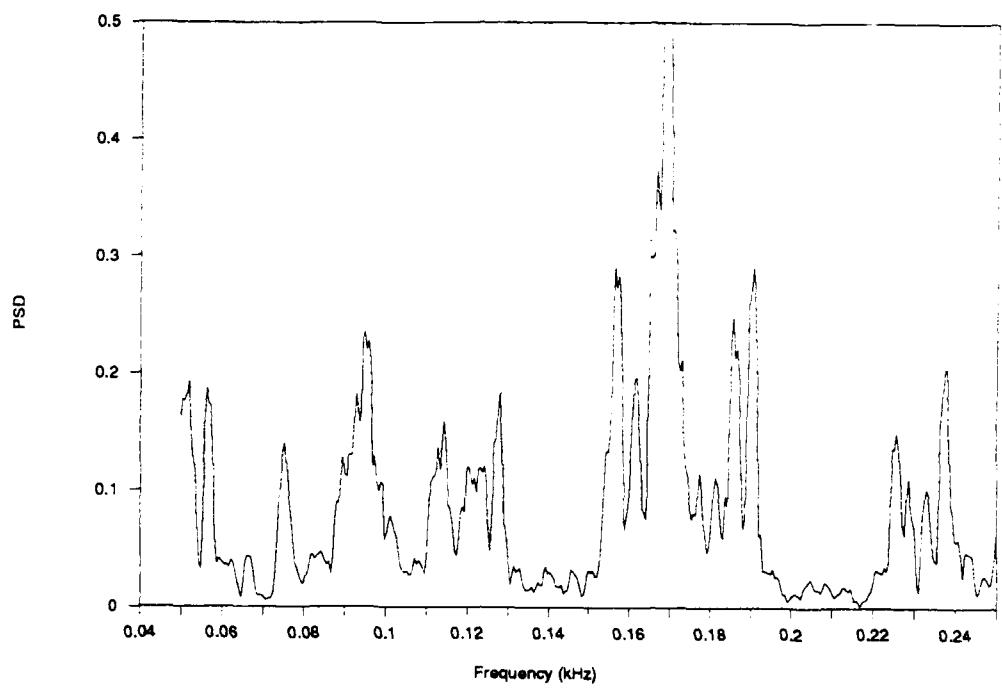
Figure 42.
X=15mm, Z=8mm, 10 ft/sec
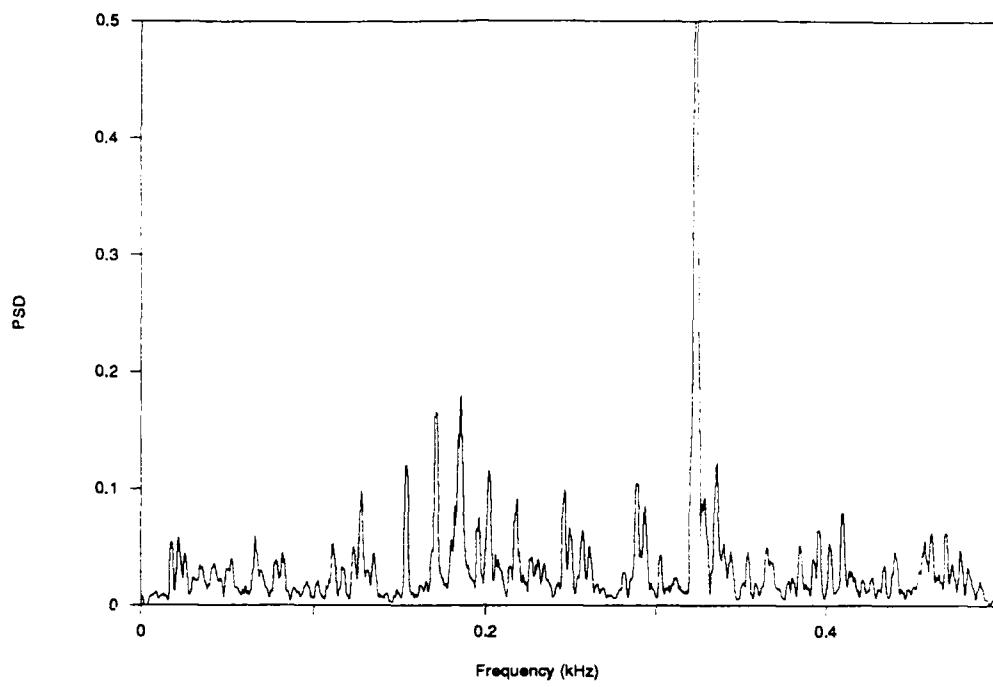
Figure 43.
X=25mm, Z=8mm, 10 ft/sec
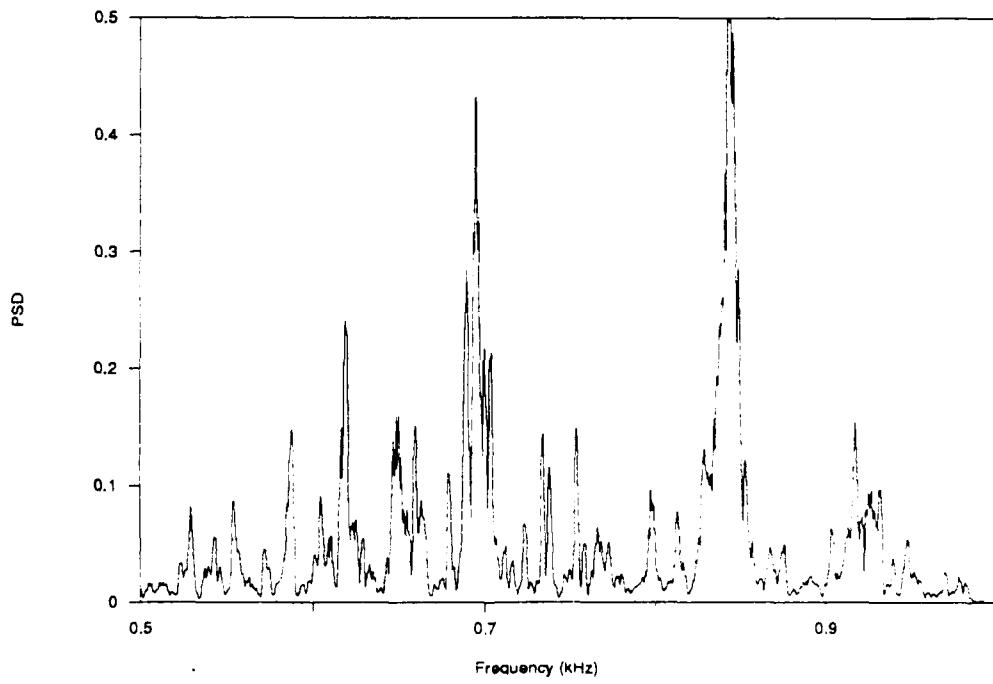
Figure 44.
X=25mm, Z=8mm, 10 ft/sec
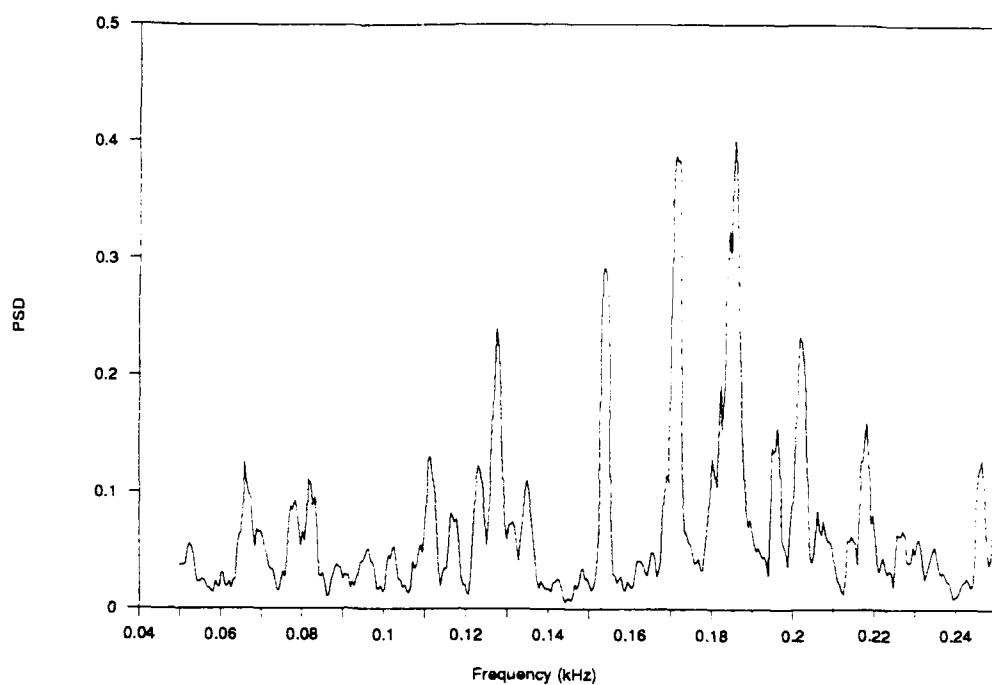
Figure 45.
X=25mm, Z=8mm, 10 ft/sec
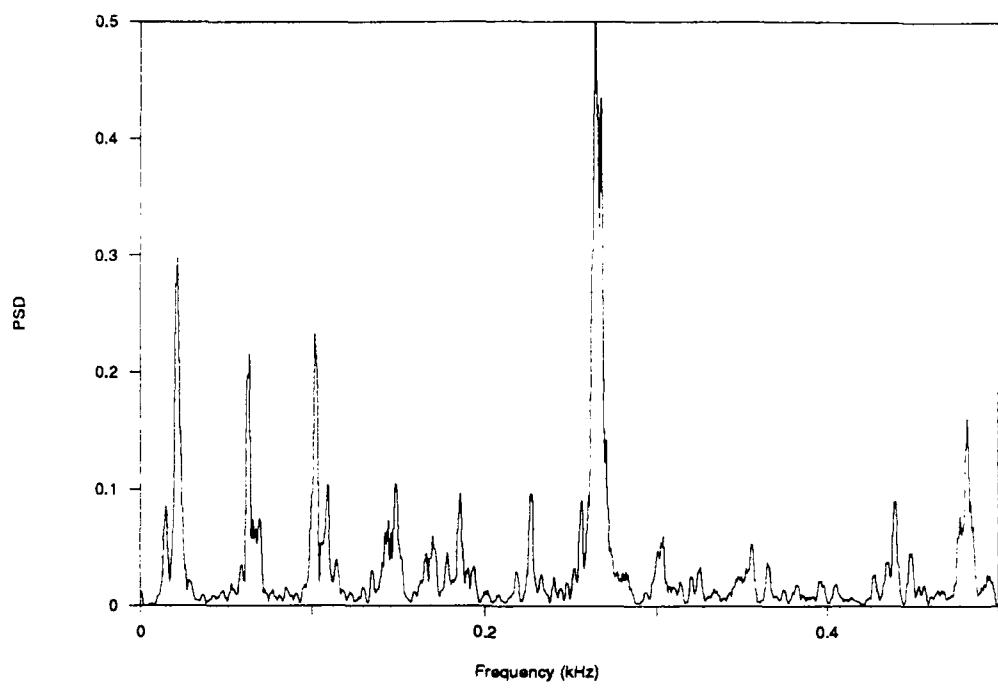
Figure 46.
X=5mm, Z=2.8mm, 10 ft/sec
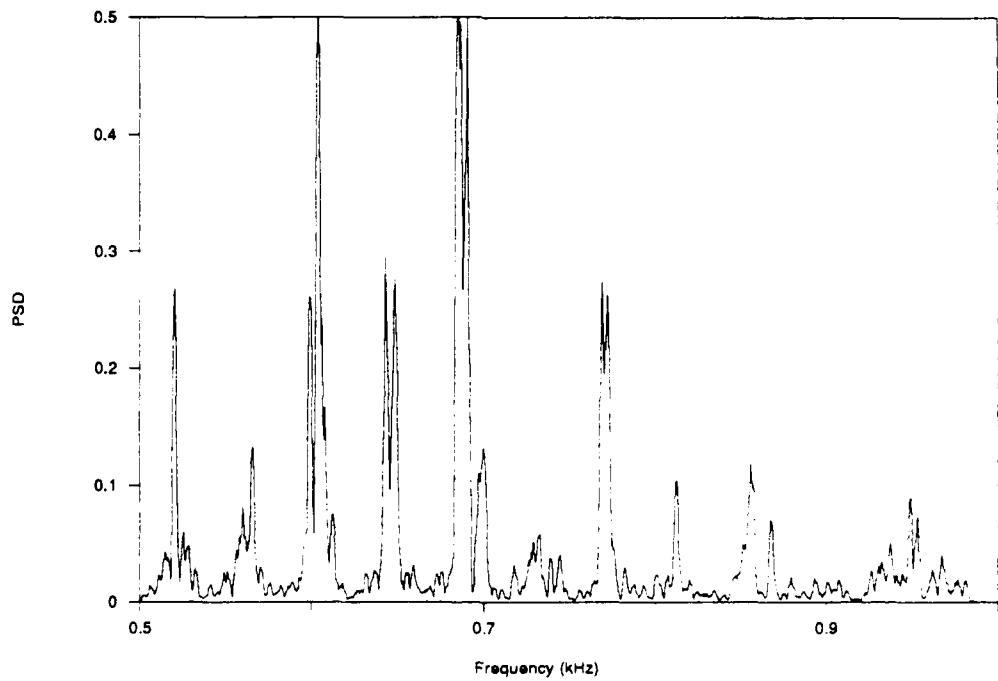
Figure 47.
X=5mm, Z=2.8mm, 10 ft/sec

Page 64
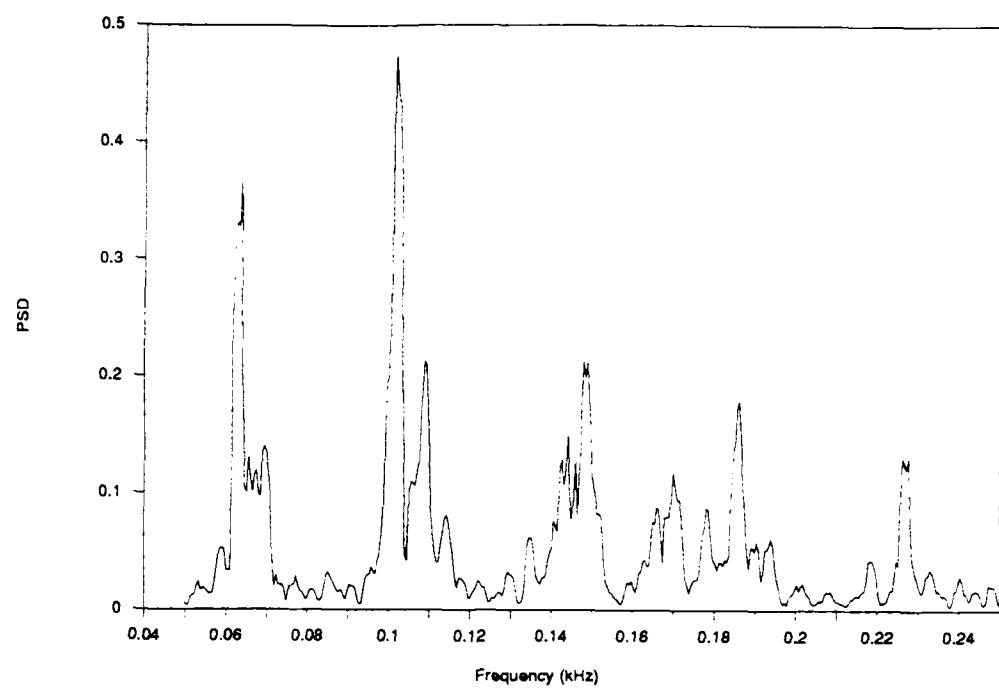
Figure 48.
X=5mm, Z=2.8mm, 10 ft/sec
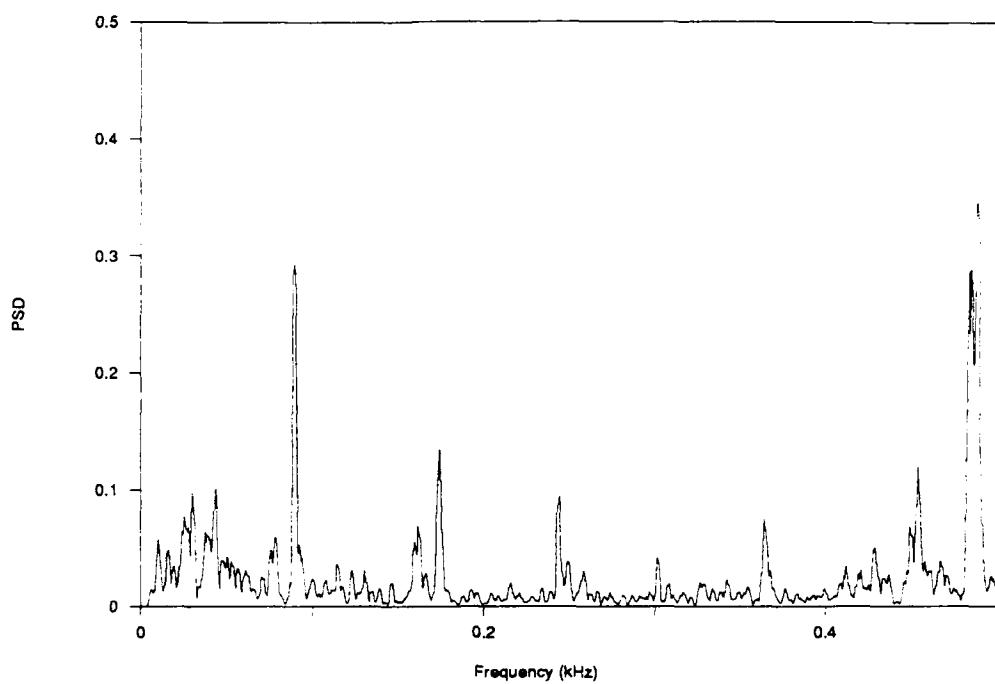
Figure 49.
X=15mm, Z=2.8mm, 10 ft/sec
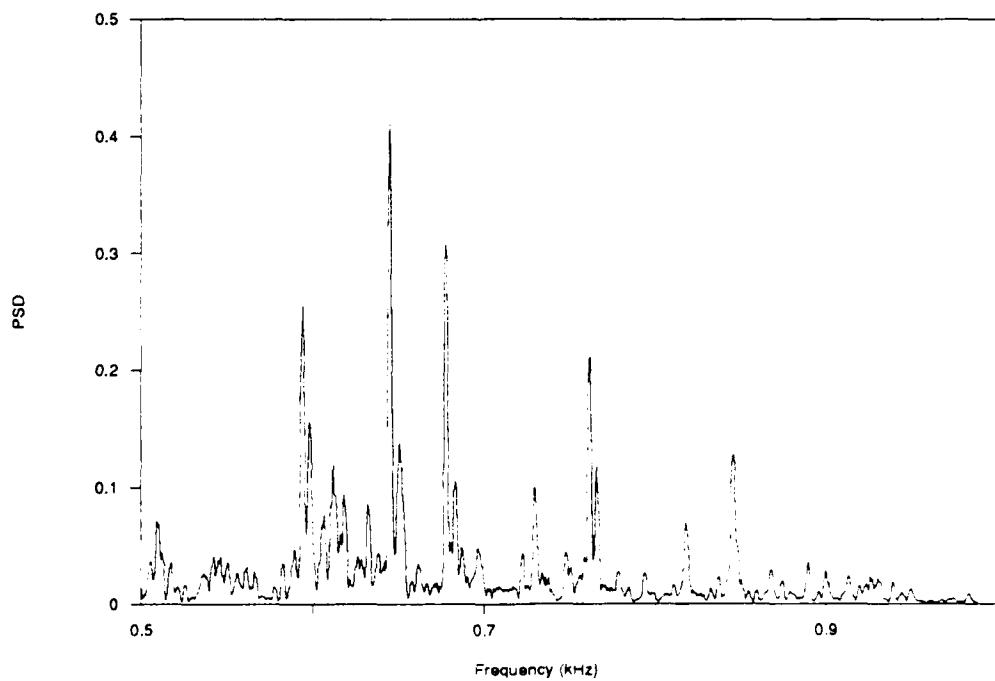
Figure 50.
X=15mm, Z=2.8mm, 10 ft/sec

Page 66
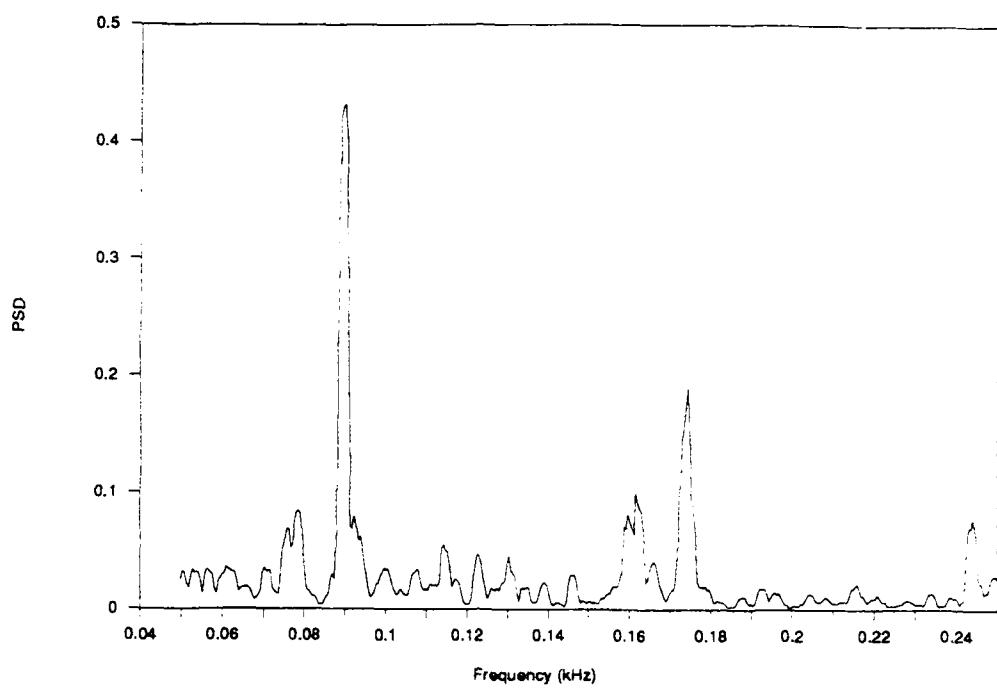
Figure 51.
X=15mm, Z=2.8mm, 10 ft/sec
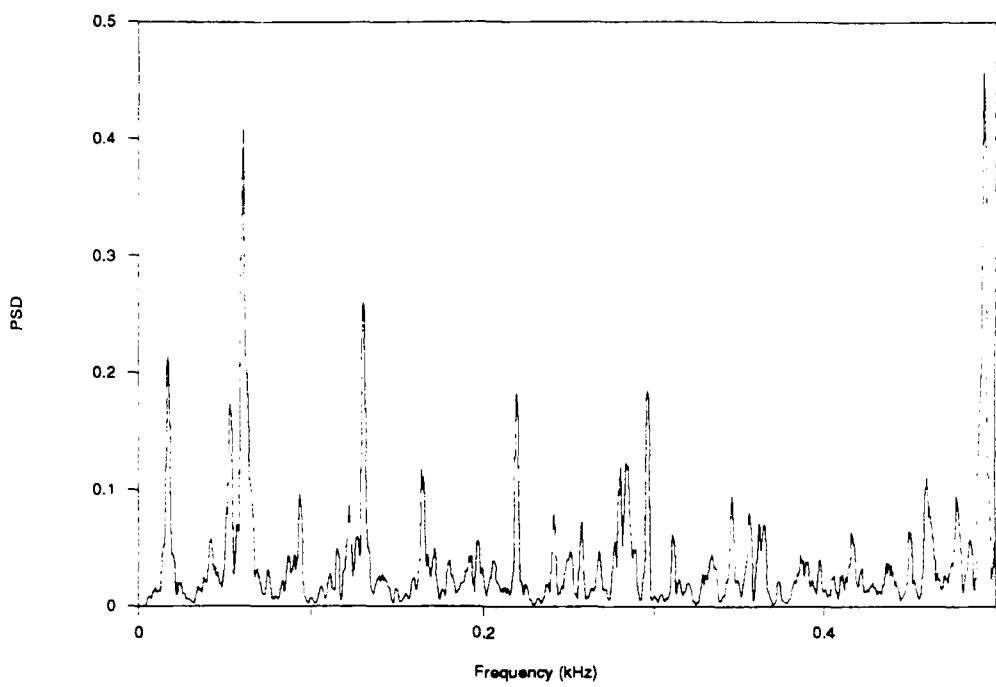
Figure 52.
X=25mm, Z=2.8mm, 10 ft/sec
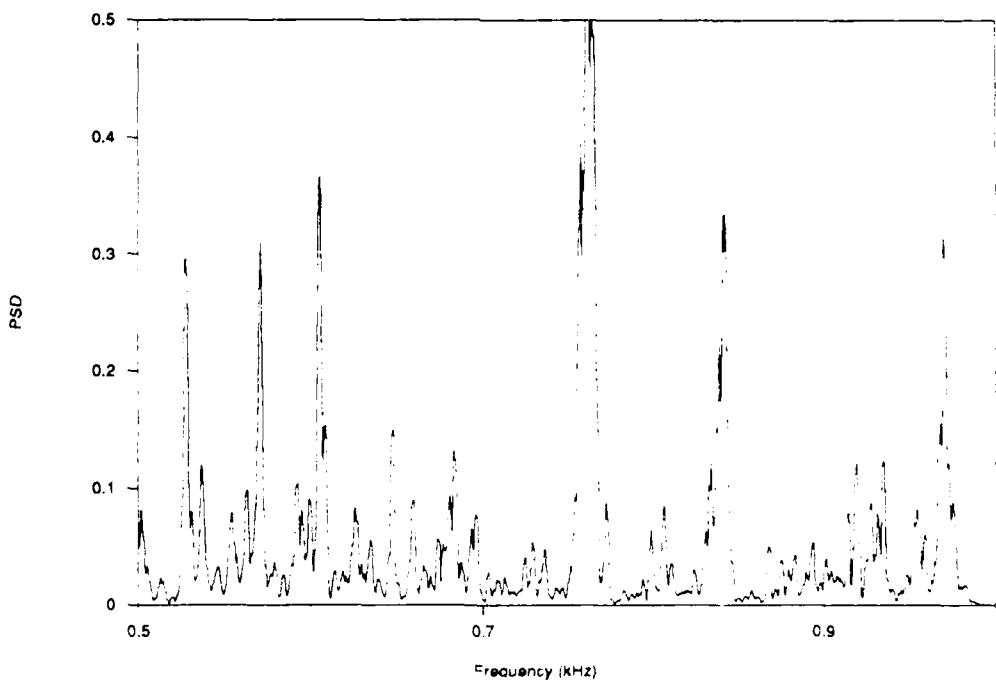
Figure 53.
X=25mm, Z=2.8mm, 10 ft/sec

Page 68
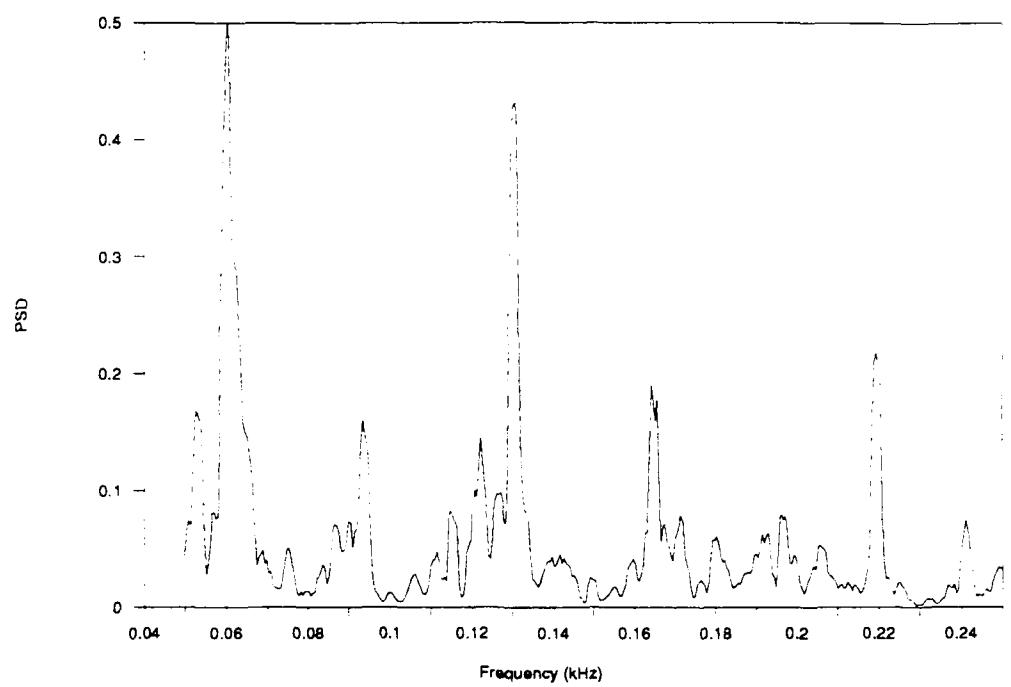
Figure 54.
X=25mm, Z=2.8mm, 10 ft/sec
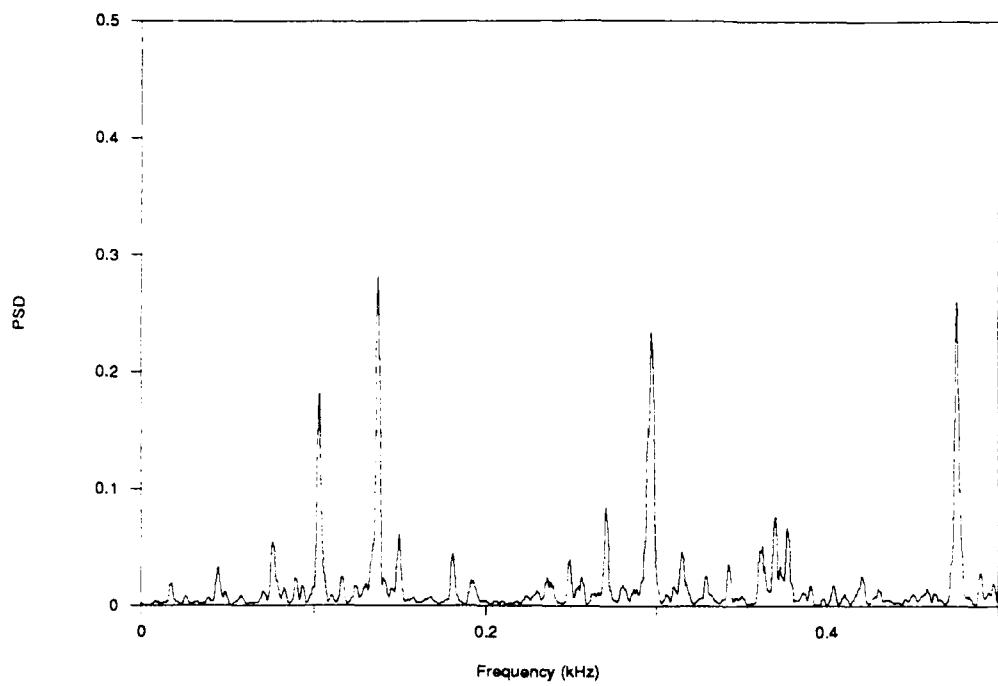
Figure 55.
Boundary Layer, 10 ft/sec
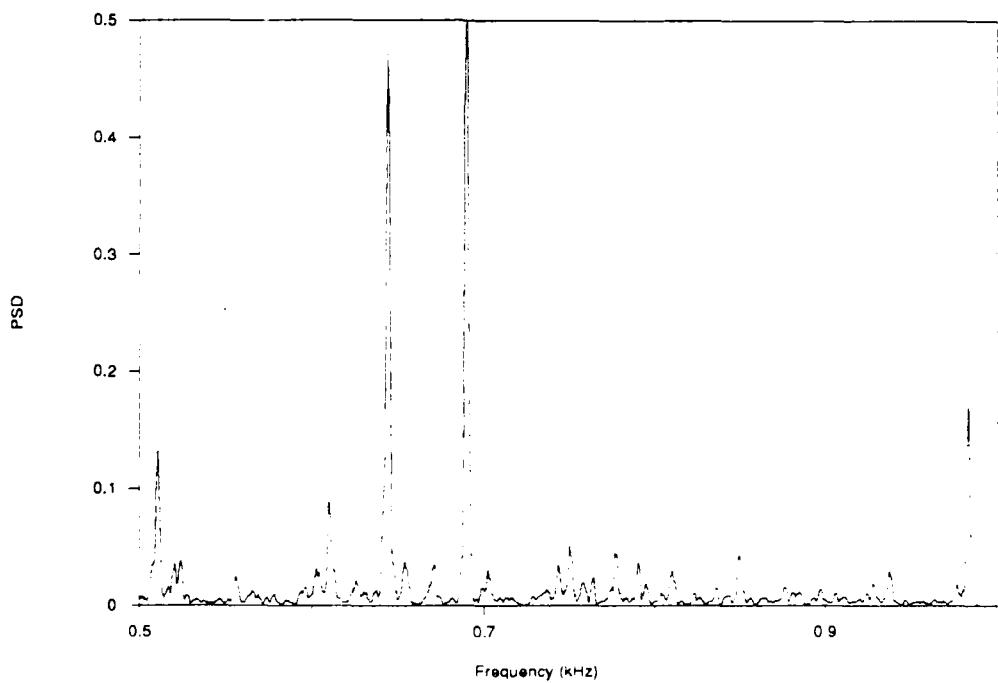
Figure 56.
Boundary Layer, 10 ft/sec

Page 70
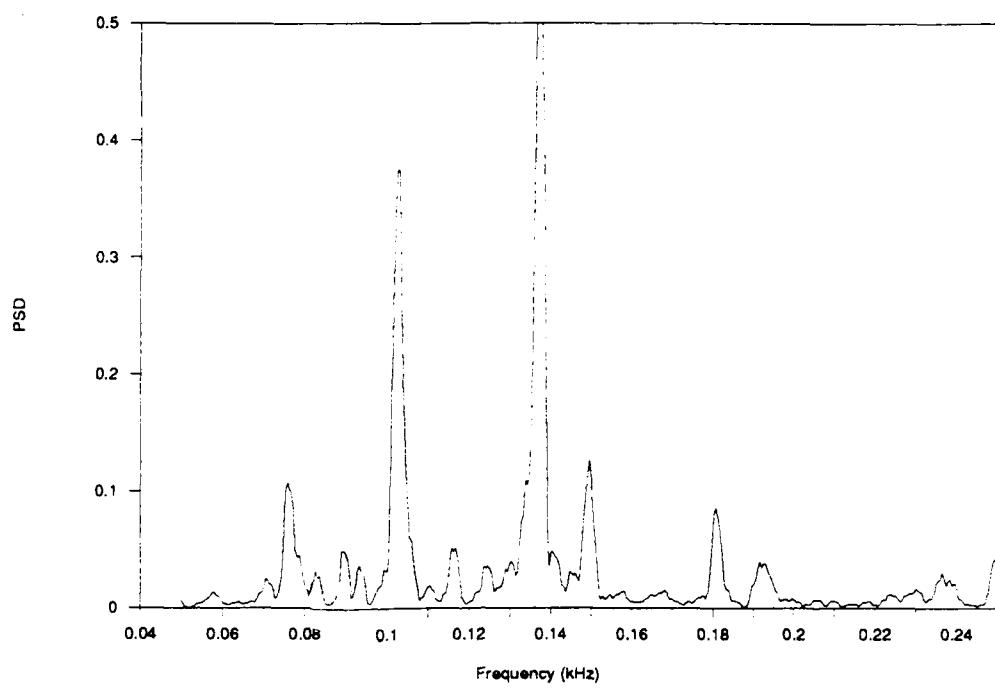
Figure 57.
Boundary Layer, 10 ft/sec
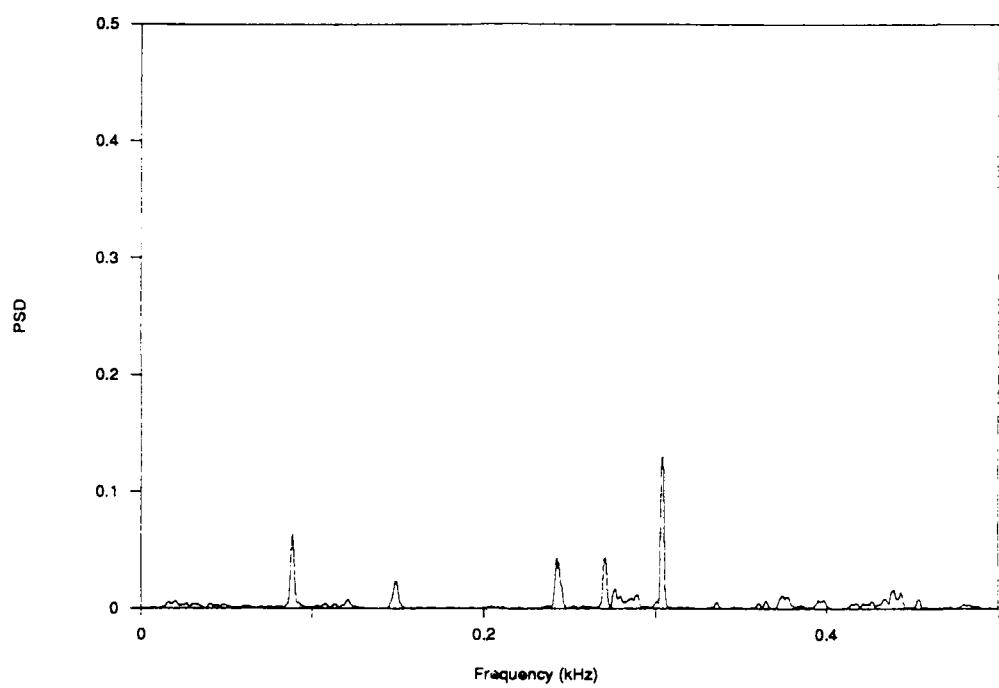
Figure 58.
X=5mm, Z=1mm, 20 ft/sec
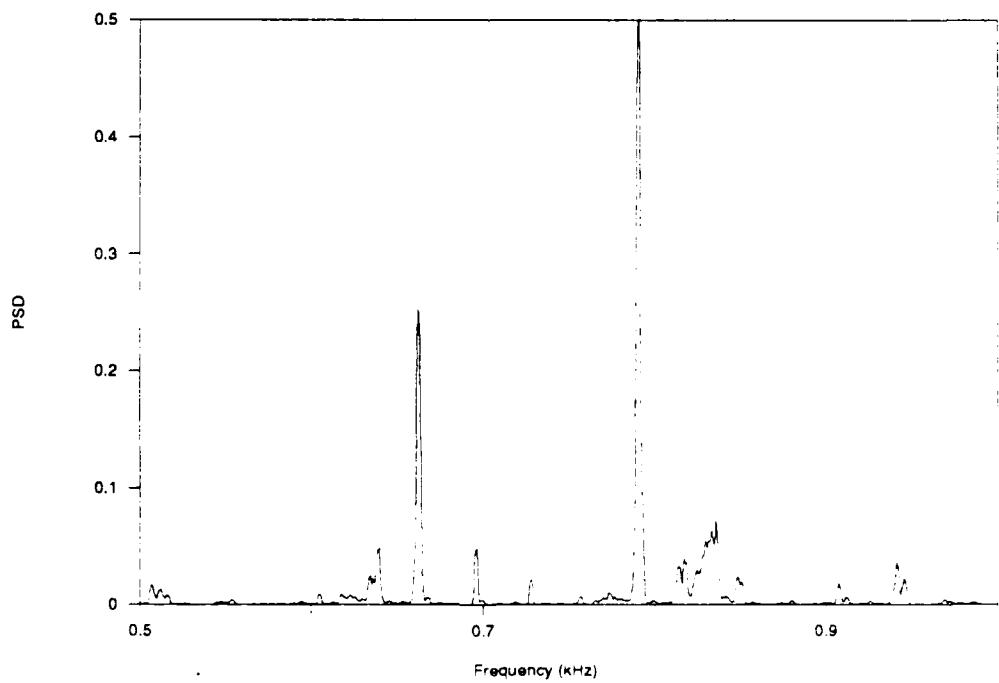
Figure 59.
X=5mm, Z=1mm, 20 ft/sec
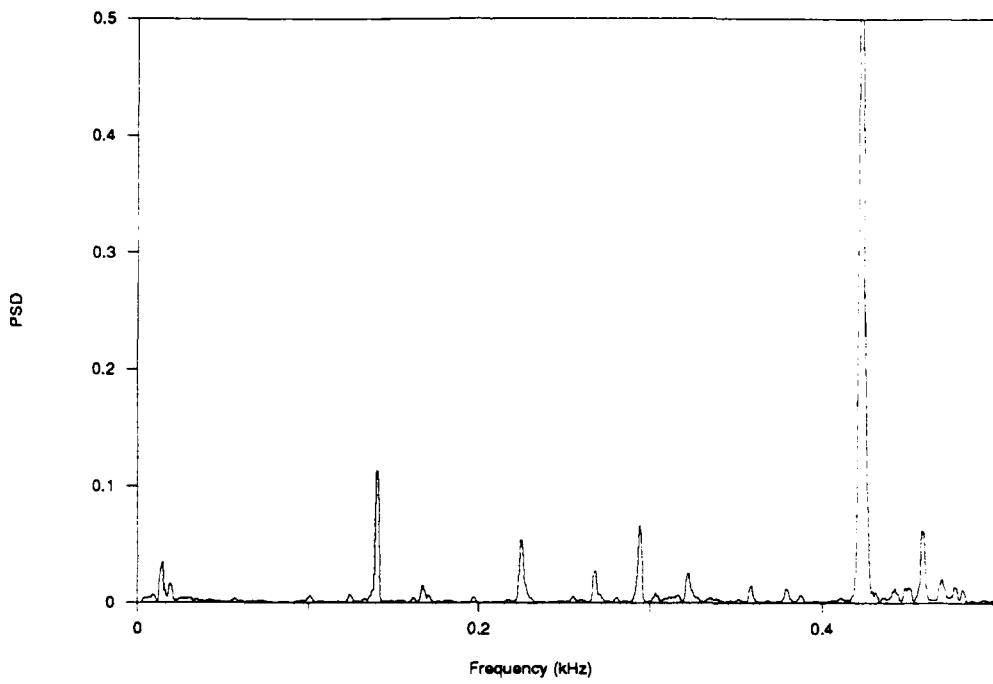
Figure 60.
X=10mm, Z=1mm, 20 ft/sec
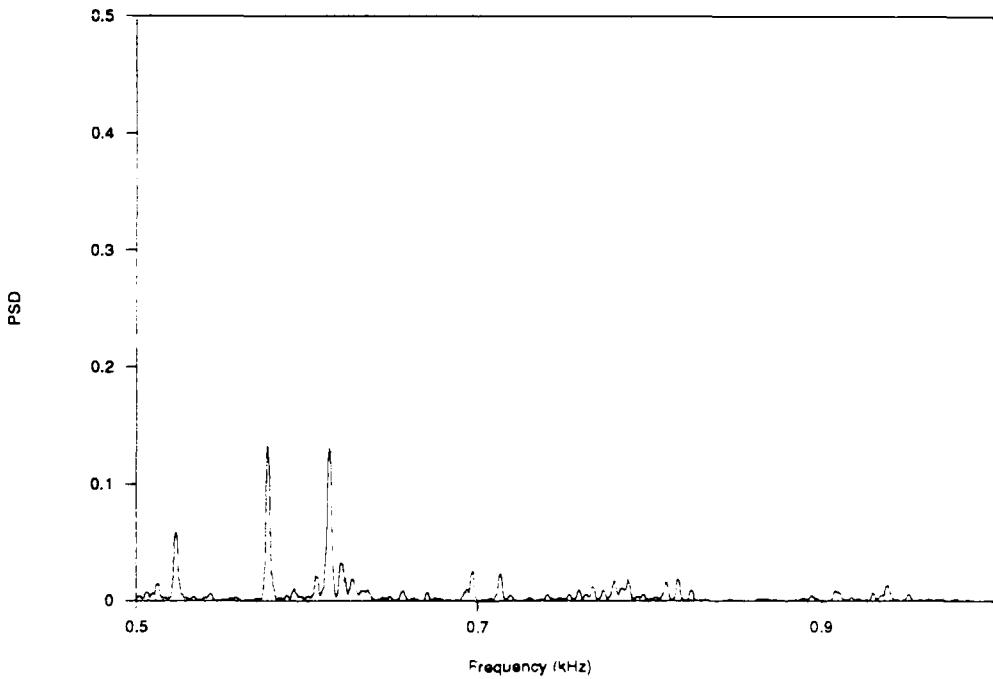
Figure 61.
X=10mm, Z=1mm, 20 ft/sec
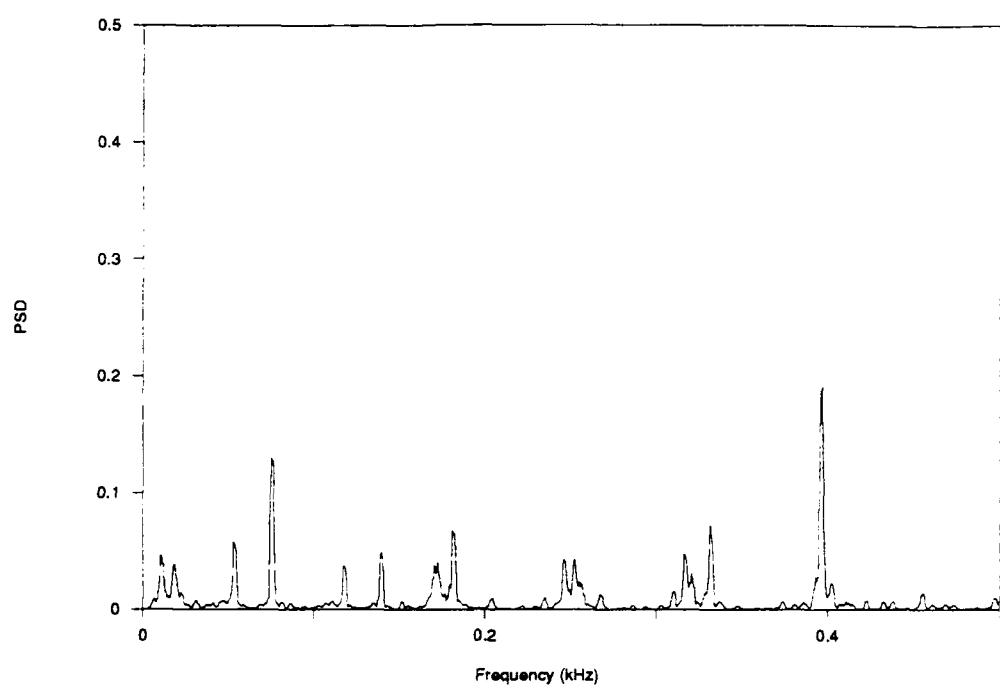
Figure 62.
X=15mm, Z=1mm, 20 ft/sec
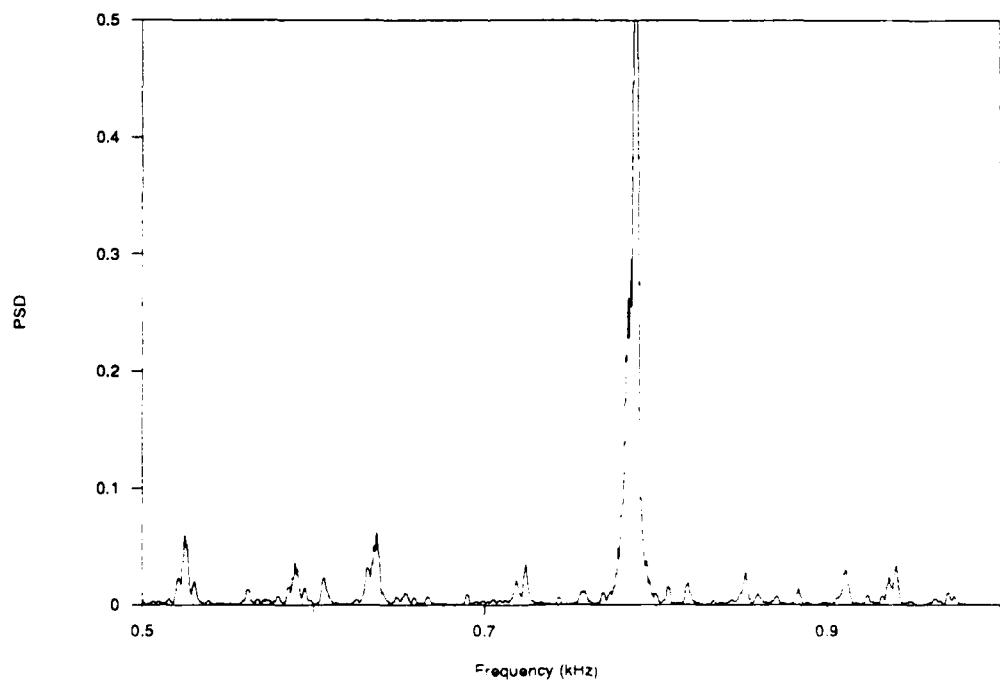
Figure 63.
X=15mm, Z=1mm, 20 ft/sec
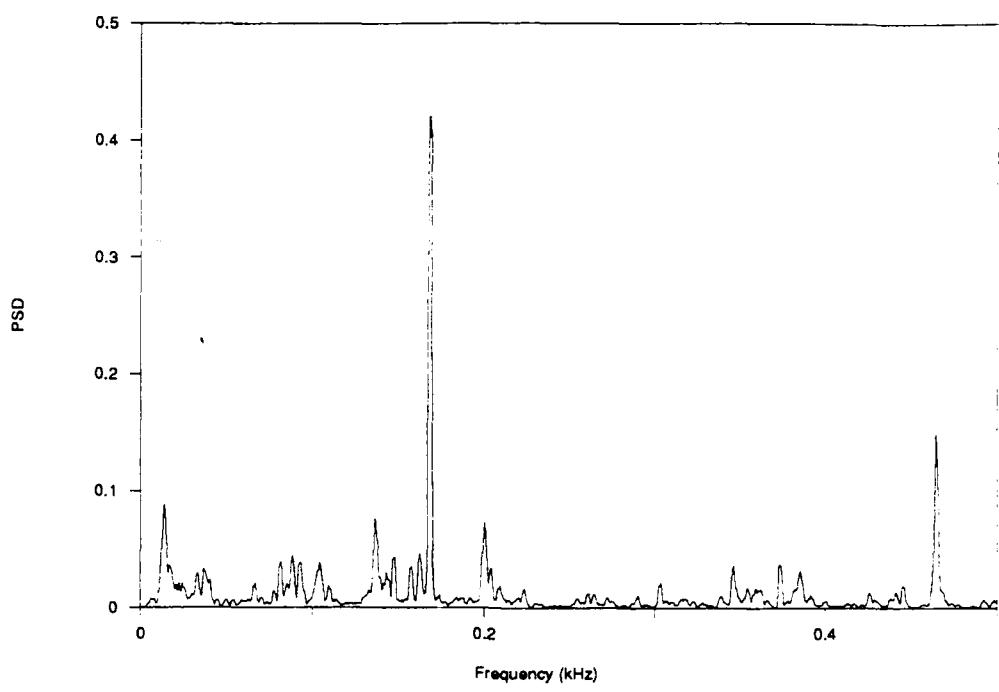
Figure 64.
X=25mm, Z=1mm, 20 ft/sec
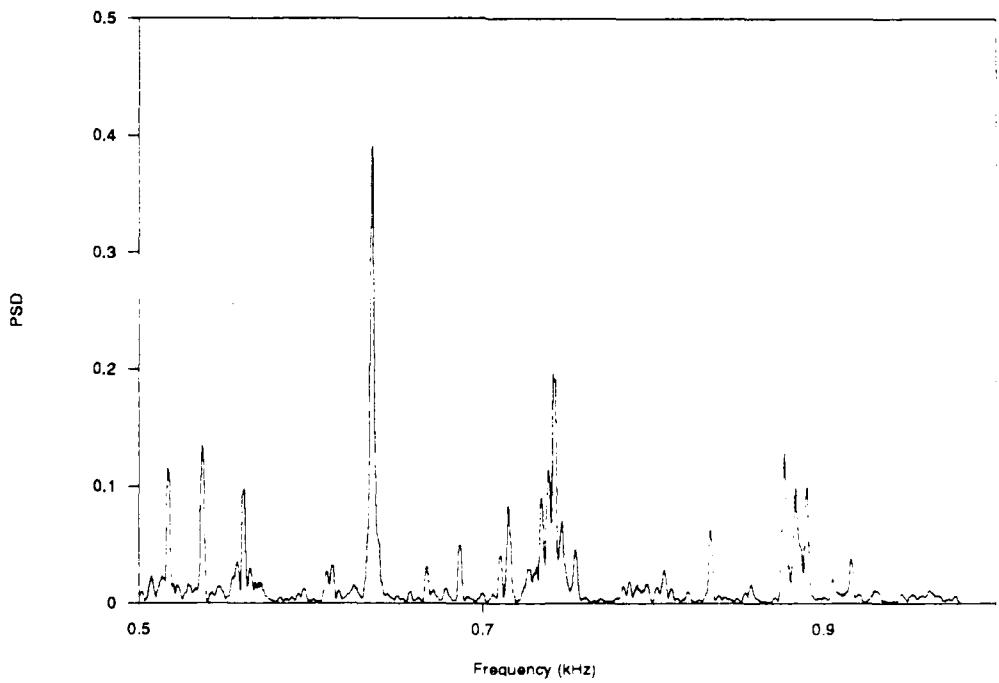
Figure 65.
X=25mm, Z=1mm, 20 ft/sec

Page 75
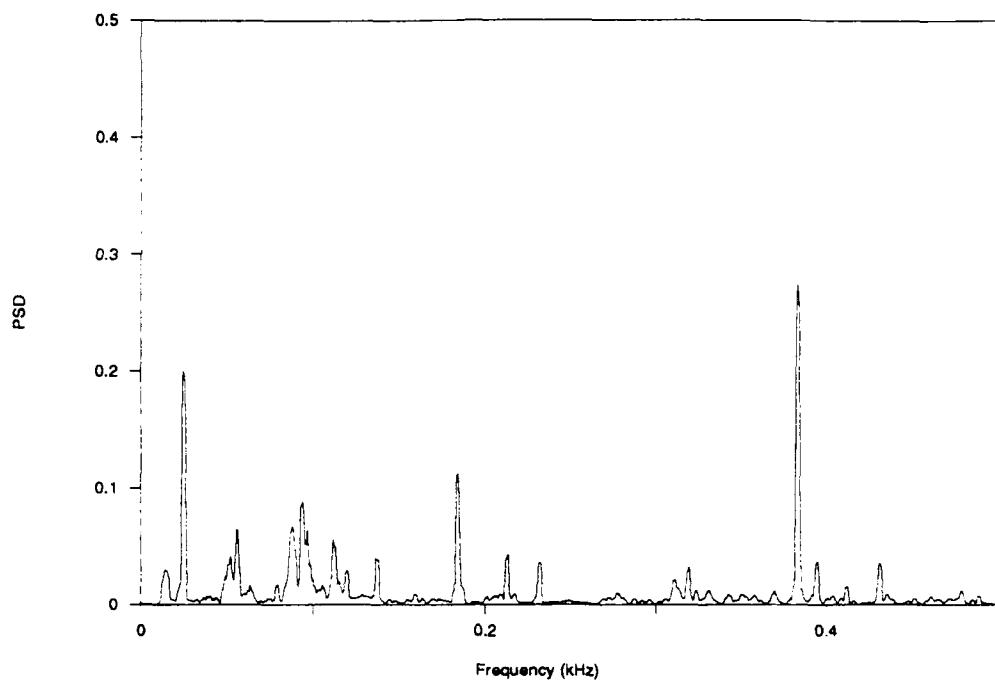
Figure 66.
X=5mm, Z=7mm, 20 ft/sec
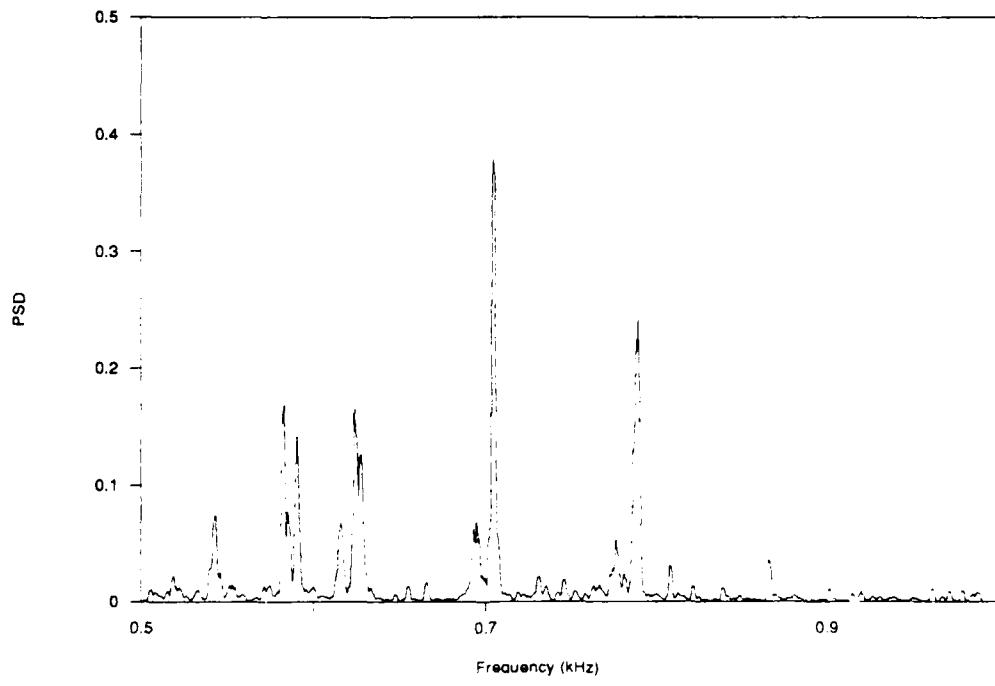
Figure 67.
X=5mm, Z=7mm, 20 ft/sec
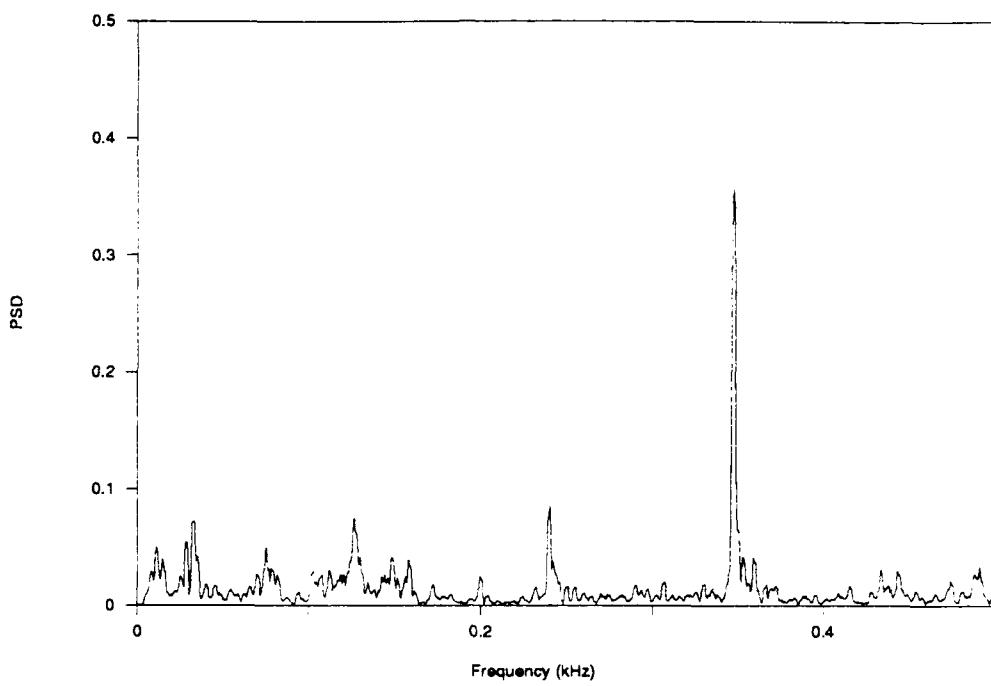
Figure 68.
X=15mm, Z=7mm, 20 ft/sec
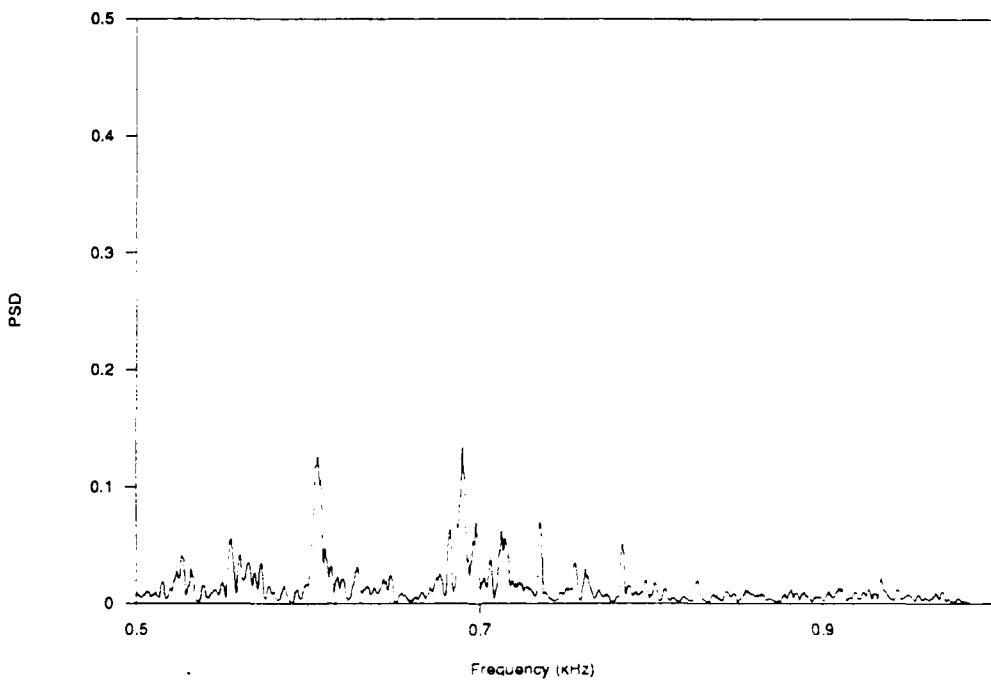
Figure 69.
X=15mm, Z=7mm, 20 ft/sec

Page 77
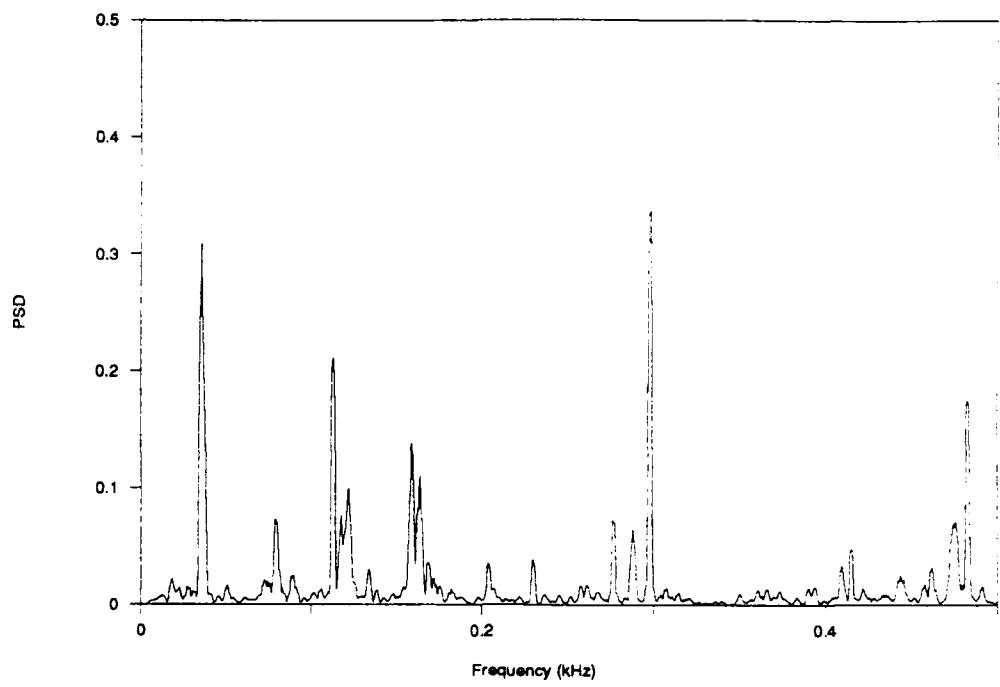
Figure 70.
X=25mm, Z=7mm, 20 ft/sec
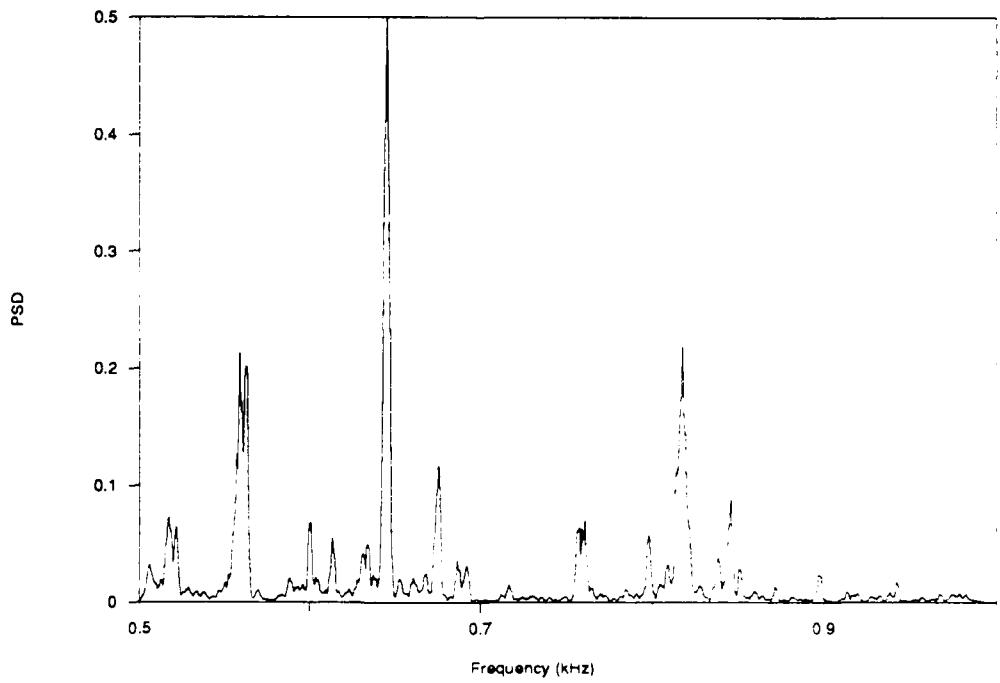
Figure 71.
X=25mm, Z=7mm, 20 ft/sec
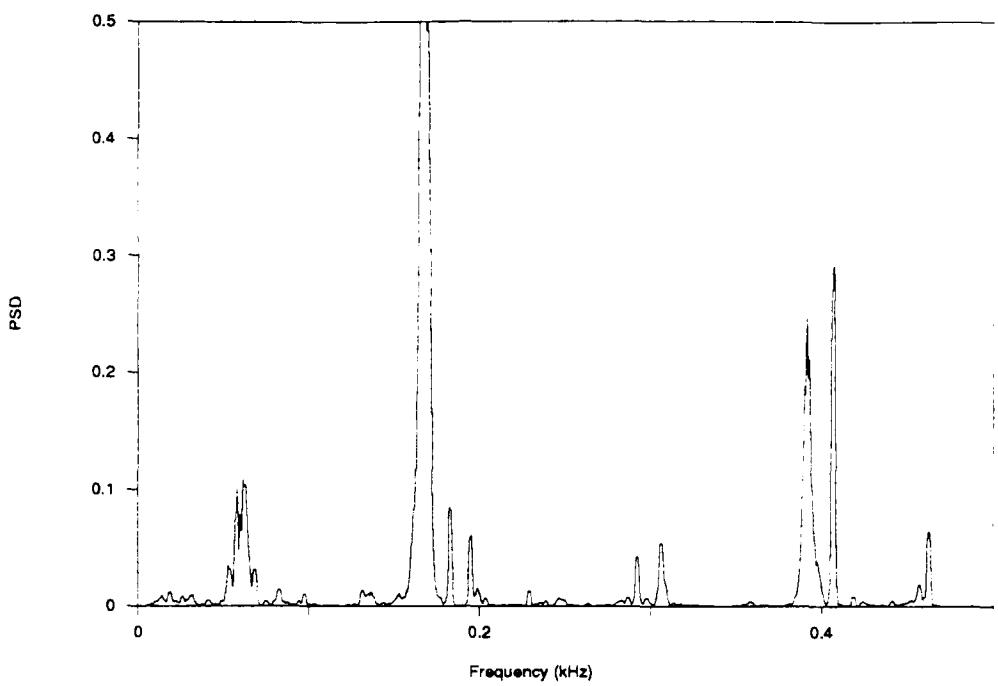
Figure 72.
X=5mm, Z=2.1mm, 20 ft/sec
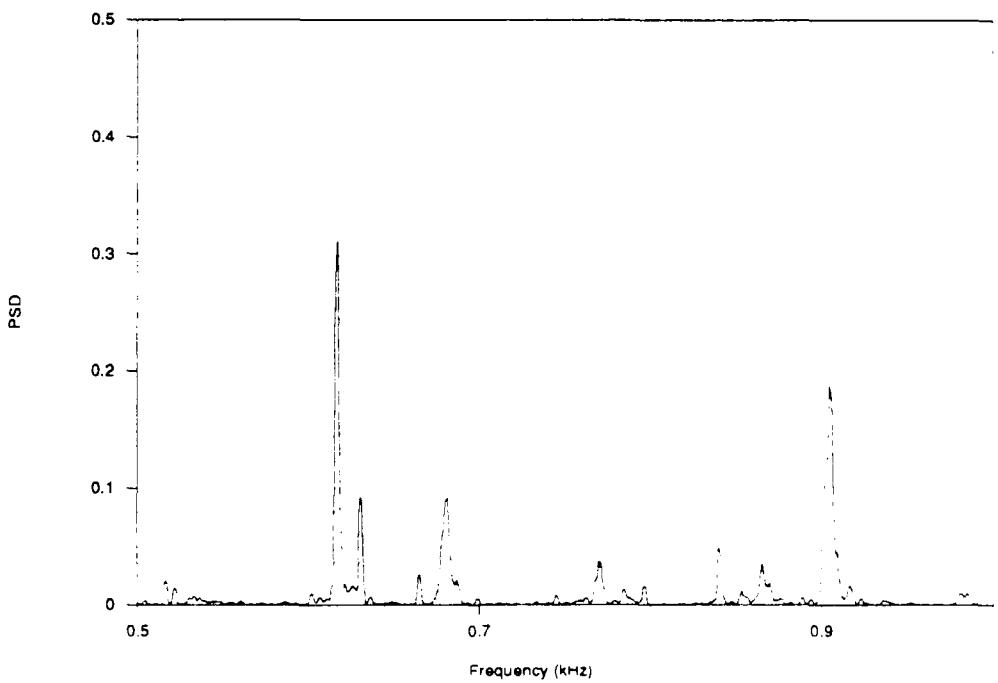
Figure 73.
X=5mm, Z=2.1mm, 20 ft/sec
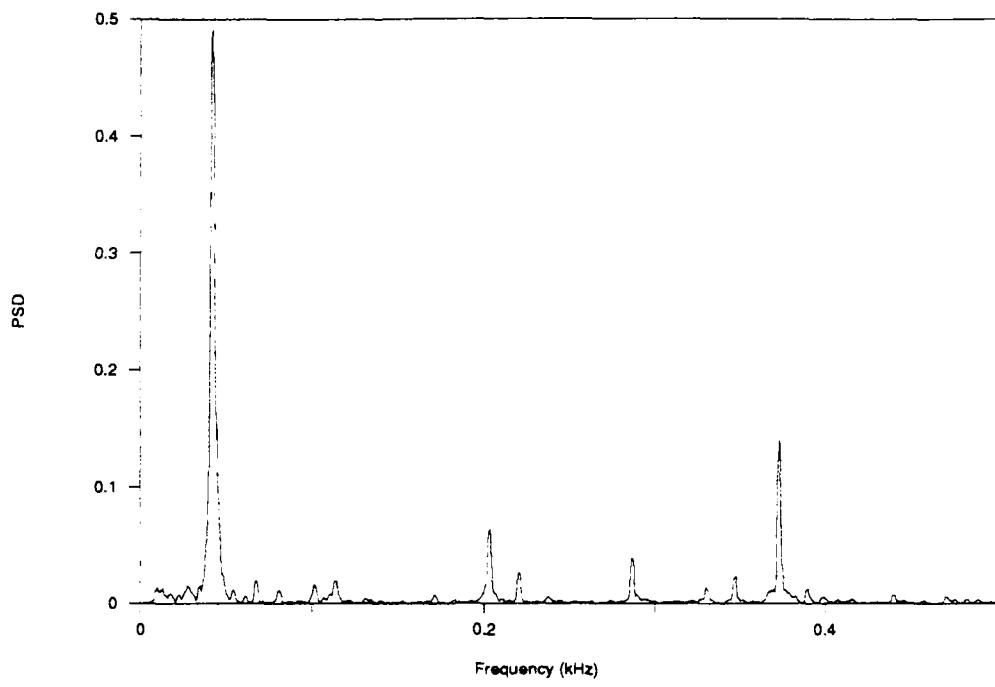
Figure 74.
X=15mm, Z=2.1mm, 20 ft/sec
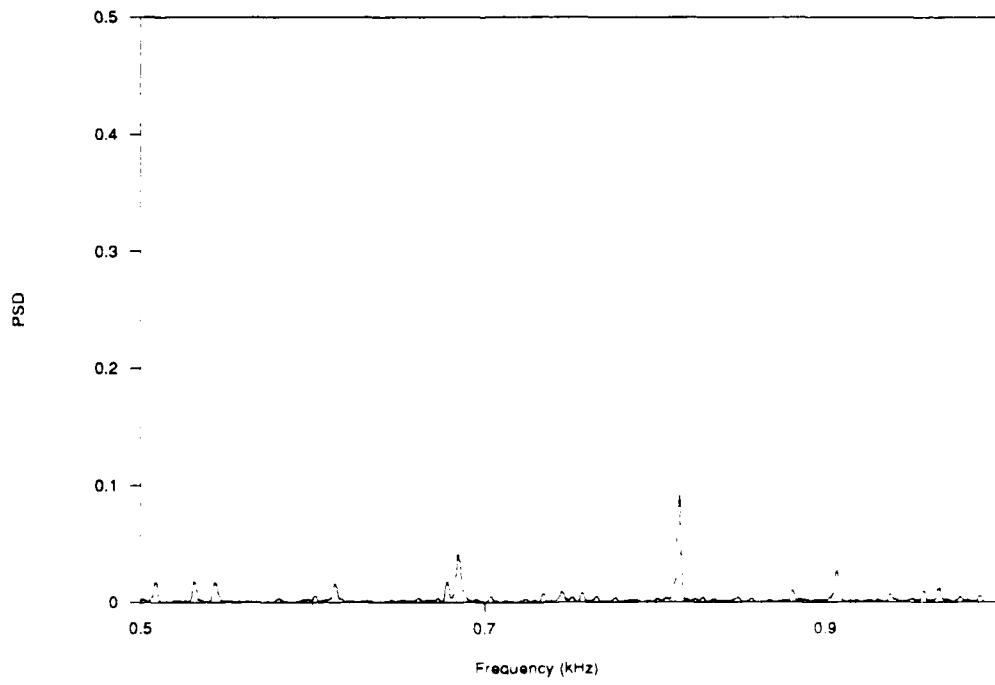
Figure 75.
X=15mm, Z=2.1mm, 20 ft/sec
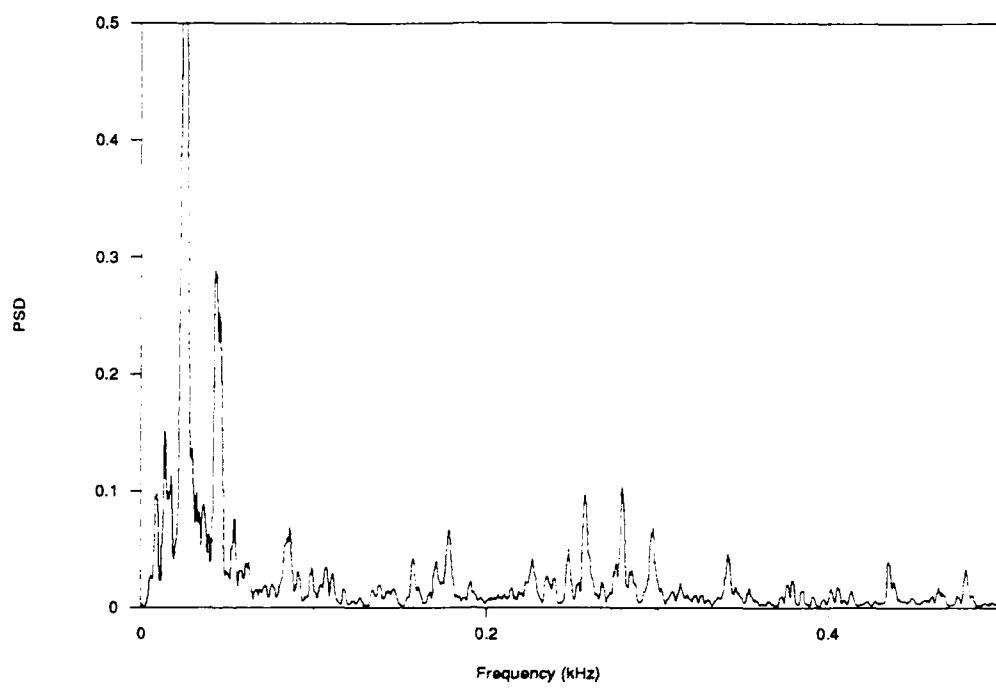
Figure 76.
X=25mm, Z=2.1mm, 20 ft/sec
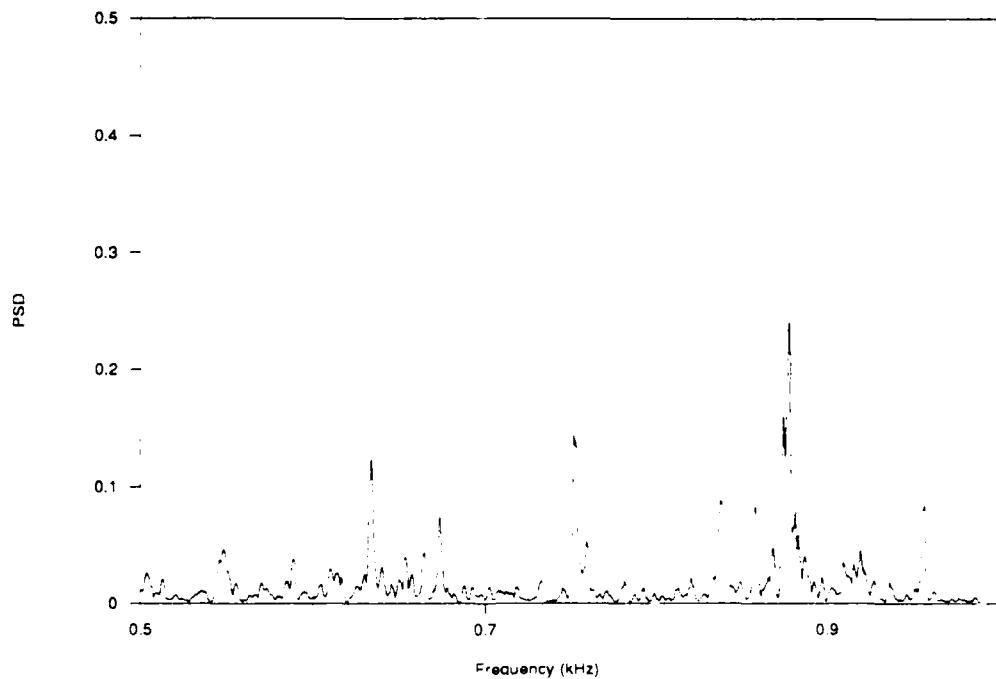
Figure 77.
X=25mm, Z=2.1mm, 20 ft/sec

Page 81
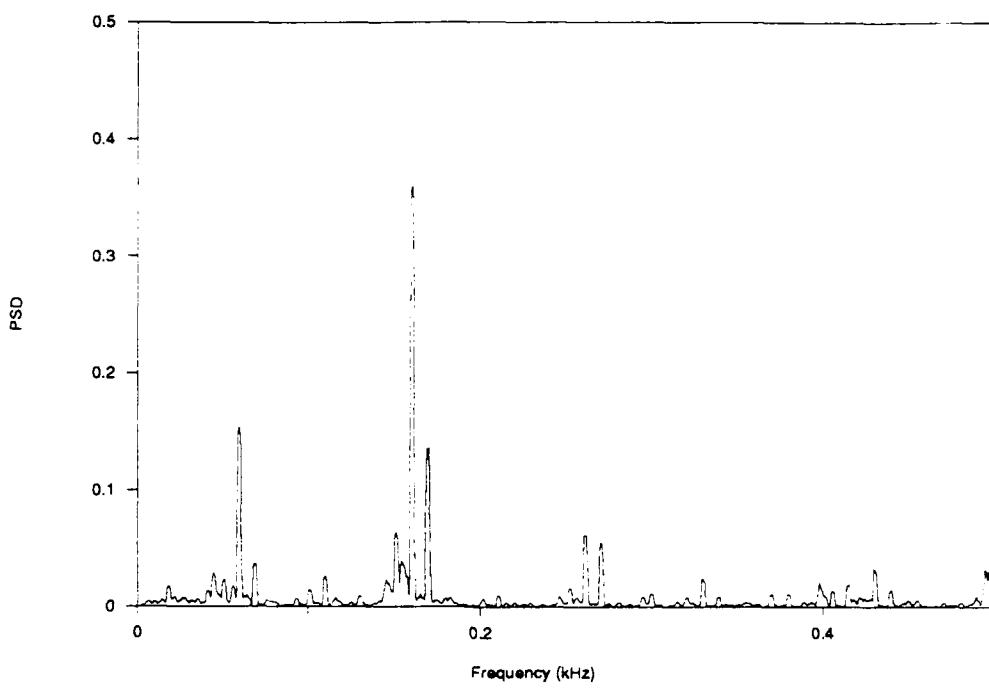
Figure 78.
Boundary Layer, 20 ft/sec
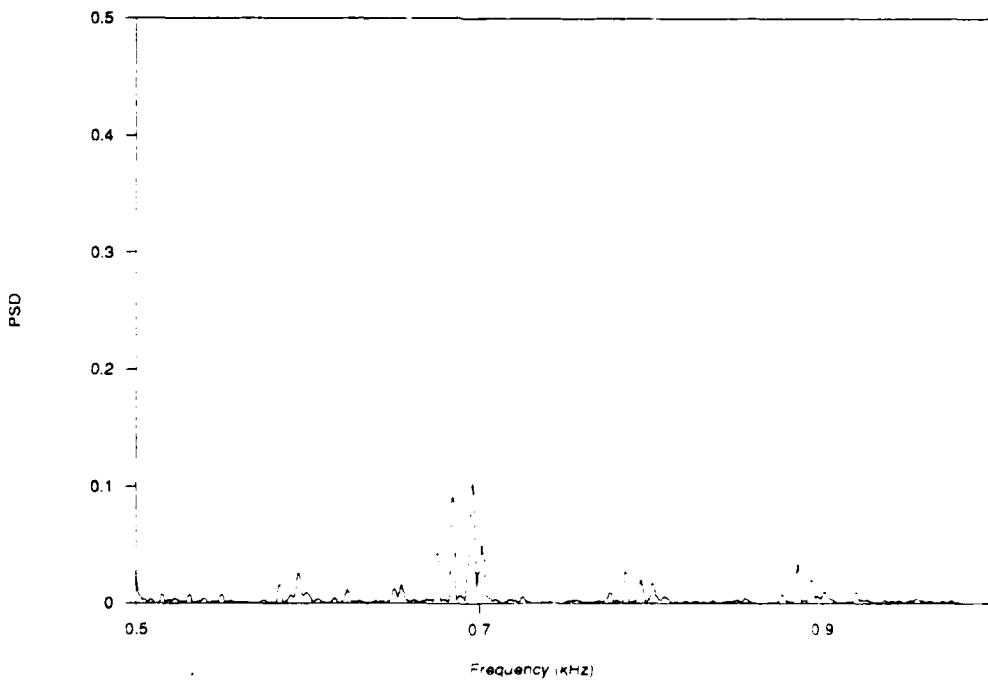
Figure 79.
Boundary Layer, 20 ft/sec

APPENDIX C.

VELOCITY PROBABILITY DISTRIBUTIONS
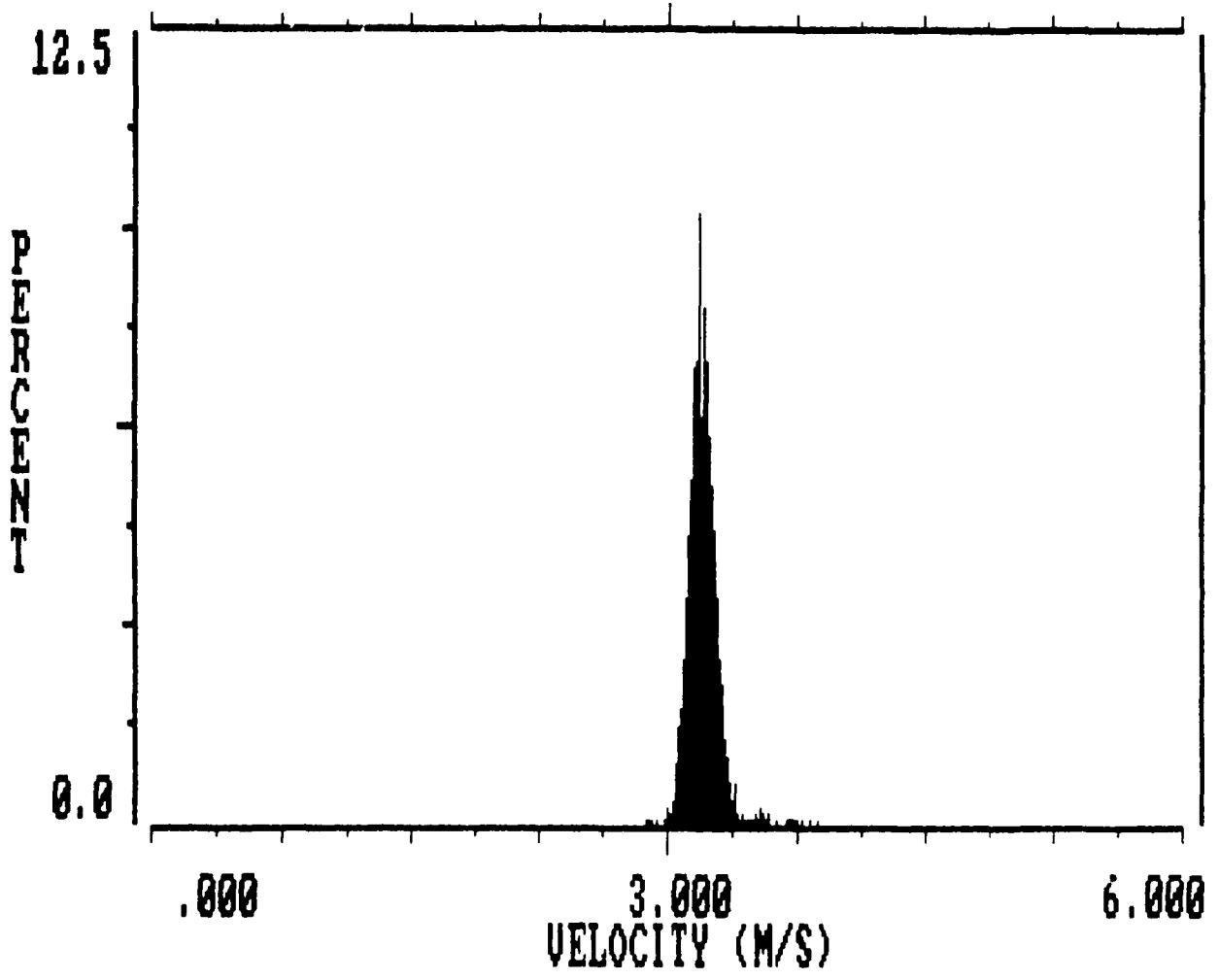
Figure 80.
Free Stream, 10 ft/sec
The PSD is Gaussian with a small standard deviation.
The non-symmetry is due to input filter settings of the signal processor.
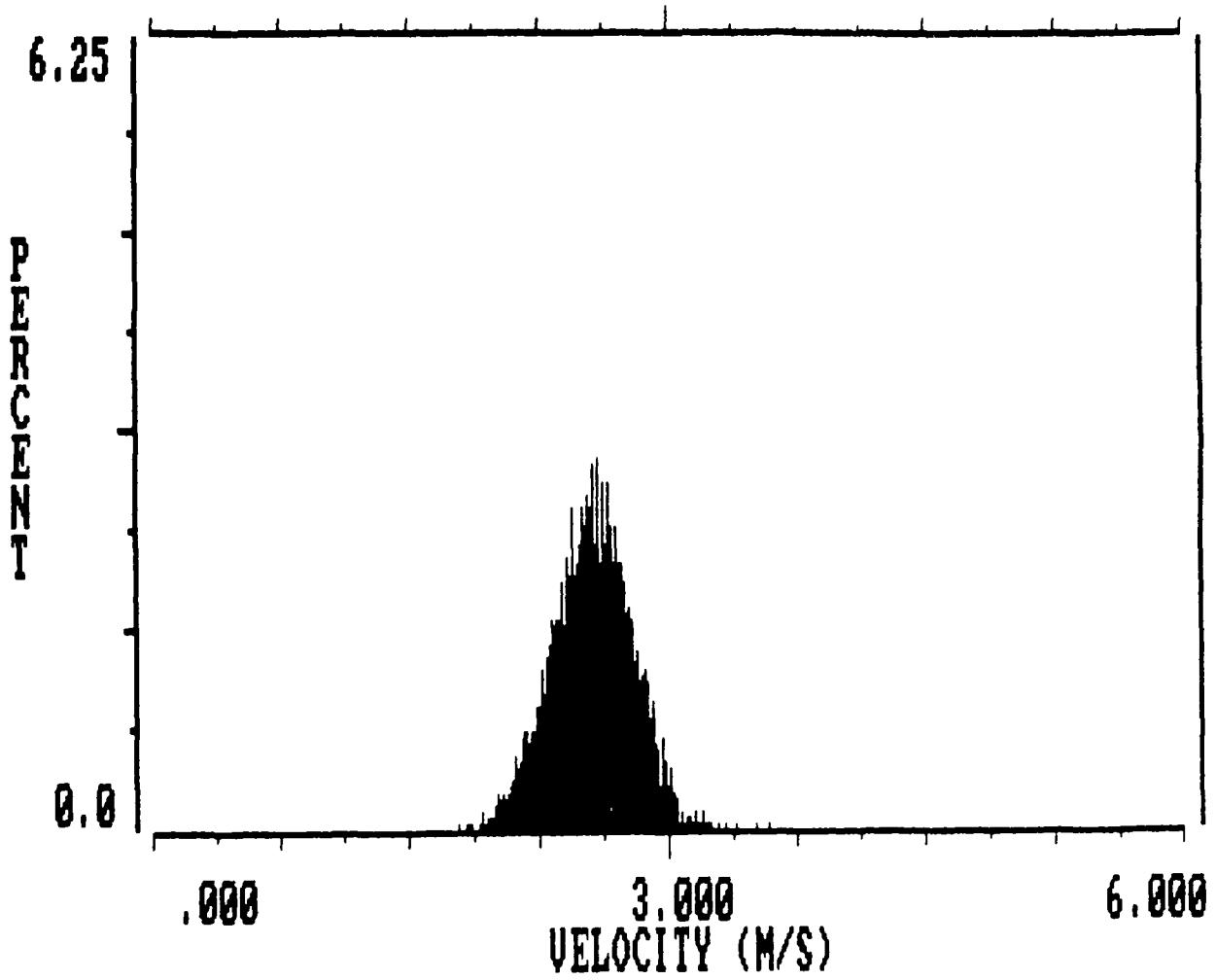
Figure 81.
Boundary Layer, 10 ft/sec
The larger standard deviation is due to turbulence in the boundary layer.
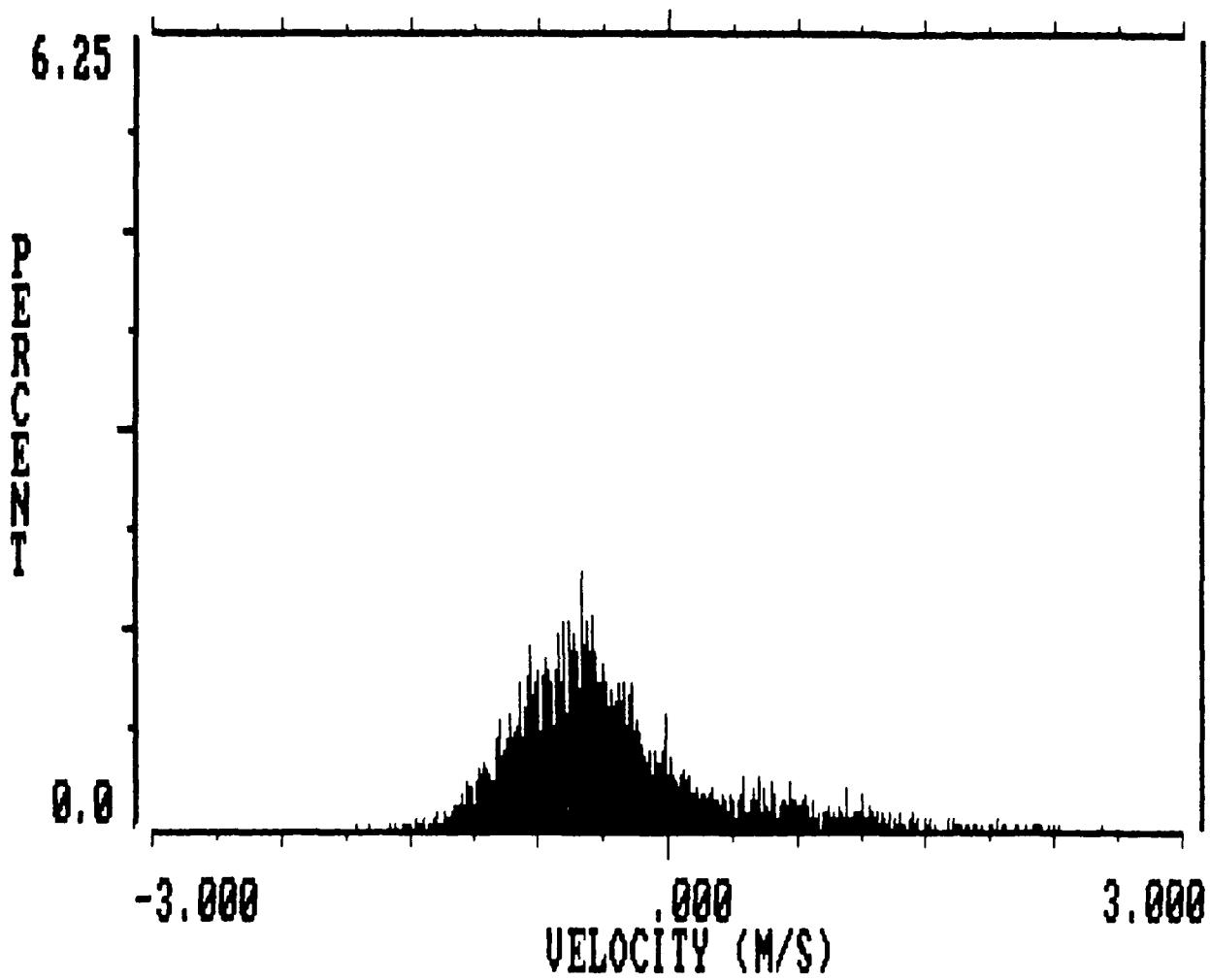
Figure 82.
X=5mm, Z=1mm, 10 ft/sec
A negative velocity is dominant near the foil as expected.
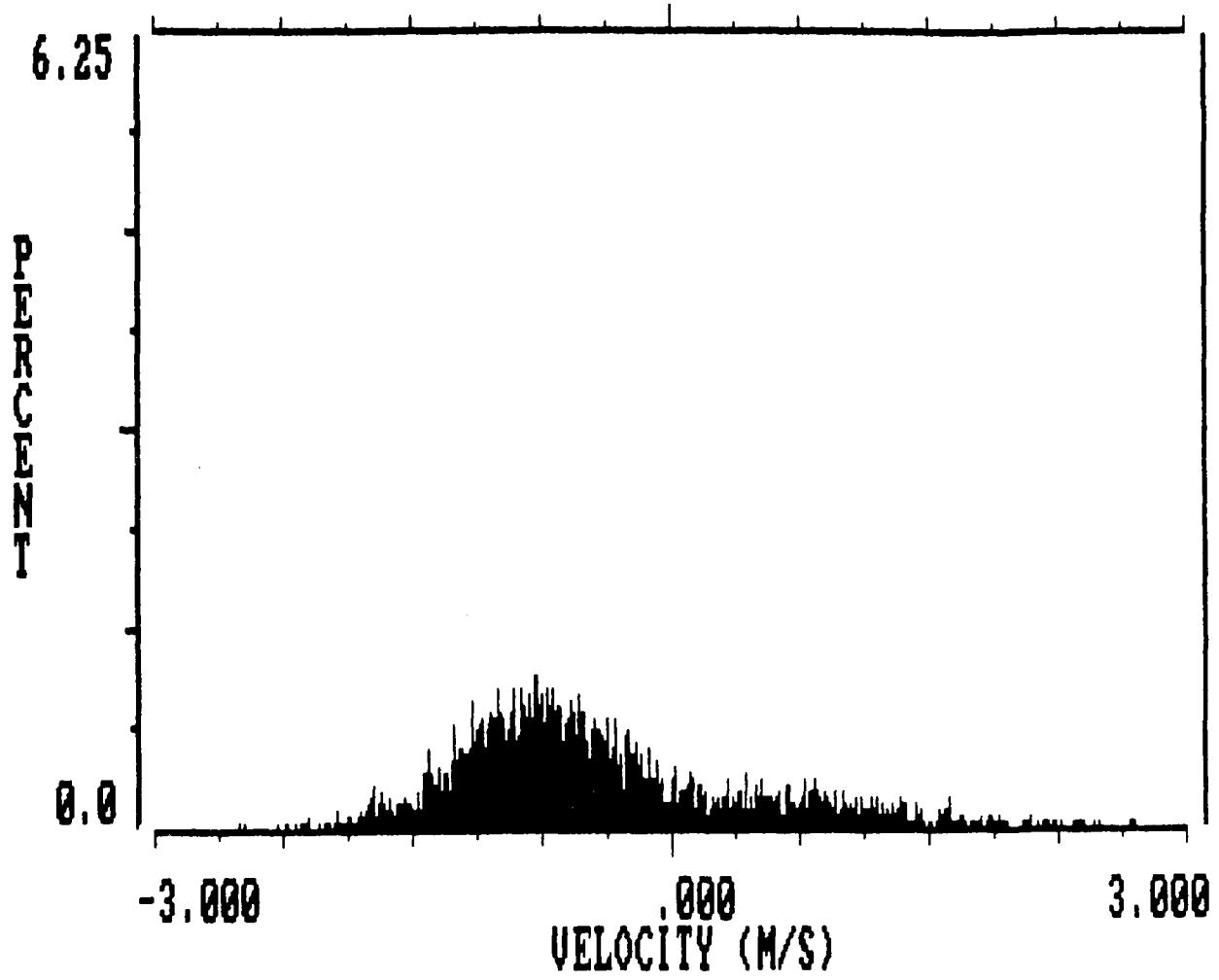
Figure 83.
X=10mm, Z=1mm, 10 ft/sec
The double peak or bimodal structure starts to become evident.
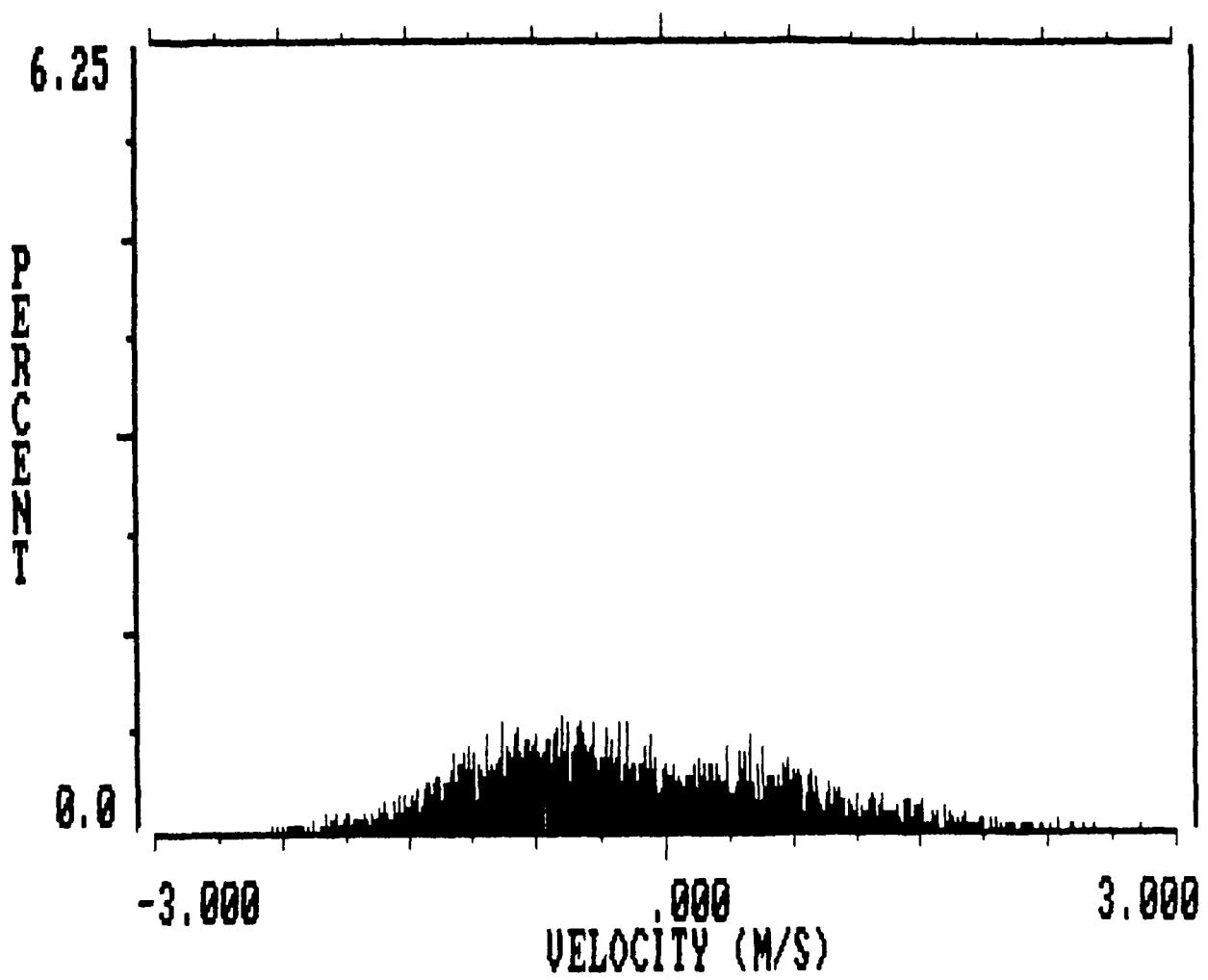
Figure 84.
X=12.5mm, Z=1mm, 10 ft/sec
The double peak is evident.
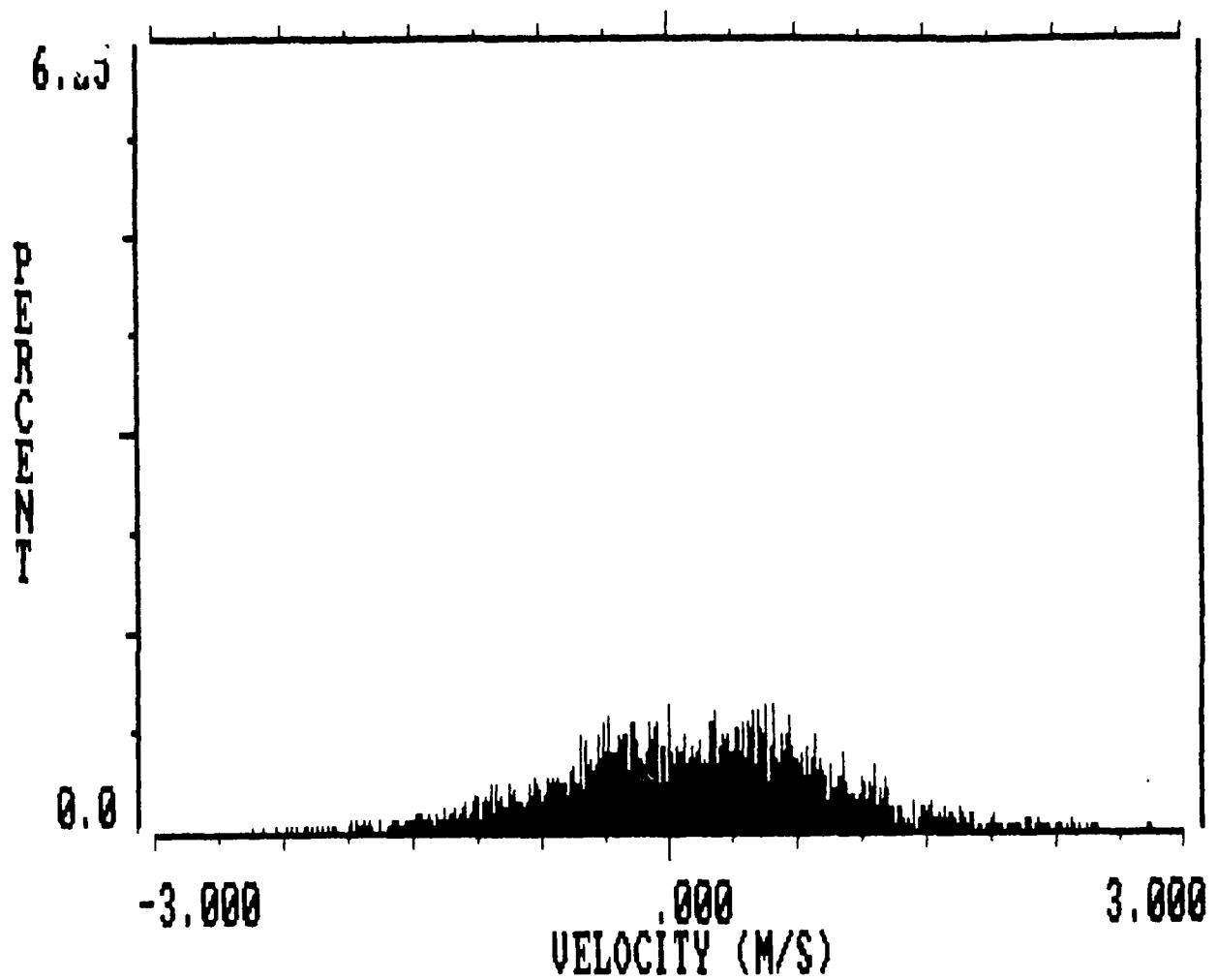
Figure 85.
X=15mm, Z=1mm, 10 ft/sec
The dominant velocity shifts to positive flow.
Bimodal structure is still evident.
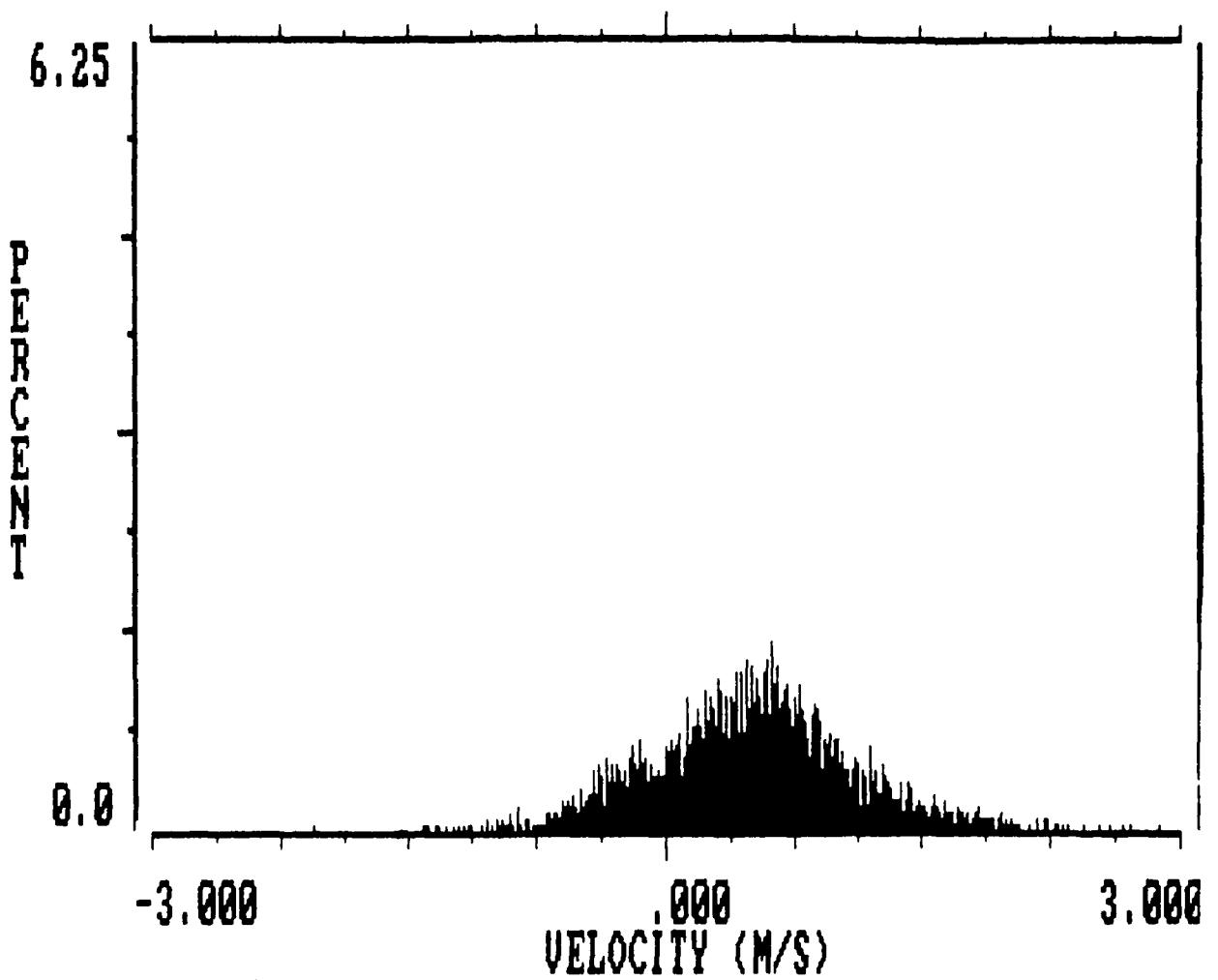
Figure 86.
X=20mm, Z=1mm, 10 ft/sec
The dominant velocity is now strongly positive.
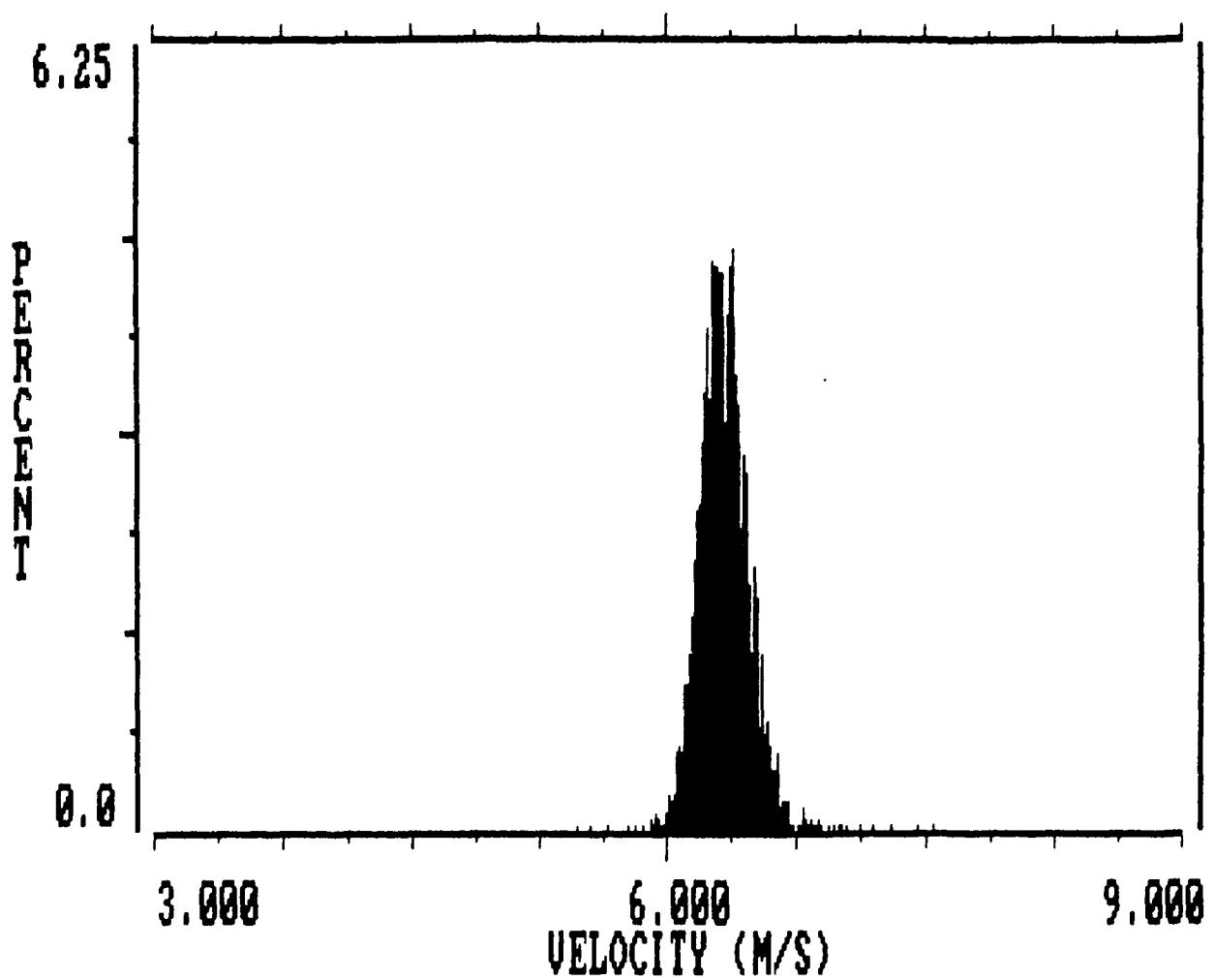
Figure 87.
**Free Stream, 20 ft/sec**
The PSD is Gaussian, similar to 10 ft/sec.
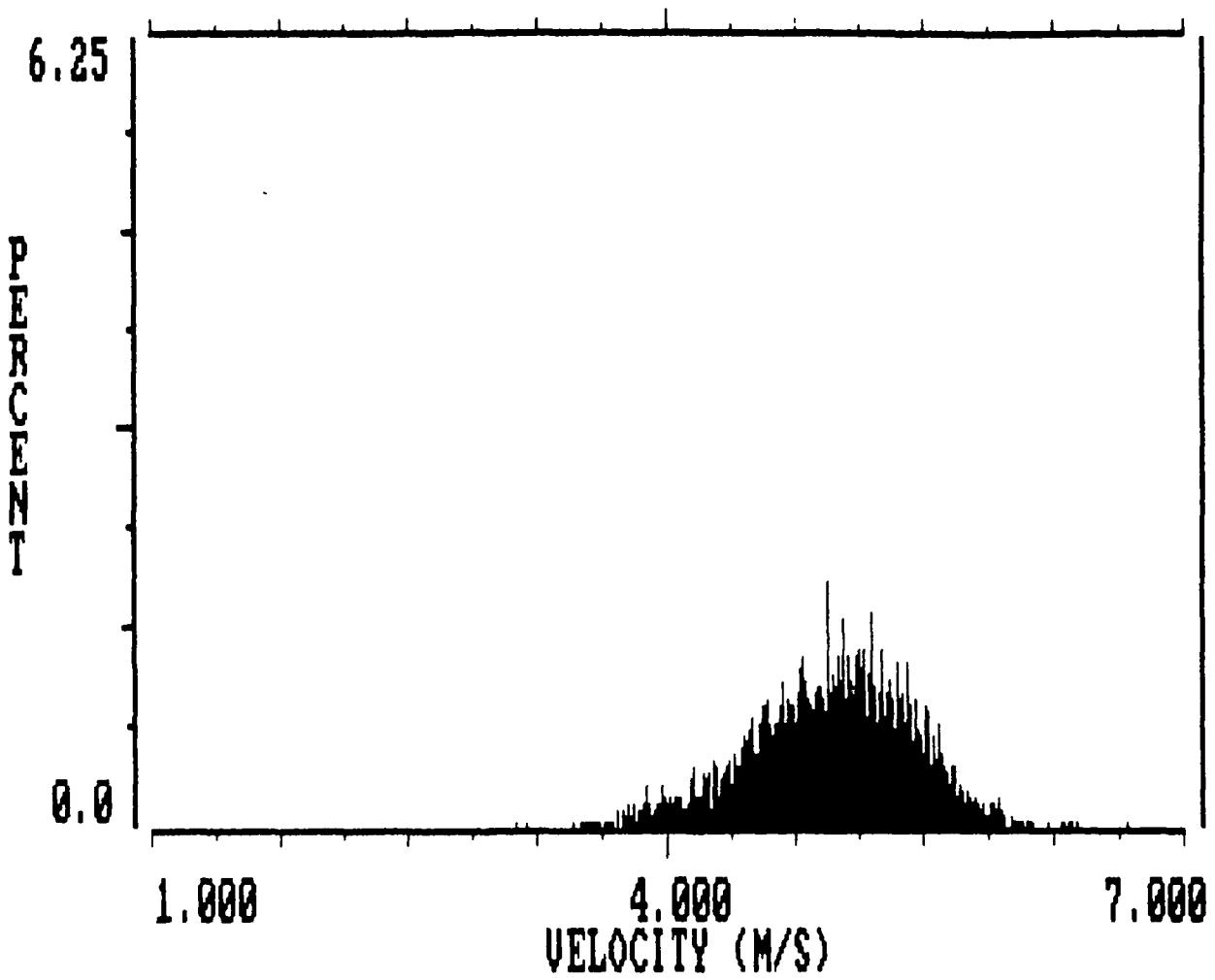
Figure 88.
Boundary Layer, 20 ft/sec
Turbulence in the boundary layer once again broadens the distribution.
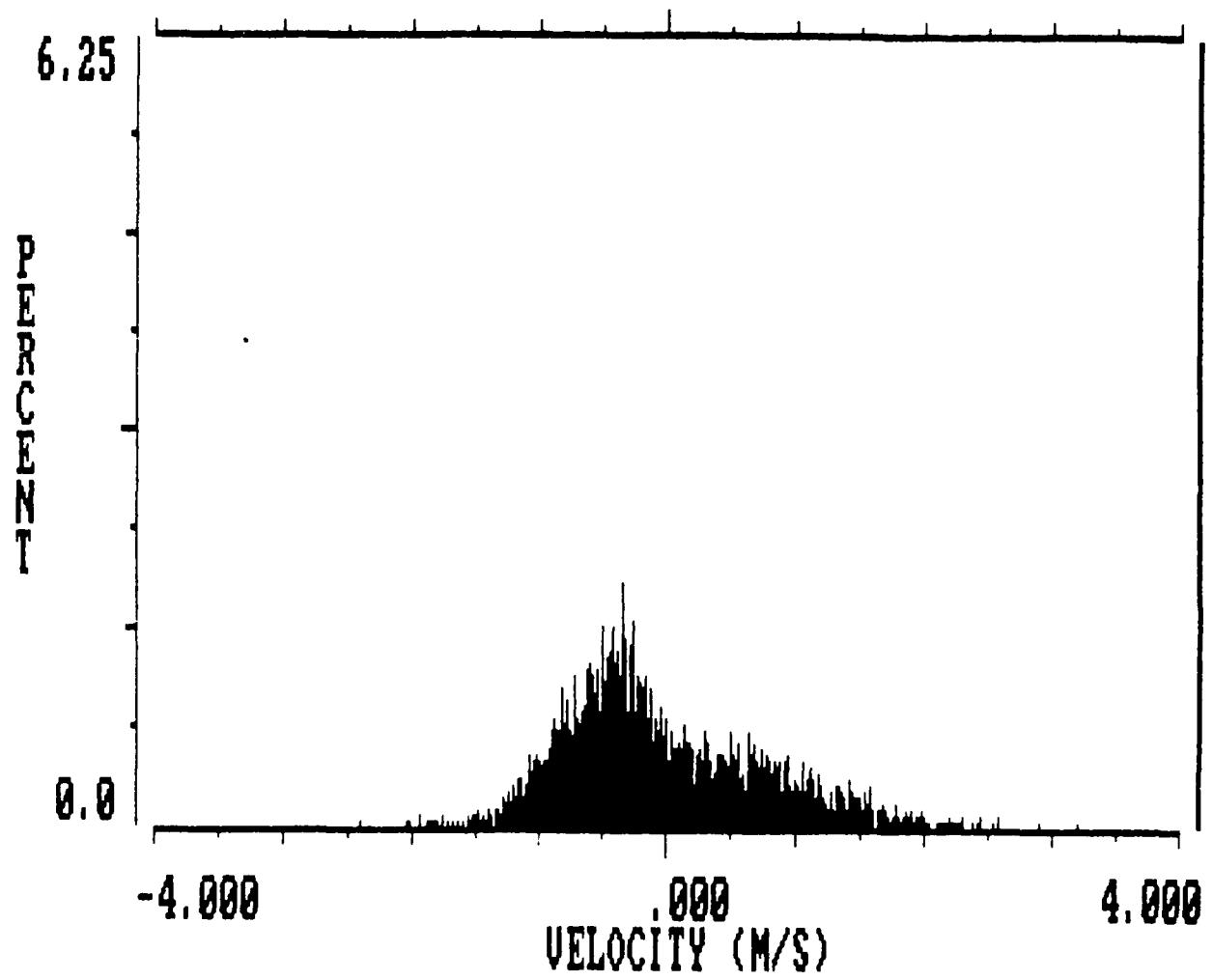
Figure 89.
X=1.5mm, Z=1mm, 20 ft/sec
Double peak is already starting to become evident very close to foil.
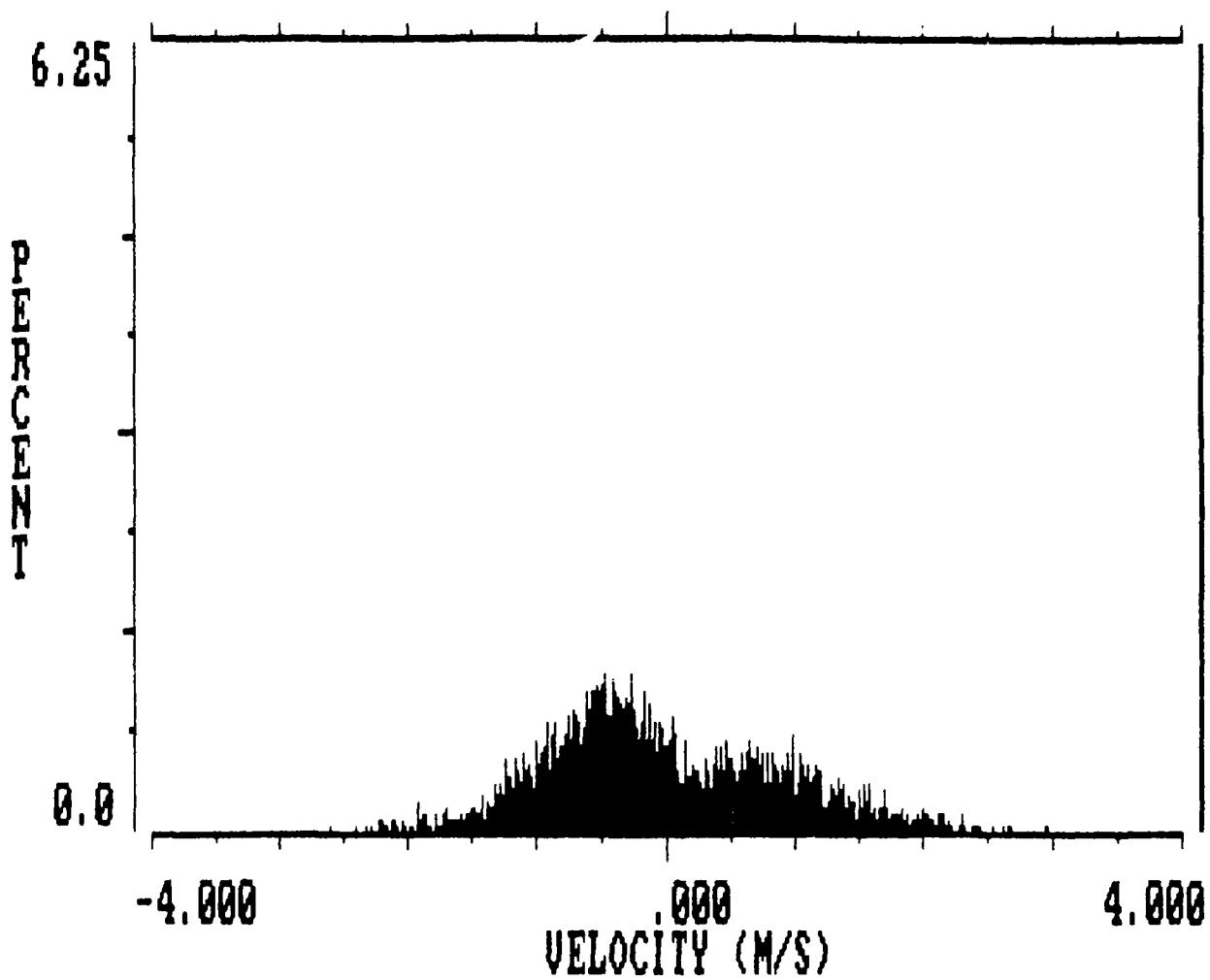
Figure 90.
X=5mm, Z=1mm, 20 ft/sec
The bimodal structure is clearly evident with a dominant negative velocity.
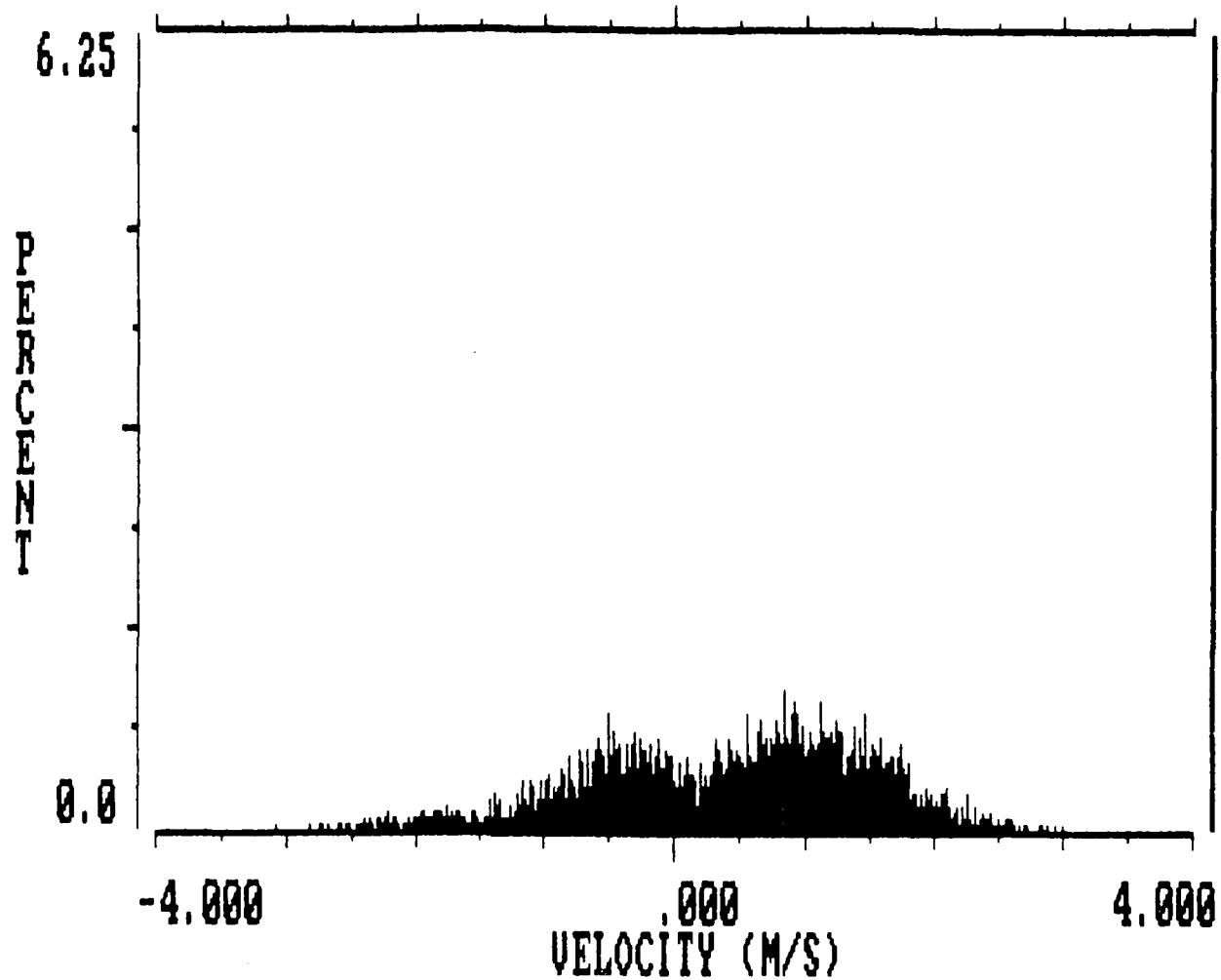
Figure 91.
X=10mm, Z=1mm, 20 ft/sec
The bimodal structure is strongly inherent at 20 ft/sec.
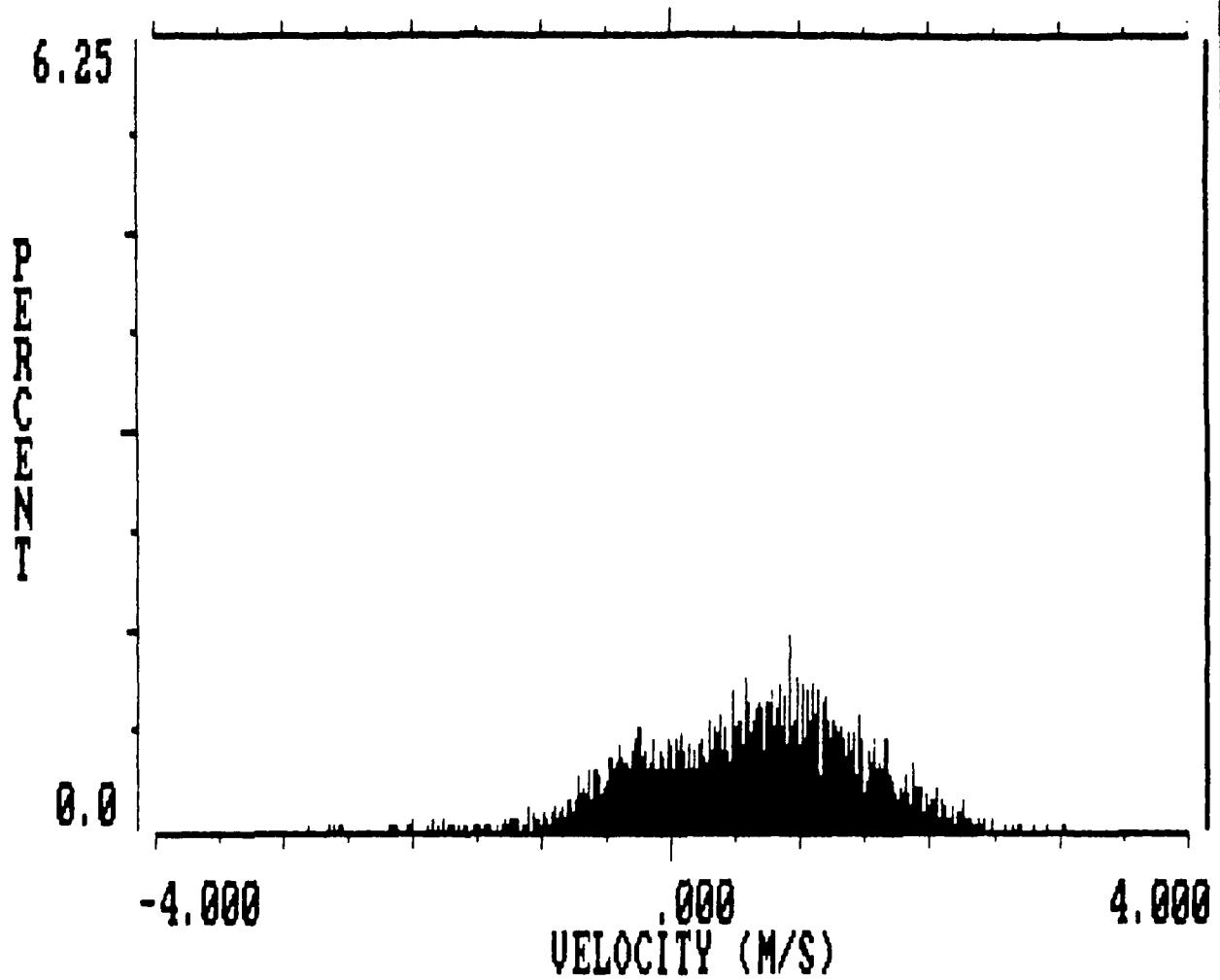
Figure 92.
X=15mm, Z=1mm, 20 ft/sec
The dominant velocity shifts to positive.
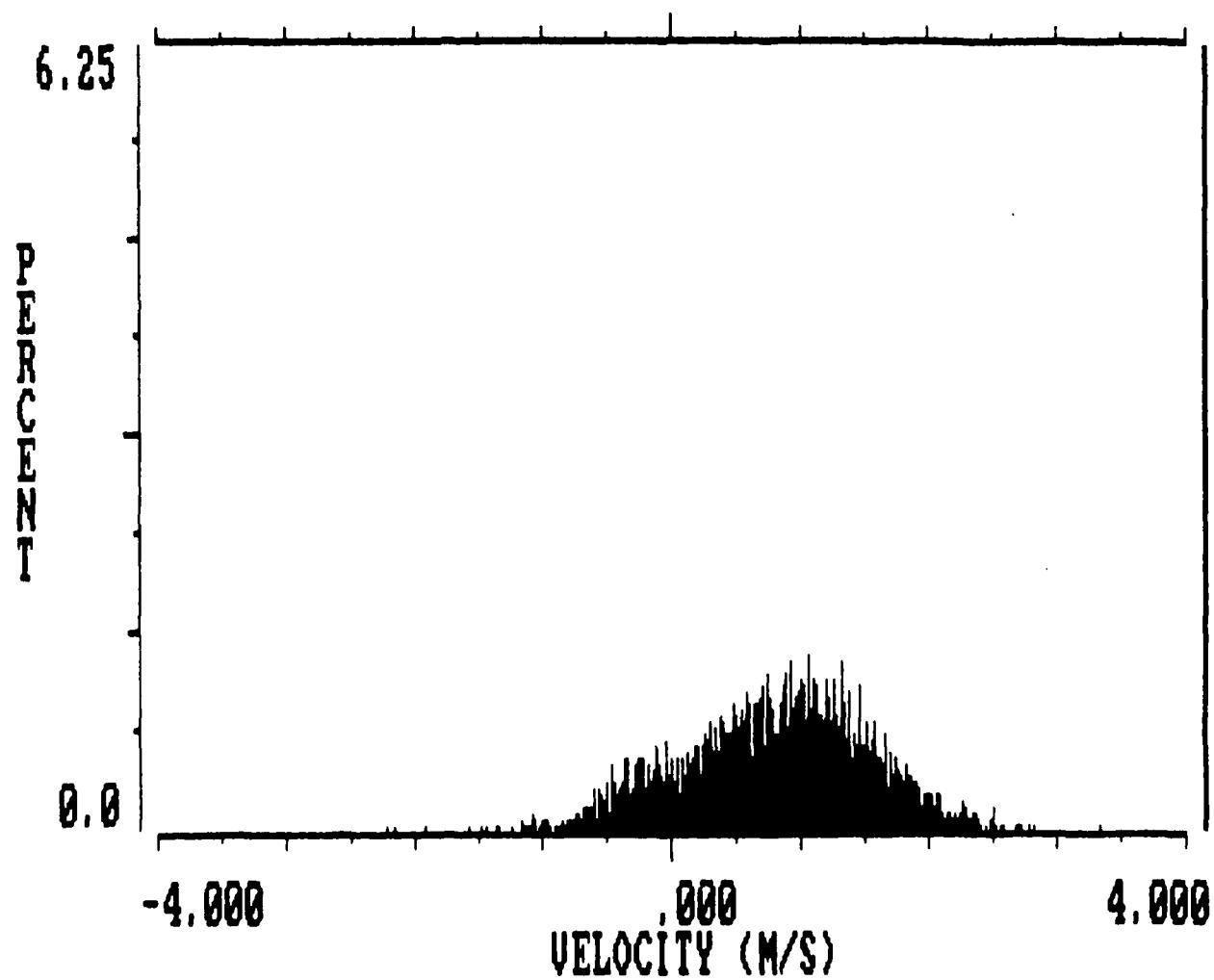
Figure 93.
X=20mm, Z=1mm, 20 ft/sec
The distribution approaches the shape of the boundary layer distribution.
The double peak is still slightly evident.

Figure 93.
X=20mm, Z=1mm, 20 ft/sec
The distribution approaches the shape of the boundary layer distribution.
The double peak is still slightly evident.